

1-1-2010

An Investigation Into The Fouling Phenomena Of Polycarbonate Membranes Used In The Treatment Of Latex Paint Wastewater

Ruston Bedasie
Ryerson University

Follow this and additional works at: <http://digitalcommons.ryerson.ca/dissertations>



Part of the [Chemical Engineering Commons](#)

Recommended Citation

Bedasie, Ruston, "An Investigation Into The Fouling Phenomena Of Polycarbonate Membranes Used In The Treatment Of Latex Paint Wastewater" (2010). *Theses and dissertations*. Paper 1266.

This Thesis is brought to you for free and open access by Digital Commons @ Ryerson. It has been accepted for inclusion in Theses and dissertations by an authorized administrator of Digital Commons @ Ryerson. For more information, please contact bcameron@ryerson.ca.

**AN INVESTIGATION INTO THE FOULING PHENOMENA OF POLYCARBONATE
MEMBRANES USED IN THE TREATMENT OF LATEX PAINT WASTEWATER**

by

Ruston Bedasie

Bachelor of Engineering, Ryerson University, Canada, 2008

A thesis

presented to Ryerson University

in partial fulfillment of the
requirements for the degree of
Master of Applied Science
in the Program of
Chemical Engineering

Toronto, Ontario, Canada, 2010

©Ruston Bedasie 2010

Author's Declaration

I hereby declare that I am the sole author of this thesis.

I authorize Ryerson University to lend this thesis to other institutions or individuals for the purpose of scholarly research.

Ruston Bedasie

I further authorize Ryerson University to reproduce this thesis by photocopying or by other means, in total or in part, at the request of other institutions or individuals for the purpose of scholarly research.

Ruston Bedasie

Abstract

An investigation into the fouling phenomena of polycarbonate membranes used in the treatment of latex paint wastewater

Ruston Bedasie, Master of Applied Science in Chemical Engineering,
Ryerson University, Toronto, 2010

The treatment of latex paint wastewater with ultrafiltration allows for the reuse of the filtrate as process water or for cleaning purposes, as well as the potential for reclamation of the valuable paint solids. In this study, the utilization of polycarbonate membranes for the ultrafiltration of dilute latex dispersions was evaluated. Hydrophilic, flat sheet ultrafiltration membranes with a mean pore size of $0.1\ \mu\text{m}$ were used. All filtration experiments were conducted under constant pressure operation, in a circular, centre-fed, cross-flow filtration cell.

The effect of feed flow rate was investigated, and the steady-state permeate flux achieved showed an increase of 294% between 1.0 and 3.0 L/min. Increasing the operating pressure also resulted in an increased permeate flux, with a 320% increase from 1.5 to 5.5 psi. Also considered was the effect of the feed solid concentration on the permeate flux. When compared to the clean water flux (0% solids) of $5.5 \times 10^{-2}\ \text{m}^3/\text{m}^2\cdot\text{s}$, increasing the feed solid concentration to 0.21% led to a decrease of 290% to $4.04 \times 10^{-2}\ \text{m}^3/\text{m}^2\cdot\text{s}$ steady-state permeate flux.

Surfactant-enhanced ultrafiltration was also studied, with concentrations ranging from 25% to 200% of the literature values of the surfactant's critical micelle concentration (CMC) in pure water. The addition of an anionic surfactant, sodium dodecyl sulphate (SDS), reduced the effectiveness of the filtration. However, the addition of a cationic surfactant, cetyl trimethylammonium bromide (CTAB), increased the permeate flux of the latex dispersion up to 130% when twice its CMC was

used, with evidence of a reduction in the effect of fouling of the membranes. This may be due to repelling interactions between the surface of the membrane and the surface of the formed micelles, as well as a reduced cake resistance due to the larger particle size of the constituents forming a less dense cake layer.

Acknowledgements

I would like to express my deepest appreciation to Dr. Huu Doan for his excellent supervision during the entirety of this thesis, and his timely and comprehensive feedback, as well as his guidance and support during the course of my studies at Ryerson University. I would also like to thank Dr. Ali Lohi for his direction and valuable input.

Thanks to my thesis evaluation committee, Dr. Chil-Hung Cheng, Dr. Ramdhane Dhib, and Dr. Jiangning Wu for taking the time in reviewing this work and for their valuable comments and advice for improving this document.

I would also like to extend my gratitude to every person in the Department of Chemical Engineering at Ryerson University, including Ms. Caltha Rimmer, Ms. Isabella Fernandes, Mr. Tondar Tajrobehkar, Mr. Ali Hemmati, and Mr. Daniel Boothe.

I extend my thanks to my family, especially my parents, who have always provided me with unconditional encouragement and support, even when so far away.

Finally, I would like to thank my fellow students at Ryerson University for providing assistance and ideas when needed.

Dedication

To my parents...

Table of Contents

Author's Declaration	iii
Abstract.....	v
Acknowledgements	vii
Dedication	viii
Table of Contents	ix
Lists of Tables	xii
List of Figures.....	xiii
Nomenclature	xvii
Chapter 1 Introduction.....	1
Chapter 2 Literature Review	3
2.1 Membrane Filtration.....	3
2.1.1 Constant Pressure Filtration.....	6
2.1.2 Concentration Polarization.....	7
2.2 Membrane Fouling.....	9
2.2.1 Empirical Equations	10
2.2.2 Semi-Empirical Equations.....	10
2.3 Factors Affecting Fouling.....	14
2.3.1 Temperature.....	14
2.3.2 Cross-Flow Velocity	14
2.3.3 Transmembrane Pressure	15
2.3.4 Constituents in the Feed/Model Chemicals	16
2.4 Micellar-Enhanced Ultrafiltration	16

Chapter 3	Materials and Methods.....	19
3.1	Filtration Experiments.....	19
3.1.1	Experimental Setup	19
3.1.2	Ultrafiltration Membranes	21
3.1.3	Preparation of Latex Paint Dispersions to Simulate Wastewater	21
3.1.4	Operating Parameters.....	22
3.1.5	Operating Procedure	22
3.2	Analytical Methods.....	23
3.2.1	Solid Concentration.....	23
3.2.2	Particle Size Distribution of Latex Paint Dispersions	23
3.2.3	Scanning-Electron Microscopy (SEM)	24
Chapter 4	Results and Discussions.....	27
4.1	Effect of Feed Flow Rate on Permeate Flux	27
4.2	Effect of Transmembrane Pressure on Permeate Flux	32
4.3	Effect of Solid Concentration of Feed on Permeate Flux	35
4.4	Pretreatment of Feed with Anionic Surfactant SDS.....	38
4.5	Pretreatment of Feed with Cationic Surfactant CTAB.....	39
4.6	Determining the Mass Transfer Coefficient at Membrane Surface.....	43
4.7	Empirical Models for Filtration	45
4.7.1	Complete Blocking Model.....	45
4.7.2	Intermediate Blocking Model.....	49
4.7.3	Standard Blocking Model.....	54
4.7.4	Cake Layer Formation Model	58
4.7.5	Summary of Regression Coefficients	62
4.7.6	Changing Modes of Fouling over Filtration Time	63
4.8	Resistance-in-series Model.....	67

Chapter 5	Conclusions and Recommendations.....	71
5.1	Conclusion.....	71
5.2	Recommendations.....	72
References.....		75
Appendix A	Experimental Data Collected	81
Appendix B	t/v Data Graphs	85
Appendix C	Ultrafiltration Cell	88
Appendix D	Reproducibility	91

Lists of Tables

Table 2-1: Comparison of different types of membranes.....	4
Table 2-2: Hermia's models adapted for each model of fouling.....	13
Table 3-1: Membrane properties	21
Table 4-1: Comparison between experimental initial permeate flux and the initial permeate flux obtained from the complete blocking model	46
Table 4-2: Comparison between experimental initial permeate flux and the initial permeate flux obtained from the intermediate blocking model.....	51
Table 4-3: Comparison between experimental initial permeate flux and the initial permeate flux obtained from the standard blocking model.....	56
Table 4-4: Comparison between experimental initial permeate flux and the initial permeate flux obtained from the cake layer formation model	60
Table 4-5: Measures of fit to the experimental data for Hermia's model.....	62
Table 4-6: Measures of fit to the experimental data for Hermia's models dependant on the time domain considered.....	64
Table C-1: Maximum Reynolds number of flow on the feed side of the ultrafiltration cell for various feed flow rates	90
Table D-1: Filtration constants for repeated trials at $Q_f=2.0\text{L}/\text{min}$, $P=3.5\text{ psi.}$, and $C_s=0.12\%$	92

List of Figures

Figure 2-1: Illustration of Dead-End (a) and Cross-Flow (b) Modes of Ultrafiltration	5
Figure 2-2: Illustrations of various ultrafiltration configurations (a) tubular hollow fiber module (b) plate-and-frame module (c) spiral wound module, and (d) rod module.....	6
Figure 2-3: Illustration of gel layer model of concentration polarization.....	8
Figure 2-4: The four basic types of fouling considered by Hermia's models (a) complete blocking (b) intermediate blocking (c) standard blocking (d) cake layer formation.....	12
Figure 2-5: Pressure-flux characteristic in cross-flow ultrafiltration	15
Figure 2-6: Illustration of (a) surfactant molecule (b) micelle composed of a number of surfactant molecules.....	17
Figure 3-1: Schematic diagram of the experimental setup.....	20
Figure 3-2: Cross-section schematic view of membrane filtration unit.....	20
Figure 3-3: Microtrac S3500 operating schematic diagram (Microtrac, 2008)	24
Figure 3-4: Particle Size Distribution of Latex Paint Dispersion	24
Figure 3-5: SEM image of clean membrane, gold-coated.....	25
Figure 3-6: Illustration of the area of extracted samples from fouled membranes.....	25
Figure 4-1: Permeate flux vs time for various feed flow rates. $P=3.5\text{psi.}$, $C_s=0.12\%$	28
Figure 4-2: Steady-State Permeate Flux vs Feed Flow Rates at $t=800\text{ s}$	29
Figure 4-3: Filtration constants obtained from t/V vs. V graphs vs Feed Flow Rate $P=3.5\text{psi.}$, $C_s=0.12\%$ (a) K_p (b) F_M	30
Figure 4-4: SEM images of sample of membrane after ultrafiltration ($t = 1200\text{s}$) $Q_f=2.0\text{L/min}$, $P=3.5\text{psi.}$, $C_s=0.12\%$	31
Figure 4-5: SEM images of sample of membrane after ultrafiltration ($t = 1200\text{s}$) (a) $Q_f=1.0\text{L/min}$, $P=3.5\text{ psi.}$, $C_s=0.12\%$ (b) $Q_f=3.0\text{L/min}$, $P=3.5\text{ psi.}$, $C_s=0.12\%$	31
Figure 4-6: Permeate flux vs time for various transmembrane pressures, $Q_f=2.0\text{L/min}$, $C_s=0.12\%$	32
Figure 4-7: Steady-State Permeate Flux vs Transmembrane Pressure at $t=800\text{ s}$	33
Figure 4-8: Filtration constants obtained from t/V vs. V graphs vs Transmembrane pressure $Q_f=2.0\text{L/min}$ $C_s=0.12\%$	34
Figure 4-9: SEM images of sample of membrane after ultrafiltration ($t = 1200\text{s}$) (a) $Q_f=2.0\text{L/min}$, $P=2.5\text{ psi.}$, $C_s=0.12\%$ (b) $Q_f=2.0\text{L/min}$, $P=4.5\text{ psi.}$, $C_s=0.12\%$	35

Figure 4-10: Permeate flux vs time for various Feed Solid concentrations, $Q_f=2.0\text{L/min}$, $P=3.5\text{psi}$	36
Figure 4-11: Steady-State Permeate Flux vs Feed Solid Concentration at $t=800\text{ s}$	37
Figure 4-12: Filtration constants obtained from t/V vs. V graphs vs Feed Solid Concentration $Q_f=2.0\text{L/min}$, $P=3.5\text{psi}$	37
Figure 4-13: SEM images of sample of membrane after ultrafiltration ($t = 1200\text{s}$) (a) $Q_f=2.0\text{L/min}$, $P=3.5\text{ psi}$, $C_s=0.04\%$ (b) $Q_f=2.0\text{L/min}$, $P=3.5\text{ psi}$, $C_s=0.21\%$	38
Figure 4-14: Steady-State Permeate Flux vs SDS surfactant concentrations at $t=800\text{s}$	39
Figure 4-15: Representation of micelles formed using cationic surfactant	40
Figure 4-16: Permeate flux vs time for various CTAB concentrations, $P=3.5\text{psi}$, $Q_f=2.0\text{L/min}$, $C_s=0.12\%$ paint solids	41
Figure 4-17: Steady-State Permeate Flux vs CTAB concentrations after $t=800\text{ s}$	41
Figure 4-18: Filtration constants obtained from t/V vs. V graphs for various CTAB concentrations, $P=3.5\text{psi}$, $Q_f=2.0\text{L/min}$, $C_s=0.12\%$ paint solids	42
Figure 4-19: SEM images of sample of membrane after ultrafiltration with CTAB addition to the feed solution, $Q_f=2.0\text{ L/min}$, $P=3.5\text{ psi}$, $C_s=0.12\%$, $\text{CTAB}=0.492\text{g/L}$ ($t = 1200\text{s}$)	43
Figure 4-20: Permeate Flux vs time with recycle of retentate stream to the feed tank $P=3.5\text{psi}$, $Q_f=2.0\text{L/min}$, $C_s=0.12\%$	44
Figure 4-21: Permeate Flux vs $\text{Ln}(\text{CF})$	44
Figure 4-22: Permeate flux predicted by the complete blocking model for various feed flow rates $P=3.5\text{psi}$, $C_s=0.12\%$	46
Figure 4-23: Permeate flux predicted by the complete blocking model for various operating pressures $Q_f=2.0\text{L/min}$, $C_s=0.12\%$	47
Figure 4-24: Permeate flux predicted by the complete blocking model for various feed solid concentrations, $Q_f=2.0\text{L/min}$, $P=3.5\text{ psi}$	48
Figure 4-25: Permeate flux predicted by the complete blocking model for various concentrations of CTAB, $P=3.5\text{psi}$, $Q_f=2.0\text{L/min}$, $C_s=0.12\%$ paint solids	49
Figure 4-26: Permeate flux predicted by the intermediate blocking model for various feed flow rates $P=3.5\text{ psi}$, $C_s=0.12\%$	51
Figure 4-27: Permeate flux predicted by the intermediate blocking model for various operating pressures $Q_f=2.0\text{L/min}$, $C_s=0.12\%$	52
Figure 4-28: Permeate flux predicted by the intermediate blocking model for various feed solid concentrations, $Q_f=2.0\text{L/min}$, $P=3.5\text{psi}$	53

Figure 4-29: Permeate flux predicted by the intermediate blocking model for various concentrations of CTAB, $P=3.5\text{psi}$, $Q_f=2.0\text{L/min}$, $C_s=0.12\%$ paint solids	53
Figure 4-30: Permeate flux predicted by the standard blocking model for various feed flow rates $P=3.5\text{psi}$, $C_s=0.12\%$	55
Figure 4-31: Permeate flux predicted by the standard blocking model for various transmembrane pressures $Q_f=2.0\text{L/min}$, $C_s=0.12\%$	56
Figure 4-32: Permeate flux predicted by the standard blocking model for various feed solid concentrations, $Q_f=2.0\text{L/min}$, $P=3.5\text{psi}$	57
Figure 4-33: Permeate flux predicted by the standard blocking model for various concentrations of CTAB, $P=3.5\text{psi}$, $Q_f=2.0\text{L/min}$, $C_s=0.12\%$ paint solids	57
Figure 4-34: Permeate flux predicted by the cake layer formation model for various feed flow rates $P=3.5\text{psi}$, $C_s=0.12\%$	59
Figure 4-35: Permeate flux predicted by the cake layer formation model for various operating pressures $Q_f=2.0\text{L/min}$, $C_s=0.12\%$	60
Figure 4-36: Permeate flux predicted by the cake layer formation model for various feed solid concentrations, $Q_f=2.0\text{L/min}$, $P=3.5\text{psi}$	61
Figure 4-37: Permeate flux predicted by the cake layer formation model for various concentrations of CTAB, $P=3.5\text{psi}$, $Q_f=2.0\text{L/min}$, $C_s=0.12\%$ paint solids	61
Figure 4-38: Permeate flux predicted by the complete blocking model at various time intervals over the experimental run, $Q_f=2.0\text{L/min}$, $P=3.5\text{psi}$, $C_s=0.12\%$	65
Figure 4-39: Permeate flux predicted by the intermediate blocking model at various time intervals over the experimental run, $Q_f=2.0\text{L/min}$, $P=3.5\text{psi}$, $C_s=0.12\%$	65
Figure 4-40: Permeate flux predicted by the standard blocking model at various time intervals over the experimental run, $Q_f=2.0\text{L/min}$, $P=3.5\text{psi}$, $C_s=0.12\%$	66
Figure 4-41: Permeate flux predicted by the cake layer formation model at various time intervals over the experimental run, $Q_f=2.0\text{L/min}$, $P=3.5\text{psi}$, $C_s=0.12\%$	66
Figure 4-42: Permeate flux to demonstrate dominant mode of fouling over time, $Q_f=2.0\text{L/min}$, $P=3.5\text{psi}$, $C_s=0.12\%$ paint solids	67
Figure 4-43: Steady-State permeate flux vs (a) Feed Flow Rate ($P=3.5\text{psi}$, $C_s=0.12\%$ or 0% for distilled water) (b) Operating Pressure ($Q_f=2.0\text{L/min}$, $C_s=0.12\%$ or 0% for distilled water)	68
Figure 4-44: Total resistance to permeate flow, R_{TOT} vs Feed Flow Rate, Q_f	69

Figure 4-45: Total resistance to permeate flow, R_{TOT} vs Operating Pressure	69
Figure A-1: Cumulative mass of permeate collected vs time for various operating conditions using Distilled Water.....	81
Figure A-2: Permeate Flux vs time for various feed flow rates using Distilled Water	82
Figure A-3: Permeate flux vs time for various operating pressures using Distilled Water	82
Figure A-4: Cumulative mass of permeate collected vs time for various feed flow rates, $P=3.5\text{psi}$, $C_s=0.12\%$	83
Figure A-5: Cumulative mass of permeate collected vs time for various operating pressures, $Q_f=2.0\text{L/min}$, $C_s=0.12\%$	83
Figure A-6: Cumulative mass of permeate collected vs time for various feed solid concentrations $Q_f=2.0\text{L/min}$, $P=3.5\text{ psi}$	84
Figure A-7: Cumulative mass of permeate collected vs time for various CTAB surfactant concentrations, $Q_f=2.0\text{L/min}$, $P=3.5\text{ psi}$, $C_s=0.12\%$	84
Figure B-1: t/V vs V plots for various feed flow rates, $P=3.5\text{psi}$, $C_s=0.12\%$	85
Figure B-2: t/V plots for various operating pressures, $Q_f=2.0\text{L/min}$, $C_s=0.12\%$	86
Figure B-3: t/V vs V plots for various feed concentrations, $Q_f=2.0\text{L/min}$, $P=3.5\text{ psi}$	86
Figure B-4: t/V vs V plots for various CTAB surfactant concentrations, $Q_f=2.0\text{L/min}$, $P=3.5\text{psi}$, $C_s=0.12\%$	87
Figure C-1: Ultrafiltration cell with dimensions (all sizes in mm)	89
Figure D-1: t/V vs V plots for various CTAB surfactant concentrations, $Q_f=2.0\text{L/min}$, $P=3.5\text{psi}$, $C_s=0.12\%$	91

Nomenclature

Roman Symbols

Symbol	Description	Units
A	Filter membrane surface area	m^2
A₀	Initial active membrane surface area	m^2
C	Volume of solid particles retained per unit filtrate volume	--
C_B	Concentration of the bulk	% or kg solute/ m^3 solvent
CF	Concentration Factor	--
C_G	Gel Concentration	% or kg solute/ m^3 solvent
C_s	Solid Concentration of the feed	% or kg solute/ m^3 solvent
D	Diffusivity	m^2/s
F_M	Filtration constant	s/m^3
H	Distance between the two plane-parallel discs	m
J₀	Initial permeate flux	$m^3/m^2.s$
J_p	Permeate Flux	$m^3/m^2.s$
J_s	Flux of diffusion of solute molecules towards the bulk	$m^3/m^2.s$
k	Mass Transfer Coefficient	$m^3/m^2.s$ or m/s
K_b	Complete pore blocking model constant	$1/s$
K_c	Cake layer formation model constant	s/m^6
K_i	Intermediate pore blocking model constant	$1/m^3$
K_p	Filtration constant	s/m^6
K_s	Standard pore blocking model constant	$1/s^2$
L	Membrane thickness	m
m	Mass ratio of wet to dry cake	--
n	Blocking index	--
Q	Flow rate	m^3/s
Q_f	Feed Flow Rate	L/min
R	Filter resistance	$1/m$
R_C	Cake resistance	$1/m$
R_{CP}	Concentration polarization layer resistance	$1/m$
R_F	Fouling resistance	$1/m$

Symbol	Description	Units
R_M	Membrane resistance	1/m
R_p	Pore blocking resistance	1/m
R_{TOT}	Total resistance to permeate flow	1/m
s	Mass fraction of solids in slurry	--
u_0	Filtrate linear velocity	m/s
V	Volume of permeate collected	m ³
V_F	Initial volume of feed in tank	m ³
V_t	Volume remaining in the feed tank after time t	m ³
ΔP	Operating Pressure/Transmembrane Pressure	psi.

Greek Symbols

Symbol	Description	Units
α	Specific cake resistance	m/kg
β	Resistance coefficient	--
γ	Filtrate density	kg/m ³
δ	Boundary layer thickness	m
η	Viscosity	Pa.s
μ	Viscosity	Pa.s
σ	Blocked area per unit filtrate volume	1/m

Acronyms

Symbol	Description
BOD	Biological Oxygen Demand
COD	Chemical Oxygen Demand
CMC	Critical Micelle Concentration
CTAB	Cetyl trimethylammonium bromide
PEG	Poly(ethylene glycol)
SDS	Sodium dodecyl sulfate

Chapter 1

Introduction

During the manufacture of paint products, a large amount of wastewater is generated when reactors and mixing basins are cleaned. Containing a wide variety of constituents such as organic and inorganic pigments, latexes, solvents, and emulsifying agents, this wastewater cannot be discharged directly from the manufacturing sites.

Paint effluents typically have high levels of biological oxygen demand (BOD, greater than 580 mg/L), chemical oxygen demand (COD, greater than 5500 mg/L), suspended solids, and turbidity (Dey et al., 2004). It also has the potential to promote the growth of microorganisms, which, after consuming available oxygen, anaerobic growth initiates, and through microbial degradation, unwanted gases such as hydrogen sulphide may be produced.

Ultrafiltration for wastewater treatment can no longer be considered an emerging technology. It has been implemented on large scale applications in both industrial and municipal wastewater treatment facilities, particularly in membrane bioreactors. However, the technology's wide-spread use has also been hindered by the occurrence of the fouling phenomenon, where the efficiency of the process significantly declines over time. In this study, the fouling phenomenon is investigated for latex dispersions.

One of the benefits of treating water-based paint effluents by ultrafiltration over other processes such as electrochemical oxidation (Korbahti et al., 2007) or Fenton oxidation (Kurt et al., 2006) is the potential to reclaim some of the solids in the paint effluents for reuse, as well as the reuse of the filtrate itself as process water or for cleaning purposes (Dey et al., 2004). A study involving the

reclamation of feed water was previously performed by Anderson et al. (1981) for automotive electrocoat paint effluent using reverse osmosis.

The removal of latex dispersions from wastewater has previously been studied using microporous alumina membranes (Mikulasek and Cakl, 1994). However, there is little information available in literature on the use of polycarbonate membranes for this purpose. The pretreatment of latex paint wastewater with surfactant to improve the ultrafiltration performance has also not been previously studied.

The objectives of this study are outlined as follows:

- To examine the utilization of track-etched polycarbonate membranes in the ultrafiltration of dilute latex dispersions.
- To investigate the effect of major ultrafiltration process parameters on the fouling of these membranes. These include feed flow rate, operating transmembrane pressure, and concentration of solids in the feed.
- To investigate the effect of the addition of different types of surfactants on the efficiency of the ultrafiltration process.
- To evaluate the mass transfer coefficient near the membrane surface after concentration polarization.

Chapter 2

Literature Review

In this section, a review of membrane filtration is presented. Following this, some of the past research activities in the field is discussed.

2.1 Membrane Filtration

Membrane filtration is a physical process that separates solid constituents of a solution based on the particle size of the solids in comparison to the pore size of the membranes. It is the pore size of the membranes that determine the mode of which membrane filtration is being performed. These are illustrated in Table 2-1, along with some of the typical constituents that are excluded in the process (Tchobanoglous et al., 2003).

Membrane filtration relies on a high pressure differential between the feed/retentate, and the permeate (Geankopolis, 1993). The solvent, in this case water, and other small molecules pass through the membrane, forming the permeate. The operating pressure is dependent on the osmotic pressure of the wastewater, which in turn, depends on the constituents in the wastewater being treated. Because the operation of this process occurs at ambient temperatures and does not require a phase change, the components left in the retentate are not altered and may be recovered in another external process.

Employing membrane filtration as a part of the wastewater treatment scheme improves the handling capabilities of the system. Selectivity is mainly based on the size of the components being removed from the water. Ultrafiltration has been applied as a pre-treatment method, where suspended and

colloidal compounds are removed (Beca, 2007). It acts as a barrier to following stages of treatment and in particular, the reverse osmosis process.

Besides the pore size, operating the various modes of membrane filtration requires higher operating pressures as the pore size decreases (Kennedy et al., 2008). Typical operating pressure for ultrafiltration, the focus of this study, ranges between 4-7 psi.

Table 2-1: Comparison of different types of membranes (Tchobanoglous et al., 2003)

Process	Structure (Pore size)	Typical operating range (μm)	Typical constituents removed
Micro-filtration	Macropore (>50 nm)	0.08-2.0	TSS, turbidity, some bacteria and viruses
Ultra-filtration	Mesopores (2-50 nm)	0.005-0.2	Macromolecules, most bacteria, some viruses
Nano-filtration	Micropores (<2 nm)	0.001-0.01	Small molecules, most viruses
Reverse Osmosis	Dense (<2 nm)	0.0001-0.001	Very small molecules, metallic and other ions such as sodium and nitrates

There are two main modes of membrane filtration processes. The first is dead-end mode, where feed is directed perpendicularly to the membrane surface, as illustrated in Figure 2-1 (a). In this mode, the feed is forced through the membrane, allowing a sieving effect to occur to separate the particles larger than the pore size of the membrane from the generated permeate flow stream. Because of this separation, a large cake of the solids builds on the membrane surface over time, requiring an increase of pressure on the feed side to achieve the desired permeate flow rate.

The second mode of membrane filtration is cross flow, depicted in Figure 2-1 (b), where the feed flows parallel to the membrane surface. As separation across the membrane occurs, the exiting stream (the retentate) increases in concentration since some of the clean solvent is removed in the permeate stream. A cake builds up over time on the surface of the membrane as in dead-end mode. However, there is usually a limit to the cake thickness in cross-flow mode.

The preferred mode of ultrafiltration depends greatly on its application. For wastewater treatment processes, cross-flow mode is most commonly found (Benitez et al., 2009; Burba et al., 2005). Even though not used in large-scale installations, dead-end filtration can be useful in determining initial hydrophobic adsorption and steric and electrostatic exclusion (Yoon et al., 2004).

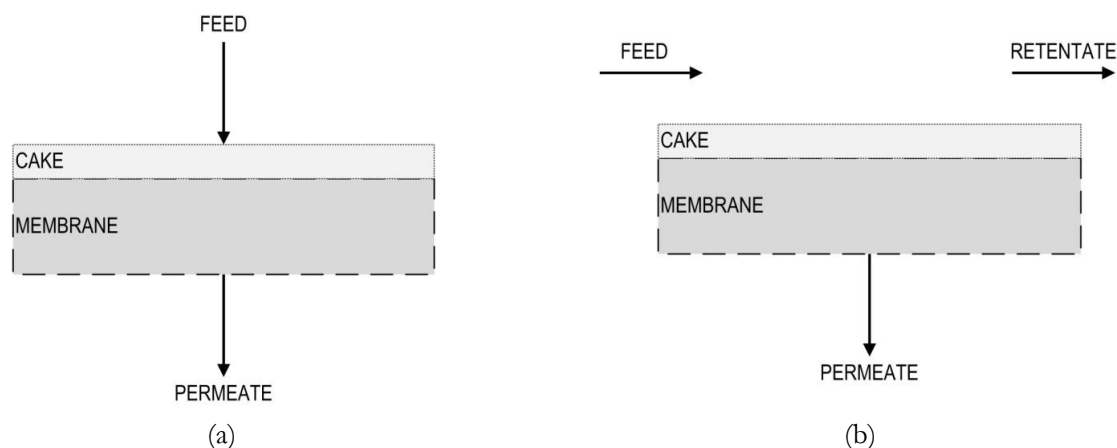


Figure 2-1: Illustration of Dead-End (a) and Cross-Flow (b) Modes of Ultrafiltration

Membranes are manufactured from many materials, falling into one of two classes: polymeric or ceramic. Polymeric materials include aromatic amides, polysulphonates, polyvinyl alcohol and polyacetylene to name a few (Shirazi et al., 2010). Many studies have been conducted to compare the efficiency of membranes made of various materials for the removal of specific compounds. In this study, polymeric membranes made out of polycarbonate were used.

Depending on the materials used for construction, the membrane may be charged. Through numerous experimental testing, it was found that uncharged organics were separated mainly due to steric hindrance (Yoon et al., 2004). The separation of charged organics, however, was mainly influenced by electrostatic interactions with the charged membranes (Berg et al., 1997). Molecular weight of the charged organics also affected the rejection levels achieved. Charged organics with higher molecular weights showed a higher degree of rejection than those with a smaller molecular weight. In general, membrane surfaces are negatively charged to prevent fouling by deposition of negatively charged natural organic matter (NOM) in water (Kennedy et al., 2008).

There are many configurations of ultrafiltration membranes. The membranes can be flat-sheet or tubular. Figure 2-2 shows four common geometries.

In many of the studies reviewed, characterization of the membranes was performed independently of the manufacturer's specifications to determine their molecular-weight cut-off or range of rejection through their narrow pores. This can be done by filtering samples containing various molecular weights of standardized polystyrene sulfonate polymers (Burba et al., 2005). Glucose has also been used to evaluate this specification (Oatley et al., 2005). Membrane pore size can also be determined using polyethylene glycol (PEG) (Yoon et al., 2004).

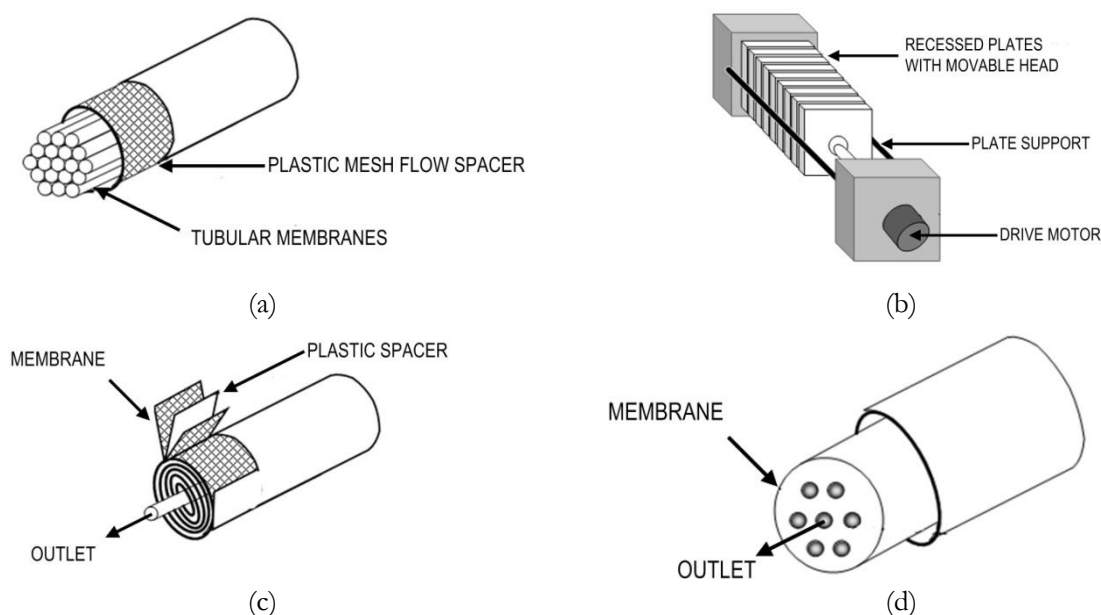


Figure 2-2: Illustrations of various ultrafiltration configurations (a) tubular hollow fiber module (b) plate-and-frame module (c) spiral wound module, and (d) rod module (Russell, 2006)

After samples of the retentate have been collected, various analytical procedures are used to determine the efficiency of the separation. One such procedure involves using a UV-visible spectrometer, which can qualitatively determine if the components being separated from the feed stream are present in the retentate depending on the absorbance of the sample (Burba et al., 2005). Other techniques used includes high performance liquid chromatography (HPLC) and Fourier transform infrared spectroscopy (FTIR). Alternatively, if the feed composition was unknown or variable, COD determination using the standardized potassium dichromate ($K_2Cr_2O_7$) method was used to evaluate the reduction in the COD (Csefalvay et al., 2008).

2.1.1 Constant Pressure Filtration

Ultrafiltration can be performed in either constant pressure operation or in constant permeate flow rate operation. In an industrial setting, it is usually more desirable to operate in constant permeate flow rate mode. However, this can be very difficult to achieve, particularly for lab scale size installations. For the purpose of this study, the experimental trials were all performed under constant pressure operation. Details of the control of the operating pressure are provided in Chapter 3.

Based on the Blake-Kozeny equation applied to filtration to incorporate both filter cake and filter medium resistances, the following expression was found for constant pressure operation (Geankopolis, 1993).

$$\frac{dt}{dV} = \frac{\mu\alpha C_s}{-\Delta PA^2} V + \frac{\mu R_M}{-\Delta PA} = K_p V + F_M \quad (1)$$

By separating the variables and integrating Equation (1), the following expressions can be obtained.

$$\frac{t}{V} = \frac{K_p}{2} V + F_M \quad (2)$$

$$K_p = \frac{\mu\alpha C_s}{-\Delta PA^2} \quad (3)$$

$$F_M = \frac{\mu R_M}{-\Delta PA} \quad (4)$$

Plots of t/V vs. V allows the extraction of the constants K_p and F_M . As Equation (3) shows, K_p relates to the resistance due to the cake built up on the membrane surface due to the presence of the specific cake resistance, α , term. Similarly, due to the resistance of the filter medium, R_M , in Equation (4), F_M can be used to indicate the extent of the membrane resistance. A limitation of this model is that it is unable to identify the mechanisms of fouling occurring during the membrane separation process. The different mechanisms involved in the fouling phenomena are described further in Section 2.2.

2.1.2 Concentration Polarization

Concentration polarization is a phenomenon due to a build-up of inorganic species at the membrane-liquid interface, resulting in a region of higher concentration than in the bulk (Song and Elimelech, 1995). This effect is predominantly found in reverse osmosis and nanofiltration applications but may occur in ultrafiltration and microfiltration systems if the inorganic species chemically bond to compounds being retained by the membrane (Benitez et al., 2009).

There are a number of proposed models used to describe permeate flux decline due to concentration polarization. The resistance-in-series model is commonly used, but has the limitation of only predicting the fouling behaviour of colloids and mono-dispersed particles. The gel layer model, as illustration in Figure 2-3, is used to determine permeate flux based on a constant gel layer resistance and membrane resistance (Shirazi et al., 2010), derived by adapting convective heat transfer theories.

Concentration polarization may lead to increased occurrences of particles in the feed breaking through to the permeate stream, essentially deteriorating permeate quality (Shirazi et al., 2010). At the same time, there is a reduction in the permeate flux due to the formation of the gel layer. There is back diffusion of particles in the gel layer (depicted as J_s in Figure 2-3). This formation and back diffusion occurs until a steady state is reached, when the rate of back diffusion approaches the rate of accumulation near the membrane surface.

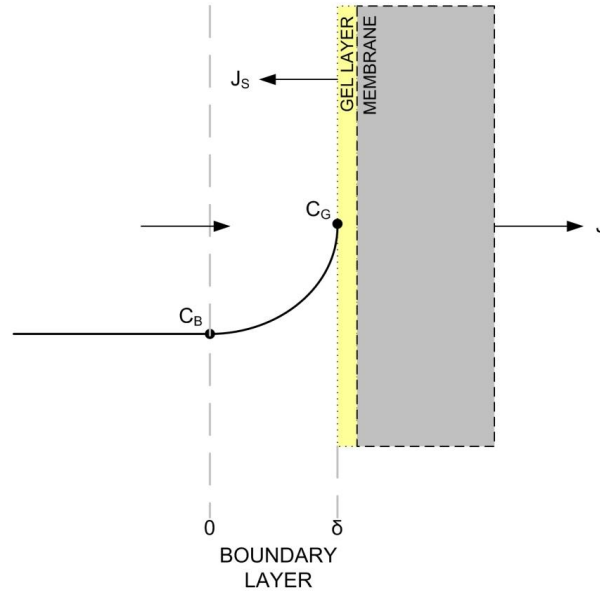


Figure 2-3: Illustration of gel layer model of concentration polarization

At steady-state, mechanisms that describe the rate that solute molecules are brought to the membrane surface and the rate of back transport of particles from the membrane surface are equated and integrated over the boundary layer from 0 to δ , resulting in the following equation for the permeate flux (Um et al., 2001).

$$J = \frac{D}{\sigma} \ln \frac{C_G}{C_B} = k \ln \frac{C_G}{C_B} \quad (5)$$

In this equation, k is the mass transfer coefficient of the solute, C_G is the gel layer concentration, and C_B is the bulk concentration of the solute. For a recycle operation where the retentate is returned to the feed, a concentration factor, CF , is usually used. This is defined as shown in Equation (6), where V_F is the initial volume in the tank, while V_t is the volume remaining in the feed tank after time t .

$$CF = \frac{V_F}{V_t} \quad (6)$$

By combining Equation (5) and Equation (6), the permeate flux equation can be rewritten as follows:

$$J = k \ln \frac{C_G}{CFC_o} - k \ln CF \quad (7)$$

Equation (7) includes the initial concentration of the solute in the feed, C_o .

2.2 Membrane Fouling

Fouling is a major concern when considering membrane filtration systems. Fouling refers to the build-up of compounds on the surface or within the pores of the membrane, which leads to a reduction in the permeate flux at constant pressure (Kennedy et al., 2008). The various types of membrane fouling are discussed further in Section 2.2.2.

The rate of fouling of a membrane depends on the type/configuration of the membrane module and flow scheme, the material of the membrane and the composition of the feed. Dead-end filtration systems in general foul faster than cross-flow systems because the flow is directed perpendicular to the membrane surface to achieve 100% recovery. This means that all of the compounds being removed from the feed is retained by the membrane. In cross-flow systems, the feed flows parallel to the membrane surface, allowing only a percentage of recovery. The compounds being removed may adsorb onto the surface of the membrane or within its pores or they may continue to the retentate flow.

Hydrophobic membranes have a higher potential to fouling effects than hydrophilic ones due to the attraction of proteins and humic substances (Kennedy et al., 2008; Yu et al., 2008).

Methods to reduce the effect of fouling in membrane filtration systems include the following:

- Periodic backwashing of the system
 - While the effect of fouling is not completely reversible, backwashing allows for the membrane to be used for a number of filtration cycles before disposal is necessary.
- Chemical cleaning of the membranes
 - This typically requires the unit to be switched offline.
 - Chemical treatment may also damage or reduce the lifespan of the membrane.
 - This step should only be used when backwashing cycles no longer improve the performance of the membrane to an acceptable level.

- Incorporate pre-treatment methods such as coagulation and sedimentation to protect the membrane filtration system.
- Use ultrafiltration prior to reverse osmosis processes, thereby protecting the reverse osmosis membranes from excessively large solute molecules.
- Use coarse air diffusers to scour the surface of the membranes, removing adhered solids (Noble, 2006).

While the mechanisms involved in the fouling of membranes have been proposed, the quantification of the effect of basic operating parameters are not fully understood. There are no theoretical models to accurately predict ultrafiltration performance (Vela et al., 2008). Instead, empirical and semi-empirical models are used.

2.2.1 Empirical Equations

There are many empirical models to be found in literature, showing high precision for specific applications (Bhattacharjee and Datta, 2003; Ahmad et al., 2006). However, these models usually require extensive pilot and full scale tests in order to obtain the required constants to predict the permeate flux. These constants also have little physical meaning. The models also offer limited insight into the mechanisms of the fouling for specific applications.

2.2.2 Semi-Empirical Equations

Semi-empirical models use parameters with physical meanings, and can be used to accurately predict the decline of permeate flux achieved while identifying the mode of fouling concurrently (Vela et al., 2008). One such model is the resistance-in-series model, where the permeate flux is related to the transmembrane pressure and the total resistance to the permeate flow, R_{TOT} , as shown in Equation (8) (Viadero et al., 1999). The total resistance is a combination of three terms, the membrane resistance, R_M , the fouling resistance, R_F , and the concentration polarization layer resistance, R_{CP} . The fouling resistance can be further divided into two parts, R_C for the resistance of the cake, and R_p for the pore blocking resistance.

$$J = \frac{\Delta P}{\mu R_{TOT}} = \frac{\Delta P}{\mu(R_M + R_F + R_{CP})} \quad (8)$$

The resistance-in-series model is able to predict the permeate flux in both the pressure-dependent and the pressure-independent regions, as well as to differentiate between the effect of the three

resistances listed above. However, as mentioned previously, it has the limitation of performing well only for colloids and monodispersed particles (Shirazi et al., 2010).

Many of the models proposed for predicting permeate flux is based on the resistance-in-series model, but includes various methods to determine each resistance term. The Carman-Kozeny equation can be used to determine the cake resistance based on properties of the cake layer such as cake layer thickness and void fraction of the cake (Shirazi et al., 2010). However, these parameters are difficult to measure.

Song & Elimelech (1995) proposed an important dimensionless filtration number that characterizes the extent of the concentration polarization and the behaviour of the permeate flux. This filtration number can be used to determine R_{CP} , but it requires the determination of the pressure drop across the concentration polarization layer.

To determine the membrane resistance, the measured permeate flux of pure water can be used (Shirazi et al., 2010). It can also be determined theoretically using the Hagen-Poiseuille equation if the membrane is assumed to have cylindrical pores with no tortuosity.

While the resistance-in-series model has performed well for predicting the permeate flux, it offers little insight into the mechanisms of pore blocking. One of the most reputable set of semi-empirical models for ultrafiltration under constant pressure operation for characterizing the form of pore blocking are Hermia's models (1982). Hermia's models are based on the characteristic form of blocking filtration laws, shown in Equation (9). The parameter n differs for the various modes of fouling: complete blocking, intermediate blocking, standard blocking, and cake layer formation. These modes of fouling are illustrated in Figure 2-4.

$$\frac{d^2t}{dV^2} = \beta \left(\frac{dt}{dV} \right)^n \quad (9)$$

The mode of fouling experienced depends on the presence of particles either larger or smaller than the pore size of the membrane used. In the complete blocking mode (Figure 2-4(a)), the particles are larger than the pore size. There may or may not be adsorption of the particles onto the surface of the membranes. The intermediate blocking mode, the particles are of similar size to the pore size of the membrane, causing obstruction of the pores. There is also a reduction of the pore size for pores where there is a build up of particles near the pore entrance. Typically, it is assumed that the particles are chemically adsorbed to the surface, and particles arriving to the membrane are blocked

by already adsorbed particles. Standard blocking involves particles smaller than the membrane pore size. Here, the particles adsorb onto the walls of the pores, essentially restricting the flow through them. These modes of fouling are considered pore-blocking and are usually irreversible.

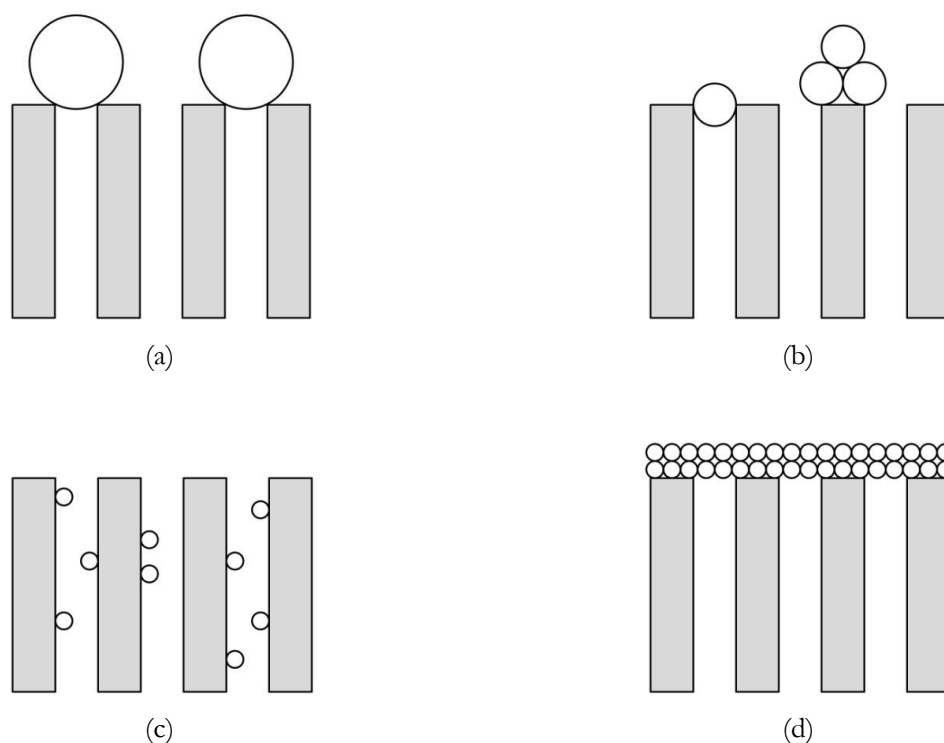


Figure 2-4: The four basic types of fouling considered by Hermia's models (a) complete blocking (b) intermediate blocking (c) standard blocking (d) cake layer formation (adapted from Vela et al., 2008)

The final mode of fouling considered by Hermia's models is the formation of a cake layer. Particles involved in the cake layer may be larger or smaller than the membrane pore size and is due to a build up of particles on the surface.

It has been proposed that the consecutive steps in the membrane fouling process entail the following, occurring successively or simultaneously (Bowen et al., 1995):

- Blockage of the smallest pores by particles arriving at the membrane (complete blocking)
- Coverage of the inner surfaces of larger pores (standard blocking)
- Particles arriving to the membrane blocks some of the remaining pores, while other particles cover particles already blocking pores (intermediate blocking)
- Build-up of a cake layer (cake filtration)

This sequence has been reported to be valid for a number of system configurations. One such system involved the ultrafiltration of poly(ethylene glycol) solutions using monotubular ceramic

membranes (Vela et al., 2008). Another study to validate this was performed by Hwang and Lin (2002), where polymethyl methacrylate (PMMA) suspensions were separated by membrane filters of various materials.

Hermia's models were developed for dead-end flow but have been applied to cross-flow systems with varying success rates (Hwang et al., 2007; Vela et al., 2008). In experiments performed by Vela et al. (2008), they were used to determine which effect dominates the mode of fouling occurring for their system as described above. This was accomplished by calculating the coefficient of determination, R^2 , values of the fit with each of the models of fouling shown in Table 2-2. It should be noted that the models presented in the table were derived from Equation (9), simplified to terms involving the permeate flux, J , and the initial permeate flux, J_0 , with the value of n being specified by the mode of fouling (Salahi et al., 2010). Also, using Equation (9), the values of n were determined for some of the experimental trials and compared to the theoretical values given for each model of fouling.

Table 2-2: Hermia's models adapted for each model of fouling

Fouling mechanism	β	n	Model
Complete pore blocking	$K_b = u_0 \sigma$	2	$\ln(J) = \ln(J_0) - K_b t$
Standard pore blocking	$K_s = \frac{2C}{LA} Q_0^{\frac{1}{2}}$	3/2	$J^{-0.5} = J_0^{-0.5} + K_s t$
Intermediate pore blocking	$K_i = \frac{\sigma}{A_0}$	1	$J^{-1} = J_0^{-1} + K_i A t$
Cake Filtration	$K_c = \frac{\alpha \gamma s}{AR_M Q_0 (1 - ms)}$	0	$J^{-2} = J_0^{-2} + K_c t$

The constants listed in Table 2-2 depend on many variables. The complete pore blocking constant, K_b , uses the linear velocity of the filtrate, u_0 , and the blocked area per unit of filtrate. The standard pore blocking constant, K_s , requires the volume of solid particles retained by the membrane per unit filtrate volume, C , the membrane thickness, L , the initial active membrane surface area, A , and the initial feed flow rate, Q_0 . The constant for the intermediate blocking model, K_i , depends on the ratio of the blocked area per unit of filtrate, σ , to the clean membrane surface area, A . The cake layer formation constant, K_c , uses the specific cake resistance, α , the density of the filtrate, γ , membrane surface area, A , the membrane resistance, R_M , the feed flow rate, Q_0 , the mass ratio of wet to dry cake, m , and the mass fraction of solids in slurry, s .

2.3 Factors Affecting Fouling

Salahi et al. (2010) reports that the four most important parameters that affect fouling are feed temperature, transmembrane pressure, cross-flow velocity, and feed pH. The following sections deal with some of the past work investigating these parameters on the effect of fouling.

2.3.1 Temperature

The analyses performed by Salahi et al. (2010) on the effect of temperature on the ultrafiltration of oil wastewater showed that at higher temperatures, the permeate flux decreases at a lower rate, indicating lower degrees of fouling. It should be noted that polymer membranes were utilized in the study performed by Salahi et al. (2010).

A similar effect was found for reverse osmosis filtration of NaCl-water solutions, where changing the feed temperature from 20°C to 40°C showed an increase of up to 60% of the permeate flux achieved (Goosena et al., 2002). However, at a median temperature of 30°C, the permeate flux achieved was lower than at 20 or 40°C. Since this trend was also consists whether using NaCl-water solutions or pure feed water, they suggest that the increase in flux between 30°C and 40°C may be a result of the polymeric membranes undergoing physical changes such as a change in the pore size, or it may be due to an increase in the diffusivity of the water in the membrane.

In another study involving the separation of oil in water emulsions using reverse osmosis, it was found that the permeate flux increased significantly when the temperature was increased from 20°C to 50°C (Mohammadi et al., 2003). Here, the authors proposed that this increase was due to the reduction in the viscosity of the feed as the temperature was increased.

2.3.2 Cross-Flow Velocity

The cross-flow velocity is defined as the superficial liquid velocity of the feed stream travelling parallel to the membrane surface. It is typically varied by controlling the feed flow rate, and calculated as the feed flow rate divided by the cross-section area of the flow path.

The effect of the cross-flow velocity on permeate flux has been studied for a wide variety of feed solutions. It is believed that increasing the cross-flow velocity positively affects the mass transfer coefficient of the solute and the extent of mixing near the membrane surface (Salahi et al., 2009). This higher extent of mixing experienced with larger cross-flow velocities leads to a reduction of aggregation of the feed solids in the gel layer, essentially increasing the diffusion of these

components back towards the bulk (i.e. increasing J_s in Figure 2-3), leading to an overall reduction in the effect of concentration polarization.

2.3.3 Transmembrane Pressure

The transmembrane pressure is the pressure difference between the feed and permeate stream. The control of the transmembrane pressure is essential in ultrafiltration systems as it greatly affects the permeation rate. At higher transmembrane pressures, the force of the fluid flowing towards the membrane is increased, leading to higher permeate flux. However, there is an increased probability of breakthrough of particles from the feed to the permeate.

With increasing transmembrane pressure, there are two distinct regions that are evident, as depicted in Figure 2-5 (Kohuniewicz, 1992). In the first region, the permeate flux increases proportionally with the transmembrane pressure. However, at higher transmembrane pressures, the second region, the permeate flux plateaus at a value, termed the "limiting flux" (Wijmans et al., 1984). It is proposed that in this region, the flow of the solute towards the membrane surface is affected greatly by the hydrodynamic conditions near the membrane since there is also movement of the solute from the membrane surface towards the bulk, as well as shear stresses and turbulence effects due to the direction of the flow (Kohuniewicz, 1992).

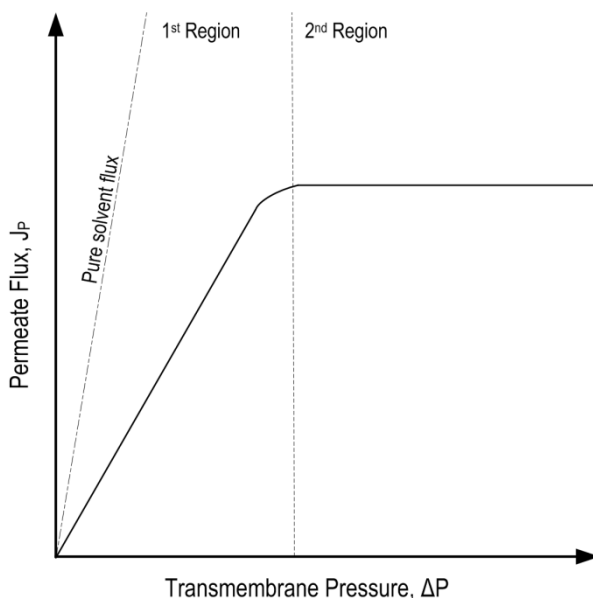


**Figure 2-5: Pressure-flux characteristic in cross-flow ultrafiltration
(adapted from Kohuniewicz, 1992)**

The nature of particles in the feed also affects the transmembrane pressure. Particles that are deformable such as poly(ethylene glycol) will result in increased cake density, resistance and

compression, as well as a sooner decline in the permeate flux at higher transmembrane pressures (Vela et al., 2008).

2.3.4 Constituents in the Feed/Model Chemicals

If sample wastewater from industrial effluents are unavailable, or to investigate specific applications of membrane filtration, studies typically employ feed solutions comprised of model chemicals. There have been a very wide range of these model chemicals used to investigate the fouling phenomena of membranes. The selection of these chemicals are usually based on the industry or application under investigation such that the chemicals will behave similarly to the actual stream to be filtered.

For example, when desalination is being studied, NaCl solutions have been used to investigate the fouling of a particular type of membrane (Goosena et al., 2002). One of the most common chemicals used to investigate fouling is poly(ethylene glycol), or PEG (Vela et al., 2008). It is considered a standard macromolecule and has been utilized in studies ranging from examining various ultrafiltration cell geometries such as a radial cross-flow cell (Ganguly and Bhattacharya, 1994) to developing models for pore-plugging (Ghose et al., 2000).

In this study, solutions of latex paint and water were used to simulate the wastewater produced in latex paint manufacturing plants during reactor/mixer cleaning as previously discussed. More details on the composition of this solution is described in Chapter 3.

2.4 Micellar-Enhanced Ultrafiltration

Surfactants are molecules that contain a hydrophobic tail (usually long chain hydrocarbons) and a hydrophilic head (for example sulfate groups). Above a specific concentration of the surfactants, the surfactant molecules move together to form clusters or micelles as illustrated in Figure 2-6. This concentration is termed the critical micelle concentration and differs depending on the type of surfactant.

There are numerous types of surfactant used in industry today, categorized by the charge of the hydrophilic portion of the molecule in the following four groups: anionic (negative charge), cationic (positive charge), non-ionic (neither positive nor negative charge), and zwitterionic (both positive and negative charges).

Micellar-enhanced ultrafiltration is an emerging technique that it used to improve the performance of the ultrafiltration process. It involves the addition of surfactant above its micelle concentration in

order to promote the dissolving of constituents in the feed in the formed micelles. Essentially, this would increase the size of the particles found in the feed, allowing the use of membranes with larger pore sizes for the same application.

The selection of the type of surfactant depends on the constituents of the feed solution being removed. A study has been conducted to compare the use of dodecylbenzenesulfonic acid (DSA) as an anionic surfactant and dodecylamine as a cationic surfactant to improve the removal of heavy metal ions (lead and arsenic) from municipal wastewater (Ferella et al., 2007). It was concluded that while both surfactant types enhanced the separation of the heavy metals, the cationic surfactant performed better than the anionic.

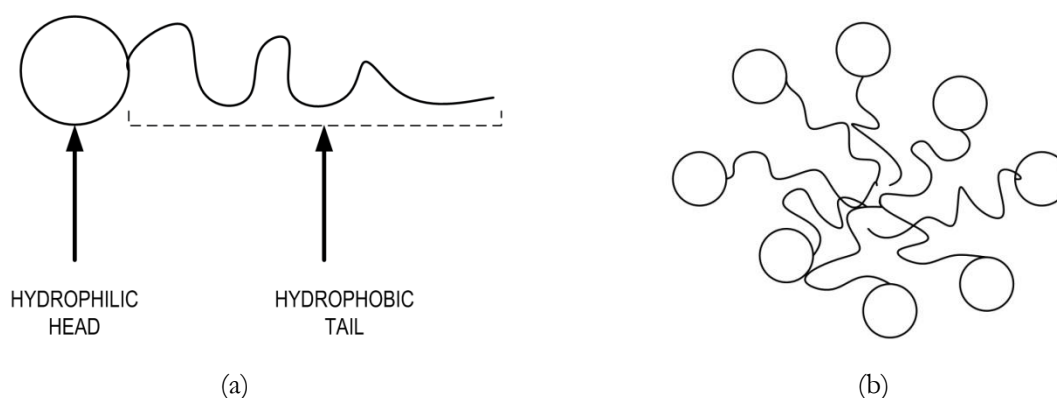


Figure 2-6: Illustration of (a) surfactant molecule (b) micelle composed of a number of surfactant molecules

The effectiveness of micellar-enhanced ultrafiltration also depends on the type of material of the membranes and its surface charge. The charge on the surface of the formed micelles is dictated by the type of surfactant used. If the charge on the membrane is opposite to the micelle surface charge, there will be an unwanted attraction of the micelles to the membrane surface, and increased probability of chemical adsorption (Gelinas, 1995). This would increase the fouling effect experienced during the ultrafiltration process.

Based on the above literature review, the effect of the main operating parameters of the ultrafiltration process (transmembrane pressure, cross-flow velocity through feed flow rate, and feed concentration) on the permeate flux over time will be investigated. The effect of surfactant addition on the permeate flux will also be considered, comparing the application of both cationic and anionic surfactants. The materials and methods used in this study is presented in Chapter 3.

Chapter 3

Materials and Methods

In this section, details of the experimental setup and procedure are summarized, followed by a brief description of some of the analytical methods used during the study.

3.1 Filtration Experiments

3.1.1 Experimental Setup

A schematic diagram of the experimental setup is shown in Figure 3-1. It includes a feed pump rated at 1.0 hp and 100 psi. and a volumetric flow meter ranging from 0.0 to 5.0 L/min (accurate to ± 0.25 L/min). Monitoring of the pressure was accomplished using a pressure transducer. The permeate stream was continuously measured gravimetrically using an electronic balance, ± 0.1 g (Model Adventurer Pro AV2101, Ohaus Corporation, New Jersey, USA). Both the pressure transducer ($\pm 0.25\%$ BFLS) and the electronic balance were connected to a nearby computer, allowing for automatic data acquisition of the required parameters.

The membrane filtration unit was constructed for centre-fed operation out of a block of acrylic, as shown in Figure 3-2. The permeate exited the cell through a small opening in the upper cavity while the retentate was directed through a port located along the side of the cell. The flat-sheet membrane was cut to size and placed under a porous stainless steel disc for support. O-rings were used to seal the unit, equipped with large bolts at four points around the cell's circular peripheral. Details of the

dimensions of the unit, as well as a determination of the flow regime through the cell, are presented in Appendix C.

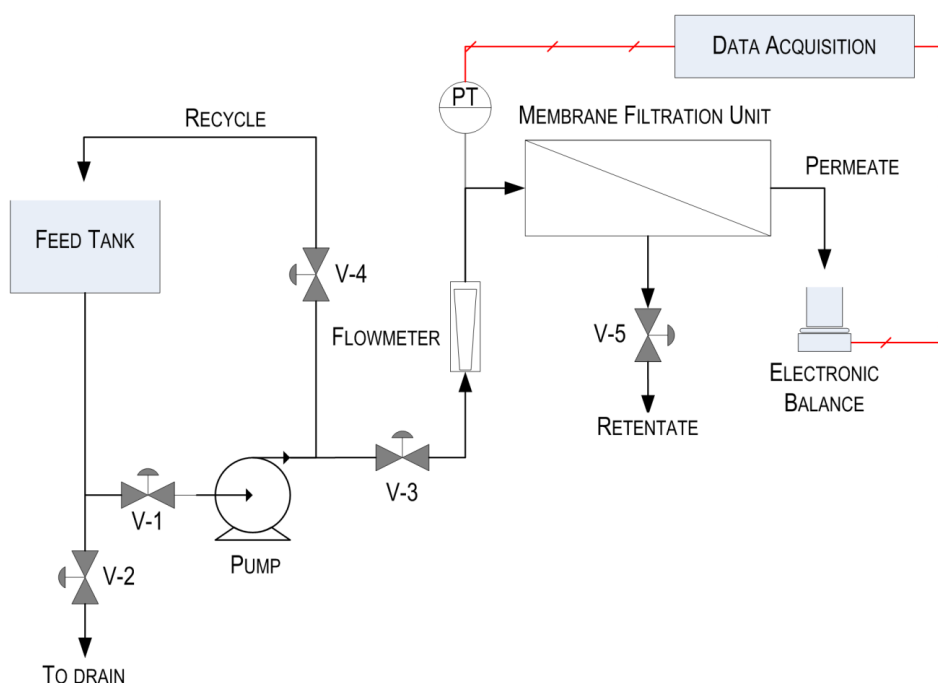


Figure 3-1: Schematic diagram of the experimental setup

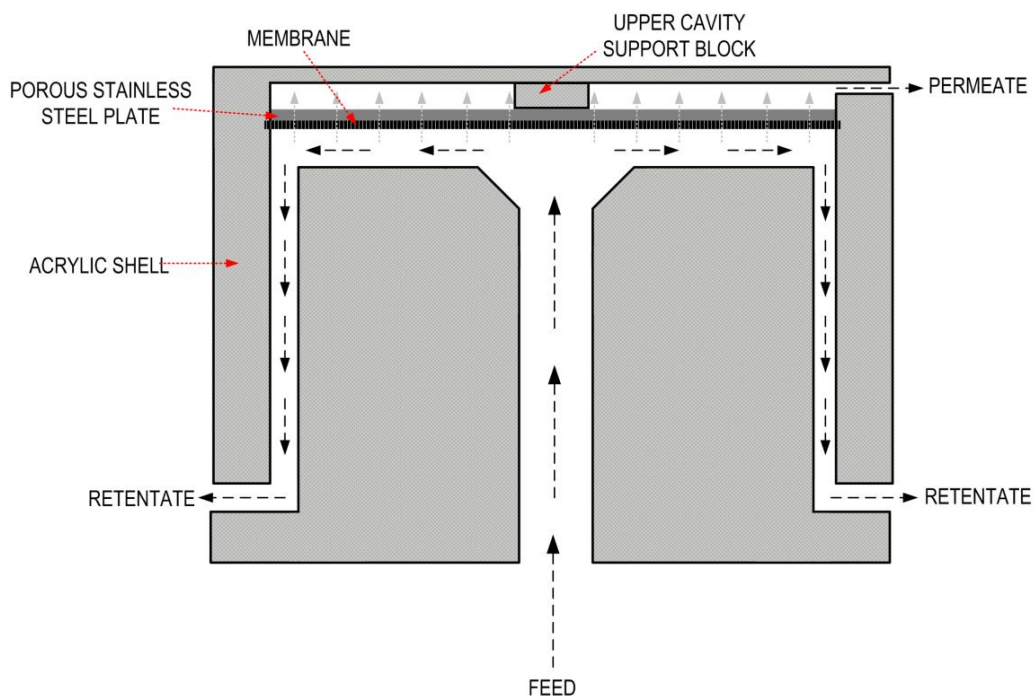


Figure 3-2: Cross-section schematic view of membrane filtration unit

3.1.2 Ultrafiltration Membranes

Polycarbonate membrane filters with a nominal pore size of 0.1 μm (GE Water & Process Technologies, CAT #: K01CP00010) were used for these experiments. These membranes were manufactured using track etching, which involves the exposure of the thin, smooth, polycarbonate sheets to charged particles in a nuclear reactor (General Electric Company, 2009). Pore size of the membrane sheets are determined by controlling the strength, temperature, and exposure time of the etching solution (General Electric Company, 2009; Apel, 2001). This method allows for precisely controlled cylindrical pores with a narrow pore size distribution to be achieved. The membranes are also coated with a wetting agent, polyvinylpyrrolidone (PVP), in order to ensure that the surface of the membrane is hydrophilic. The membrane filters were available in large sheets, 300mm x 3000mm in size, which were easily cut to the desired shape and dimensions. Data on the membrane sheets are shown in Table 3-1 below.

Table 3-1: Membrane properties

	Units		Notes
Pore Size	μm	0.1	+0%, -20% (NOTE: maximum pore size with up to 20% being lower than this)
Pore Density	pores/ cm^2	4×10^8	$\pm 15\%$
Nominal Weight	mg/cm^2	0.7	
Nominal Thickness	μm	6	$\pm 10\%$
Minimum Water Flow Rate	$\text{mL}/\text{min}/\text{cm}^2$	2.5	Measured using pre-filtered water at 10 psi

3.1.3 Preparation of Latex Paint Dispersions to Simulate Wastewater

In a large tank, a measured volume of latex paint (Type: Glidden Easyflow Interior Latex Paint, White, Flat) was added to distilled water using a syringe as a pump circulated the water through a recycle line. The latex paint is a combination of many ingredients. Vinyl acrylic latex is used as the binder. However, the exact composition of the paint is proprietary. For each experimental run, approximately 60L of latex paint dispersion was prepared. The volume of latex paint used varied with the solid concentration required for the trial, and samples were taken to determine the solid concentration of the mixture as outlined below (see Section 3.2.1). As an example, in order to obtain a feed solid concentration of 0.12%, 2.5 mL of latex paint was added using a syringe for each litre of distilled water used. The feed stock solution was transferred to the smaller feed tank connected to the main equipment setup, and periodically throughout the experimental trial, this feed tank was refilled.

3.1.4 Operating Parameters

The parameters that were controlled in each experimental run were the feed flow rate, the feed pressure, and the solid concentration of the synthetic wastewater. The temperature of the suspension used was kept at room temperature, ranging between 22-24°C. It was desired to investigate the effect of feed flow rate on the permeate flux achieved. Flow rates ranging from 1.0 to 3.0 L/min were used. Similarly, experimental trials with varying operating pressures ranging from 1.5 to 5.5 psi., and varying feed solid concentration from 0.04% to 0.21% were also performed. When investigating each parameter, the other parameters were kept constant at the midpoint. For example, when investigating the effect of feed flow rate, the pressure and feed solid concentration were set to 3.5 psi. and 0.12% solids respectively for each experimental trial.

To determine the effect of surfactant addition on permeate flux, an anionic surfactant, sodium dodecyl sulfate (SDS) (Molecular Biology Grade, Calbiochem, CAT #: 219374) was used in concentrations varying from 25 to 200% of the critical micelle concentration (CMC), reported to be 0.0082 M (Murkerjee and Mysels, 1971). To achieve the CMC concentration, SDS was added to approximately 2.36 g/L of the feed stock solution prepared. A similar approach was adopted for the cationic surfactant, cetyl trimethylammonium bromide (CTAB) (Molecular Biology Grade, Calbiochem, CAT #:428023) with a reported CMC of 0.00092M. Here, 0.33 grams of CTAB was added per litre of feed stock solution prepared.

Experiments using clean distilled water were performed to determine the clean water flux through the membrane at various operating pressures and feed flow rates. The results are presented in Appendix A. Repeats at specific operating conditions were also performed, as shown in Appendix D. From these, it was shown that the constants K_p and F_M showed a standard deviation of 4.98×10^8 and 8.51×10^4 , respectively.

3.1.5 Operating Procedure

Discs of the membrane were cut from a large roll of the PCTE membrane sheet to the required size and affixed to the membrane filtration unit. After the synthetic wastewater was prepared in the large tank, it was transferred to the feed tank shown in the experimental setup in Figure 3-1. The recycle valve (V-4) was set to fully open, and the pump was switched on, allowing the solution to mix in the tank via the recycle line.

At the start of the experimental run, the feed valve (V-3) and the retentate valve (V-5) were opened slowly in order to set the pressure and flow rate to the appropriate values desired. If a high pressure was necessary, the retentate valve (V-5) would be opened less than for lower operating pressures at the same feed flow rate, while the feed valve (V-3) would be opened slightly more. Measurement of the pressure of the stream entering the filtration unit was done using an electronic pressure sensor (PT), rated from 0.0 to 30 psi. The pressure reading was displayed on a computer monitor through NI LabVIEW located near the unit, and was recorded at one second intervals.

The permeate stream was collected on an electronic balance, rated from 0 to 2.1 kg. This electronic balance was also connected to the nearby computer that allowed for the automatic recording of the mass of the permeate collected over time using Windows HyperTerminal, at set time intervals of 20 seconds. Permeate was collected for approximately 30 minutes during each run.

During an experimental trial, the pressure and feed flow rate varied as the membrane was fouled. Therefore, it was necessary to monitor these parameters. If the operating pressure increased above the desired value, the retentate valve (V-5) was opened slightly in order to relieve the pressure build-up. While this reduces the pressure of the stream entering the filtration unit, the flow rate of the feed may also have been increased, requiring the position of the feed valve (V-3) to be partially closed.

3.2 Analytical Methods

3.2.1 Solid Concentration

Samples of the feed and the permeate streams were collected for each experimental run. From these, measured masses of each dispersion were transferred to metal dishes that were placed in an oven at 105°C for an extended period of time, over one week. The mass of each dish was periodically measured, approximately every three days, until there was no change.

3.2.2 Particle Size Distribution of Latex Paint Dispersions

The particle size distribution of the synthetic wastewater used in the experiments was determined using a particle size analyzer (Model S3500, Microtrac, Montgomeryville, PA, USA). This equipment uses a patented tri-laser technology to determine particle sizes of dilute solutions through light scattering, as shown in Figure 3.3. Laser 1 results in light scattered on-axis to 60 degrees, which is measured by the on-axis array of detectors. Laser 2 is known as an off-axis laser, allows scattering

above 60 degrees to be produced, and is detected by the off-axis array. Laser 3 produces backscattered light that is also detected by the off-axis array.

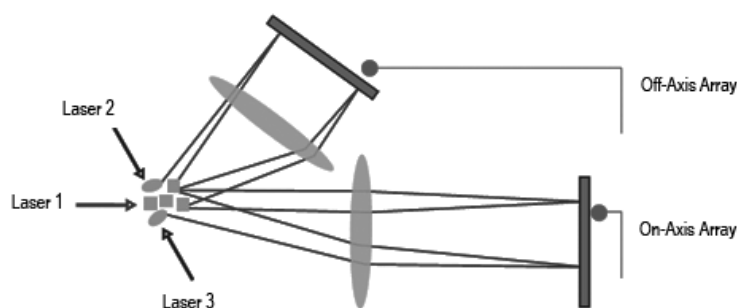


Figure 3-3: Microtrac S3500 operating schematic diagram (Microtrac, 2008)

The S3500 used has a resolution of 0.24-2800 μm . While this data does not represent all of the particles found in the latex paint dispersions, it can still provide insight into the larger particles present. The results for a typical feed solution are displayed in Figure 3-3. The majority of samples collected of the feed stream had a similar distribution since the concentration of samples did not directly affect the particle size distribution obtained. Permeate samples showed low amounts of particles within the range of sizes the equipment was capable of measuring.

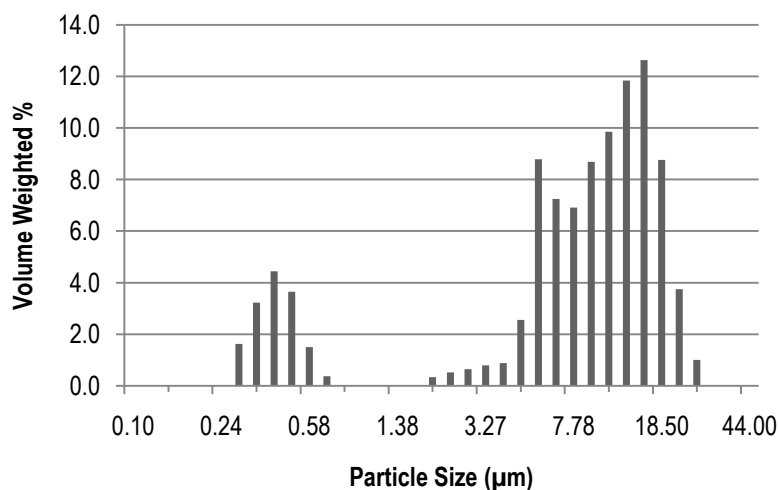


Figure 3-4: Particle Size Distribution of Latex Paint Dispersion

3.2.3 Scanning-Electron Microscopy (SEM)

To obtain surface images of the membrane before and after filtration, a scanning electron microscope (Model JEOL, JSM-6380 LV, Oxford Instrument, U.K.) was used. Shown in Figure 3-5 are those obtained after scanning a sample of a clean membrane. The sample was coated with a thin layer of gold particles to improve the resolution of the images. Figure 3-5(a) shows that the surface

of the membrane had a high pore density, but the pores were arranged in a random distribution. Figure 3-5(b) zooms into an area of the membrane surface. From this image, it can be seen that the pores are predominantly circular (or cylindrical) in nature. Measuring of the dimensions of the pore openings showed that the majority of the pore sizes was about $0.1\ \mu\text{m}$.

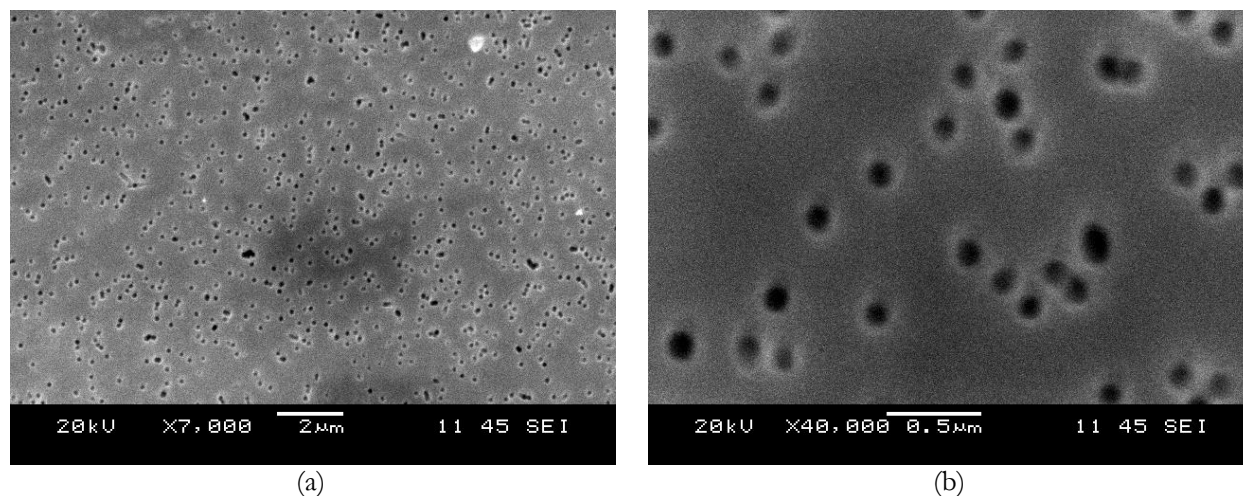


Figure 3-5: SEM image of clean membrane, gold-coated

Samples of cross-sections of the membrane were prepared by freeze-fracturing the sample under liquid nitrogen. This required small portions of the membrane to be immersed in liquid nitrogen for about 15 to 20 minutes before being pulled apart from the ends to achieve a clean edge. Because the cross-flow velocity decreases in the radial direction, a specific area from the whole membrane was segregated so that the images could be compared. This area is illustrated in Figure 3-6.

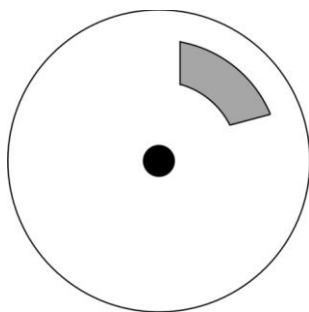


Figure 3-6: Illustration of the area of extracted samples from fouled membranes

Chapter 4

Results and Discussions

In the following sections, the results obtained from the experimental trials performed are presented. Some data manipulation is performed to determine relevant parameters required for the discussion of the effect of the pertinent parameters investigated. The mass of permeate collected over time for all filtration experiments can be found in Appendix A.

The effect of feed flow rate, transmembrane pressure, and feed solid concentration on the permeate flux is discussed, respectively. Following this, the effects of anionic and cationic surfactant addition to the feed were considered. SEM images are presented to visually describe the effects of the above parameters on the cake layer formed during the ultrafiltration process.

The mass transfer coefficient describing the transport of material across the membrane within the formed boundary layer is then discussed. An attempt is made to fit Hermia's models to the data collected in order to determine the dominant mode of fouling over time. The resistance-in-series model was applied to quantify the resistances to the permeate flow.

4.1 Effect of Feed Flow Rate on Permeate Flux

In order to investigate the effect of feed flow rate on the permeate flux, a series of five experimental trials were conducted, varying the feed flow rate from 1.0 L/min. to 3.0 L/min. The results are displayed in Figure 4-1. The initial 200 seconds were omitted due to the large fluctuations experienced in this time period. It was assumed that the system was at unsteady state for this length of time.

It was observed that over time, the permeate flux reduced dramatically at high feed flow rates. This was expected as the degree of fouling of the membrane increased with time. In general, as the feed flow rate increased, so did the initial permeate flux. It can also be said that the larger the feed flow rate, the greater the reduction in the initial permeate flux. For example, at 2.5 L/min feed flow rate, the initial flux (at steady-state) of $0.039 \text{ m}^3/\text{m}^2.\text{s}$ dropped to $0.016 \text{ m}^3/\text{m}^2.\text{s}$ after 800s of operation, showing a 59% reduction. However, for 1.0 L/min feed flow rate, the initial permeate flux of $0.007 \text{ m}^3/\text{m}^2.\text{s}$ was reduced by 28% to $0.005 \text{ m}^3/\text{m}^2.\text{s}$.

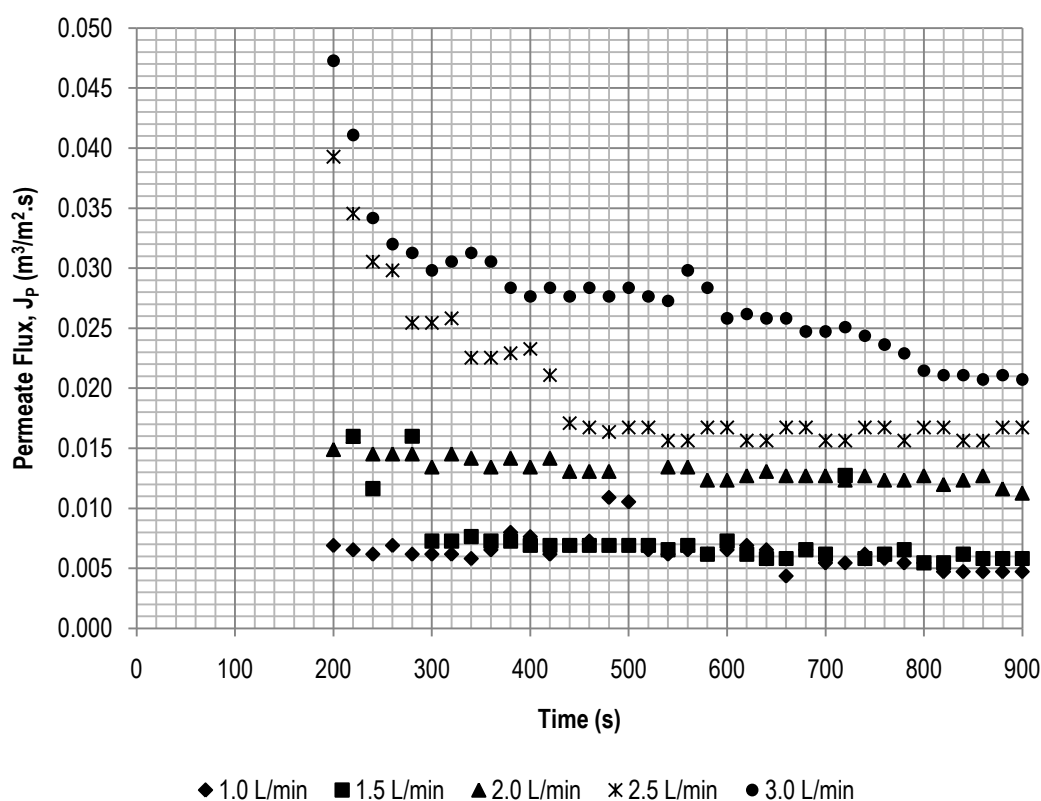


Figure 4-1: Permeate flux vs time for various feed flow rates. $P=3.5\text{psi.}$, $C_s=0.12\%$

Towards the end of the run, the permeate flux generally approached a constant value. These were displayed graphically in Figure 4-2. This plot demonstrates that when the feed flow rate was increased, the steady-state permeate flux achieved also increased. Between 1.0 L/min and 3.0 L/min, there was a 294% increase in the steady-state permeate flux achieved. Essentially, by increasing the feed flow rate, the cross-flow velocities near the surface of the membrane also increases. This may result in an increase in the number of particles that are washed away into the retentate stream, resulting in a lower degree of fouling of the membrane as well as a thinner cake layer. At higher feed

flow rates, this thinner cake would increase the mass transfer of the solute, k , as shown in Equation (5), and therefore increases the permeate flux achieved.

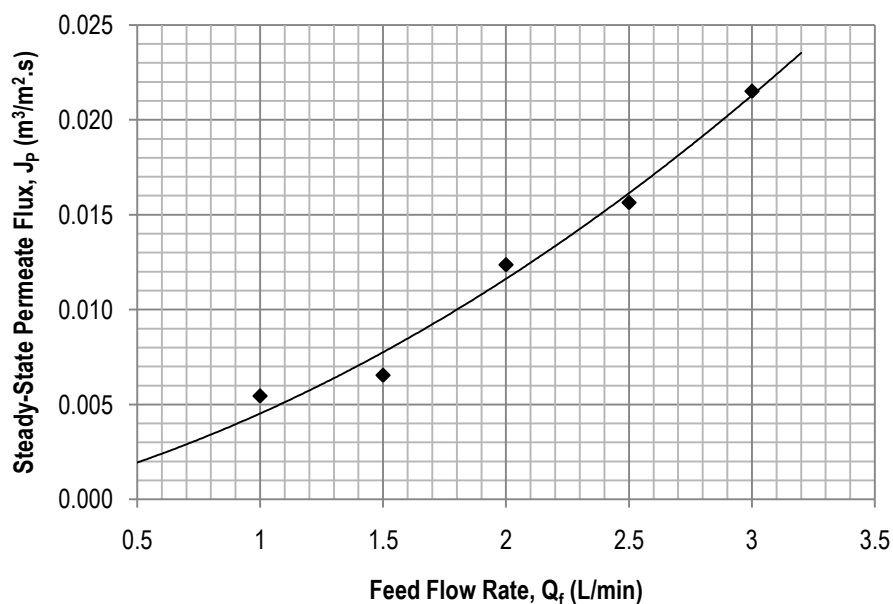
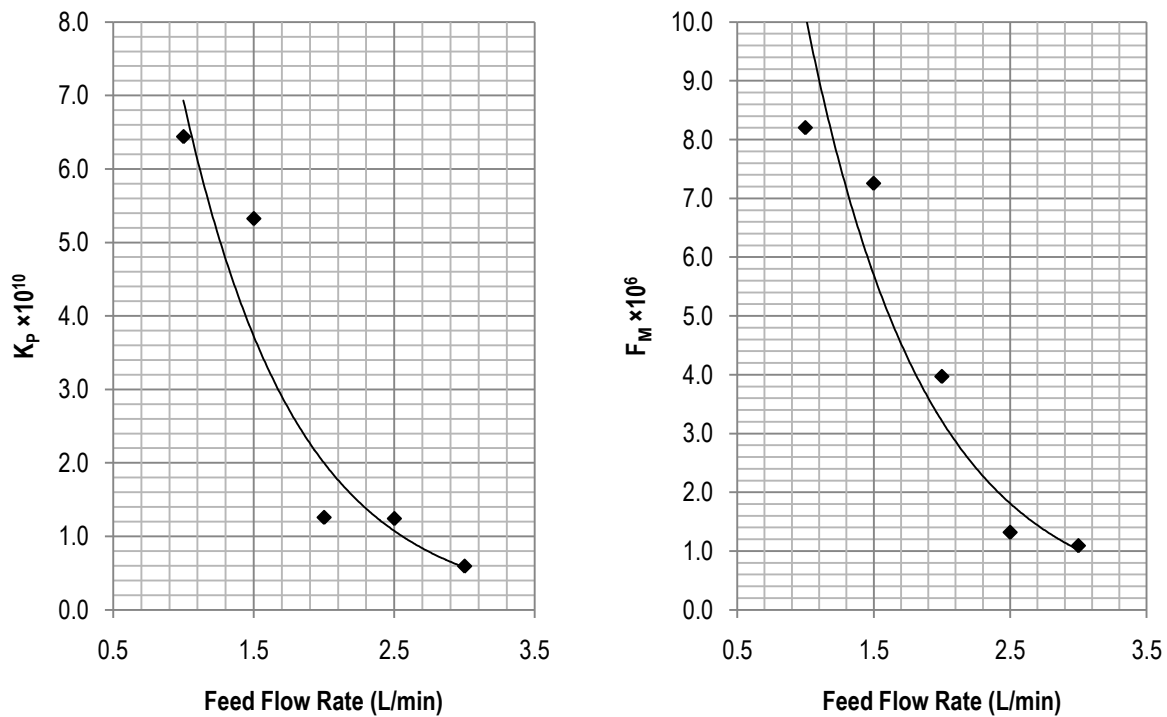


Figure 4-2: Steady-State Permeate Flux vs Feed Flow Rates at $t=800$ s

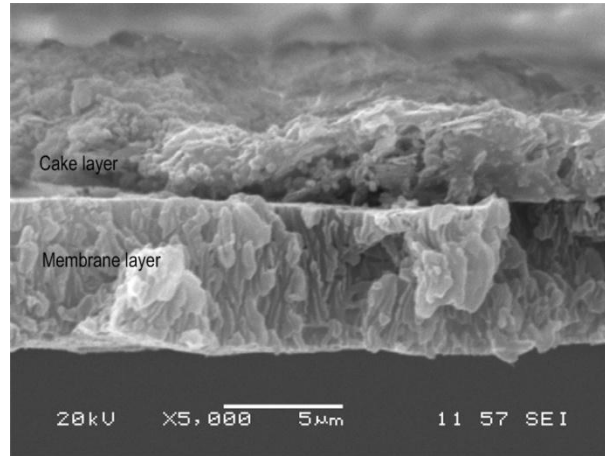
The data collected from these experimental trials were used to generate plots of t/V vs. V as discussed previously. For varying feed flow rates, these plots can be found in Appendix B (Figure B-1). From these plots, values of K_p and F_M were extracted and displayed in Figure 4-3. Figure 4-3(a) shows that the constant K_p generally decreases with increasing feed flow rates. This can be interpreted to demonstrate that as the feed flow rate is increased, the resistance due to the cake layer that has deposited on the surface of the membrane may have decreased. The cake resistance is dependent on three main factors: cake thickness, porosity, and tortuosity. As the feed flow rate is increased, the cross flow velocities also increases, resulting in an increase in the diffusion of particles from the gel layer back to the bulk. This may also lead to a more porous cake since some of the particles from the cake layer is removed. As is shown later, between 1.0 L/min and 2.0 L/min, there is an increase in the cake thickness, before a large decrease at 3.0 L/min. This reduction in the thickness results in a lower cake resistance. The increase between the lower feed flow rates can be explained by considering the compactness of the cake layer, as illustrated later. The flow regime throughout the ultrafiltration cell was laminar, as shown in Appendix C. Therefore, there should be no turbulence effects on the cake layer formed.

Similarly, Figure 4-3(b) shows that increasing feed flow rate also decreases the constant F_M , the effective membrane resistance. This may be due to an increase in the momentum experienced at the pore openings on the membrane surface. With an increase in the cross flow velocity, a larger number of the particles smaller than the membrane pore size would be swept away into the retentate stream, reducing the probability of the occurrence of standard blocking of the membrane. Less standard blocking results in a reduction in the effective membrane resistance, shown in the reduction of the constant F_M .



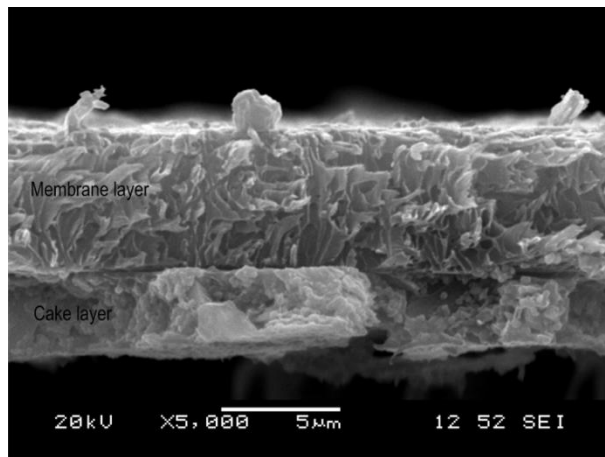
**Figure 4-3: Filtration constants obtained from t/V vs. V graphs vs Feed Flow Rate
 $P=3.5\text{psi.}$, $C_s=0.12\%$ (a) K_P (b) F_M**

Figure 4-4 displays the image obtained for the experimental trial at 2.0 L/min feed flow rate, 3.5 psi operating pressure, and a feed solid concentration of 0.12%. These values pertain to the middle value of each respective parameter investigated, allowing direct comparison to the other samples prepared. Here it is shown that the thickness of the membrane is about 6 μm . The average cake thickness was measured to be 4.6 μm . To determine these dimensions, the cake layer was measured in three positions on the image and the average was taken.

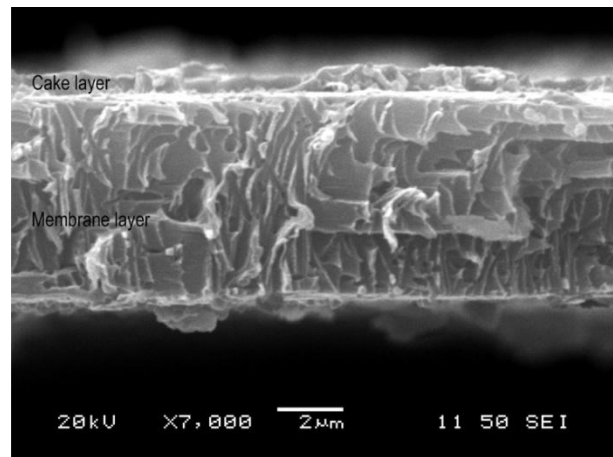


**Figure 4-4: SEM images of sample of membrane after ultrafiltration ($t = 1200s$)
 $Q_f=2.0L/min$, $P=3.5psi$, $C_s=0.12\%$**

Figure 4-5 is used to illustrate the effect of feed flow rate on the cake. Figure 4-5(a) was obtained for a sample at low feed flow rate, showing a cake thickness of $3.6 \mu m$. This is less than that achieved at the median flow rate of $2.0 L/min$ in Figure 4-4. Figure 4-5(b) shows that increasing the feed flow rate further decreased the cake thickness to about $0.83 \mu m$. It should be noted that the cake formed at the high feed flow rate was noticeably less dense, with some regions with little or no cake layer. The cake layer shown in Figure 4-4 for the median flow rate can also be considered less dense than the cake layer for the low flow rate (Figure 4-5(a)). This can be interpreted as a reduction in the cake porosity at the lower flow rate, which may explain why the cake resistance appears to decline as the feed flow rate is increased.



(a)



(b)

**Figure 4-5: SEM images of sample of membrane after ultrafiltration ($t = 1200s$)
 (a) $Q_f=1.0L/min$, $P=3.5 psi$, $C_s=0.12\%$
 (b) $Q_f=3.0L/min$, $P=3.5 psi$, $C_s=0.12\%$**

4.2 Effect of Transmembrane Pressure on Permeate Flux

A series of five experiments were conducted at various operating pressures ranging from 1.5 psi. to 5.5 psi. in order to determine the effect of operating pressure on the permeate flux. Because the permeate stream is open to the atmosphere, the gauge pressure recorded of the feed stream entering the membrane filtration cell can be equated to the transmembrane pressure of each run. Similar to the previous discussion, the initial 100s of data were disregarded due to unsteady behaviour. It was assumed that this time period corresponds to an unsteady state of operation.

As can be seen in Figure 4.6, over time, there was a decrease in the permeate flux achieved. Also, at larger operating pressures, a higher initial permeate flux was observed. This was because at higher operating pressure, there were larger forces exerted on the membrane by the feed solution to overcome the resistance to the permeate flux by the filter cake and the membrane.

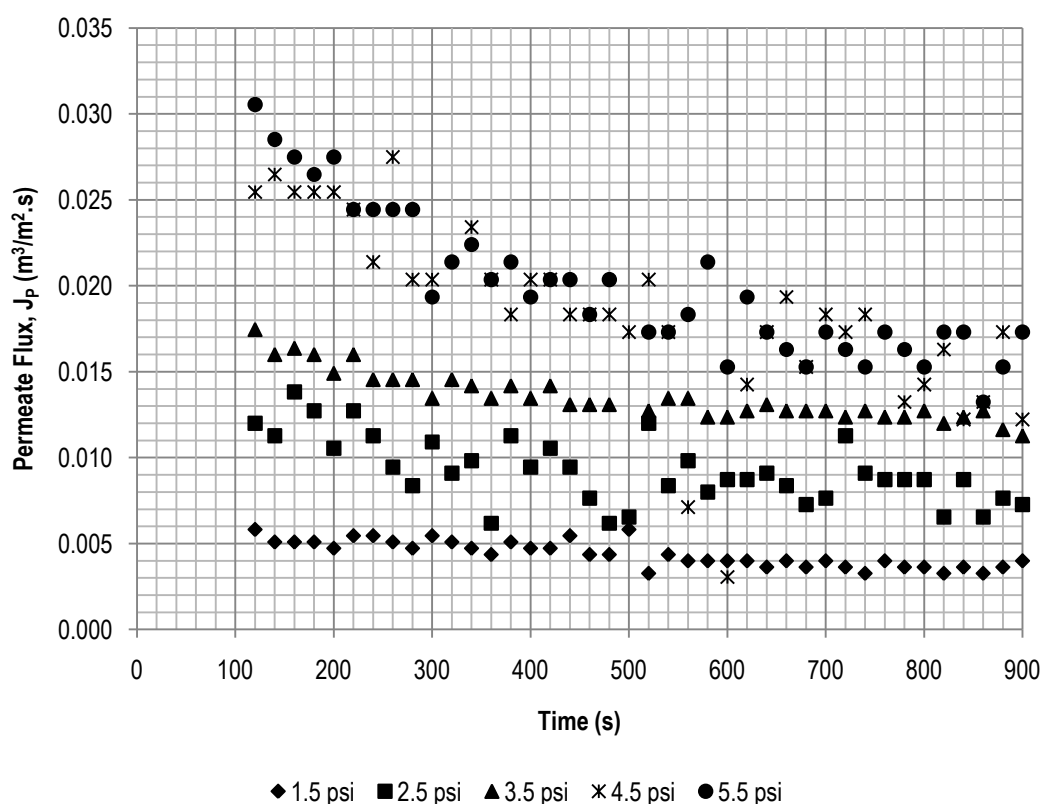


Figure 4-6: Permeate flux vs time for various transmembrane pressures, $Q_f=2.0L/min$, $C_s=0.12\%$

As with increasing feed flow rate, a similar trend was observed for increasing operating pressure in that as the operating pressure was increased, there were greater changes in the reduction of permeate flux collected after a certain period of time. For example, for an operating pressure of 1.5 psi., the

initial flux of $0.006 \text{ m}^3/\text{m}^2\cdot\text{s}$ showed a decrease of 33% to about $0.004 \text{ m}^3/\text{m}^2\cdot\text{s}$ after 800s. In comparison, at an operating pressure of 5.5 psi., a reduction of 46% was observed (from about 0.0303 to $0.0165 \text{ m}^3/\text{m}^2\cdot\text{s}$). At higher operating pressures, a larger number of particles may be moved to the membrane surface due to the increase in the forces acting on the particles in the feed stream than when lower operating pressures were used. This increased the degree of fouling of the membrane more quickly, leading to the greater reduction from the initial permeate flux to the permeate flux achieved over time at higher operating pressures.

Figure 4-7 shows that the steady-state permeate fluxes achieved at increasing operating pressures also increases. At higher operating pressures, there may have been larger forces exerted on the membrane surface by the feed stream, increasing the net flow of water to the permeate stream.

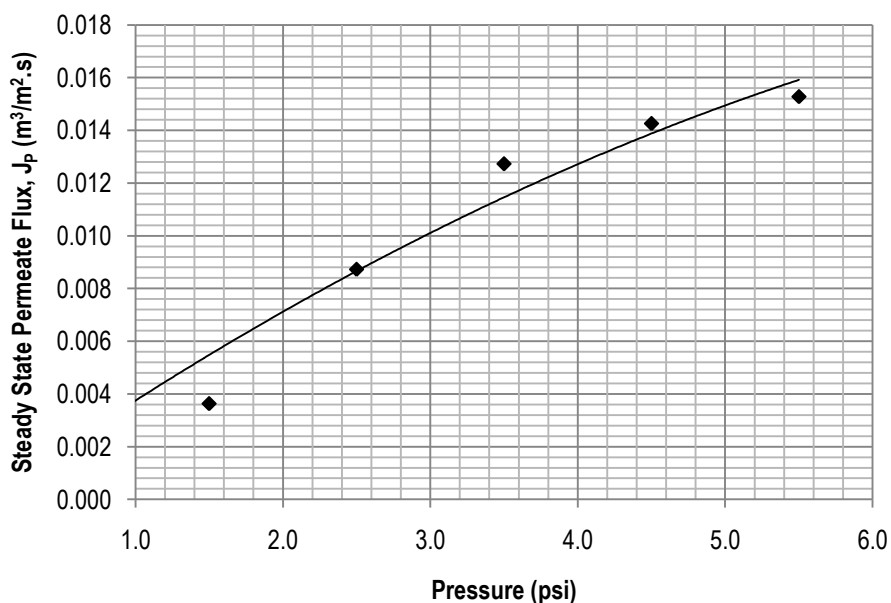
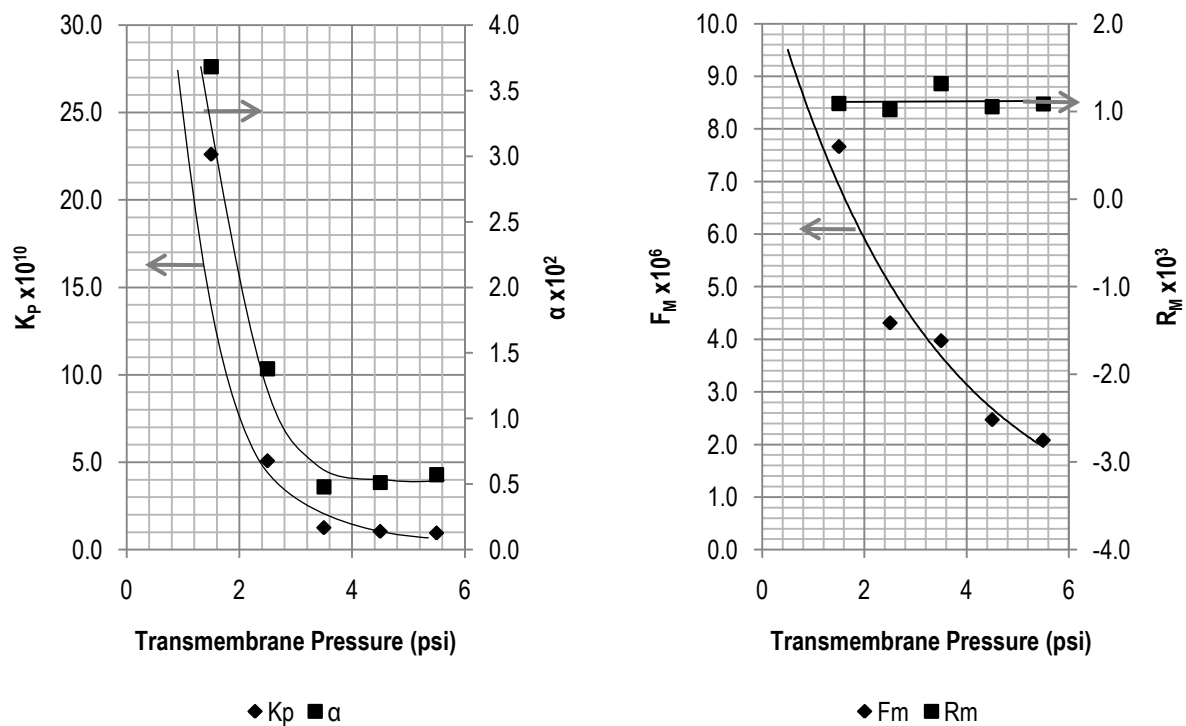


Figure 4-7: Steady-State Permeate Flux vs Transmembrane Pressure at $t=800 \text{ s}$

The experimental data collected was used to obtain the filtration constants relating to the resistance of both the cake and the membrane. These plots can be found in Appendix B (Figure B-2). Values of the constants were extracted and displayed in Figure 4-8(a) for the K_p , the resistance due to the cake, and Figure 4-8(b) for F_M , the membrane resistance.

With higher operating pressures, it was expected that the cake that accumulated on the membrane surface would be compacted, increasing the resistance due to the cake. However, as shown in Figure 4-8(a), there was a reduction in the value of K_p as the operating pressure increased. This may be because even though the cake is denser at higher operating pressures, the thickness of the cake may

be thinner due to the compacting of the layer. According to Equation (3), the constant K_p depends not only on the specific cake resistance, but also on the transmembrane pressure ΔP , and therefore, for this variable, the specific cake resistance, α should be considered. Also shown in Figure 4.8(a) is the effect of pressure on the specific cake resistance. At lower operating pressures, there is not only a lower permeate flux, but an enhanced transport of small particles to the membrane surface while the larger particles are swept back into the bulk (Riesmeier et al., 1989). This results in a classification of the particles due to the difference in the particle size. At these lower operating pressures, only the smaller particles participate in the formation of the cake layer, resulting in a more dense cake layer, and therefore an increased cake resistance since a denser cake results in a higher specific cake resistance. At higher operating pressures, the classification of particle sizes is reduced, and some of the larger particles in the feed are transported to the membrane surface. With both larger and smaller particles participating in the formation of the cake layer, the resulting cake resistance would be lower due to the lower cake layer density.



**Figure 4-8: Filtration constants obtained from t/V vs. V graphs vs Transmembrane pressure
 $Q_f=2.0\text{L/min}$ $C_s=0.12\%$**

Similarly, as the operating pressure is increased, the constant F_M decreases, as shown in Figure 4-6(b). From the definition of the F_M , Equation (4), the membrane resistance term was calculated and

displayed in the plot. Here, it is shown that this membrane resistance does not change with increasing pressure. Therefore, the reduction of the value of F_M is a result of the increasing operating pressure term located in the denominator of Equation (4).

Shown in Figure 4-9 are the SEM images for various operating pressures: (a) low pressure and (b) high pressure. In both of these images, it appears that the cake layer has a thickness of about $2.1\ \mu\text{m}$. At the median pressure, the thickness of the cake layer was higher.

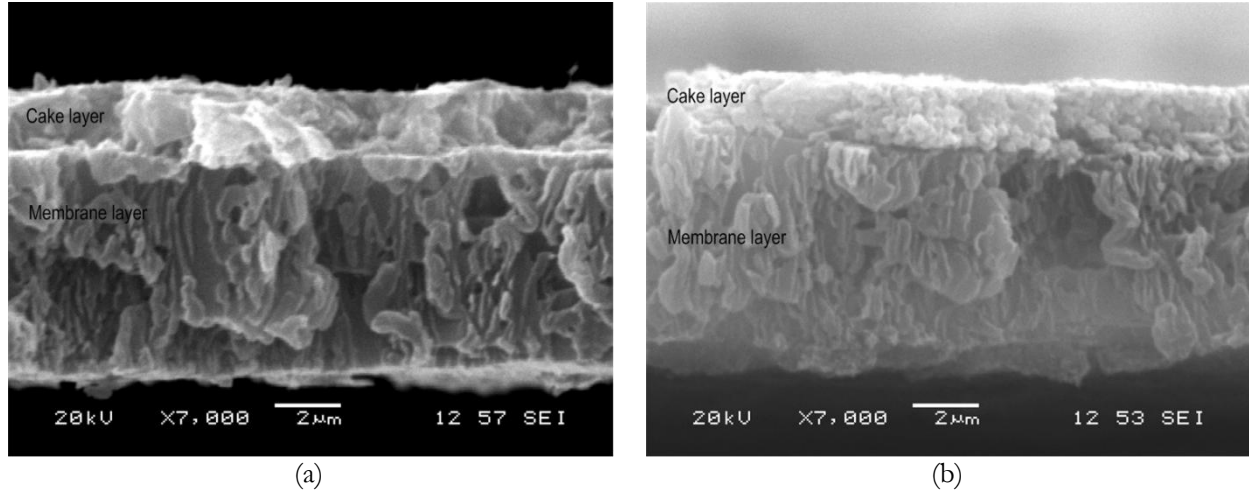


Figure 4-9: SEM images of sample of membrane after ultrafiltration ($t = 1200\text{s}$)

(a) $Q_f=2.0\text{L/min}$, $P=2.5\ \text{psi}$, $C_s=0.12\%$

(b) $Q_f=2.0\text{L/min}$, $P=4.5\ \text{psi}$, $C_s=0.12\%$

4.3 Effect of Solid Concentration of Feed on Permeate Flux

Data collected from five experimental trials was used to determine the effect of the solid concentration of the feed on the permeate flux, as shown in Figure 4-10. The system was assumed to be at unsteady state for the first 100 seconds and the data was omitted. Similarly to the other variables previously discussed, over time, it was observed that the permeate flux decreased as the degree of fouling increased.

At lower solid concentrations, the permeate flux decline was more evident than at higher concentrations. Compared to the initial steady state flux, the feed at 0.21% showed a reduction of $0.002\ \text{m}^3/\text{m}^2\cdot\text{s}$ while the 0.04% feed concentration reduction was about $0.015\ \text{m}^3/\text{m}^2\cdot\text{s}$ after $800\ \text{s}$ of operation.

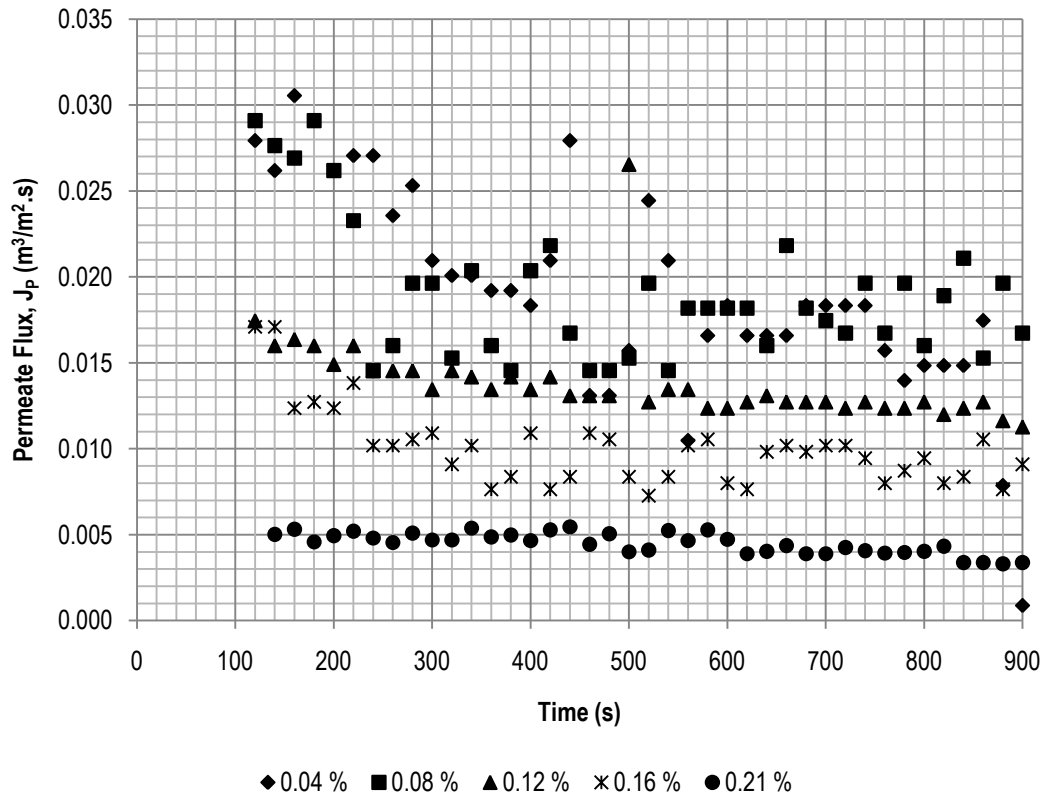


Figure 4-10: Permeate flux vs time for various Feed Solid concentrations, $Q_f=2.0\text{L/min}$, $P=3.5\text{psi}$

The steady-state permeate flux values for various feed solid concentrations were graphed in Figure 4-11. Included in the plot is the permeate flux achieved when clean water is used as the feed solution, achieving a value of $0.055 \text{ m}^3/\text{m}^2.\text{s}$. The plot shows the reduction in the steady-state permeate flux achieved after 800s of operation as the feed solid concentration increased. Compared to the clean water flux, increasing the feed solid concentration to 0.21% led to a reduction of the permeate flux to $0.004 \text{ m}^3/\text{m}^2.\text{s}$, a decline of 292%. This indicated that the membranes experienced a higher degree of flux decline when the feed solid concentration was increased, and may be explained by considering that at higher feed solid concentrations, there is a larger number of solid particles present in the feed that can contribute to the fouling of the membranes.

Plots of t/V vs V generated from the collected data for various feed solid concentrations can be found in Appendix B-3. The constants K_p and F_M were graphed against feed solid concentration in Figure 4-12 (a) and (b), respectively.

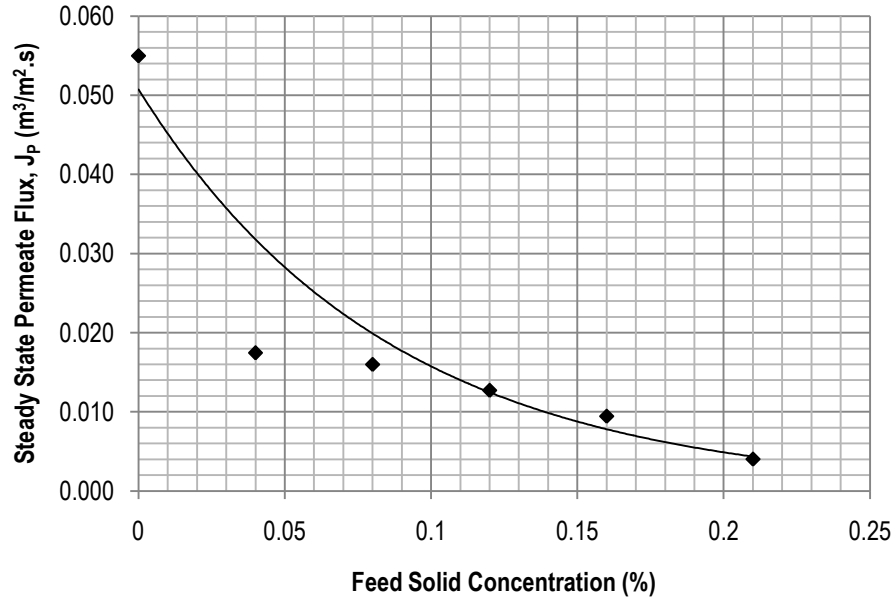


Figure 4-11: Steady-State Permeate Flux vs Feed Solid Concentration at $t=800$ s

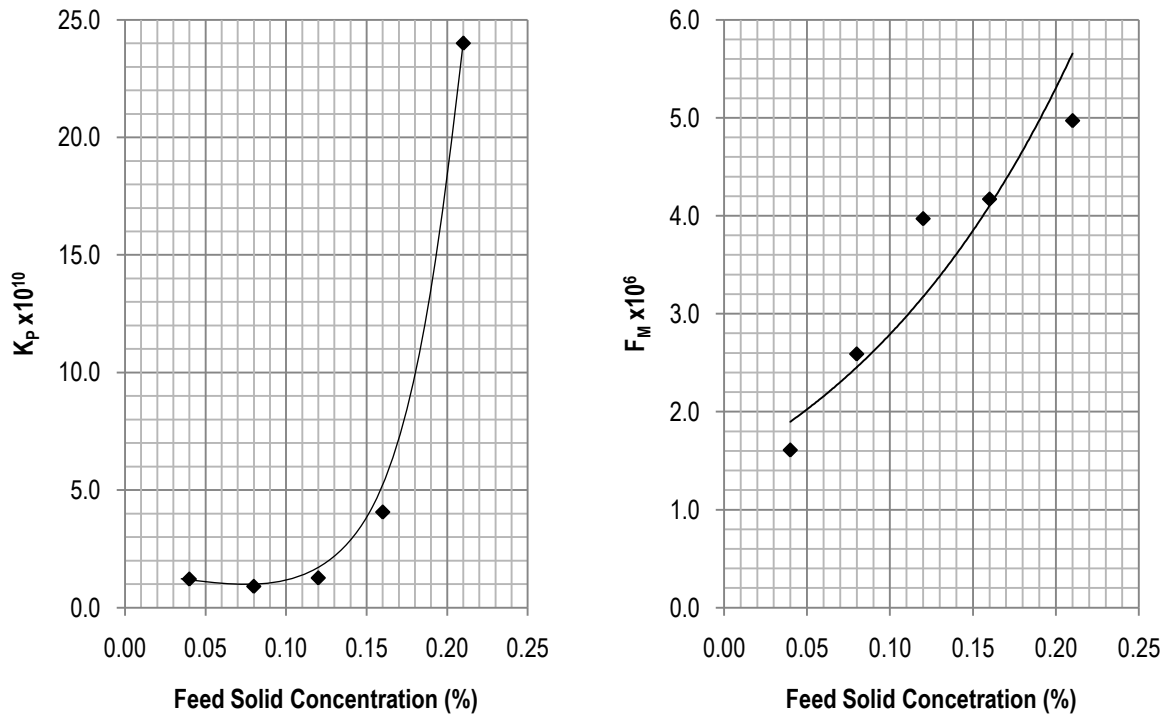


Figure 4-12: Filtration constants obtained from t/V vs. V graphs vs Feed Solid Concentration $Q_f=2.0\text{L}/\text{min}$, $P=3.5\text{psi}$.

With increasing feed solid concentration, K_p also increased, indicating that at higher feed solid concentrations, the resistance due to the cake accumulated increases. This was expected since at higher feed concentrations, the cake layer was expected to increase in thickness.

The constant F_M also increased with higher feed solid concentrations. This may be due to a higher number of particles that are smaller than the pore size of the membrane being present in the feed, leading to higher events of internal pore blocking. With an increase in the probability of these smaller particles adsorbed to the walls of the pores of the membrane, the resistance due to the membrane would appear to increase.

Increasing feed solid concentration also visible affected the cake layer. Low and high levels of feed solid concentration samples are shown in Figure 4-13(a) and (b), respectively. Here, it is clear that the thickness of the cake layer increased as the concentration was increased, from 1.4 μm to 4.6 μm to 5.9 μm from low to high concentration. With increased feed solid concentration, more particles are available to adhere to the particles previously deposited on the membrane surface.

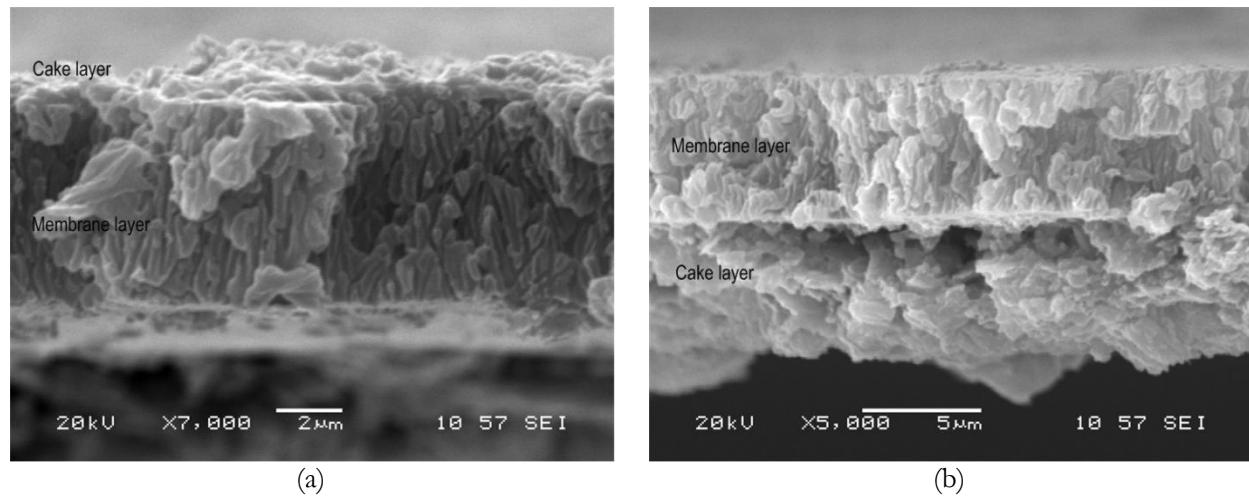


Figure 4-13: SEM images of sample of membrane after ultrafiltration ($t = 1200\text{s}$)

(a) $Q_f=2.0\text{L/min}$, $P=3.5\text{ psi.}$, $C_s=0.04\%$

(b) $Q_f=2.0\text{L/min}$, $P=3.5\text{ psi.}$, $C_s=0.21\%$

4.4 Pretreatment of Feed with Anionic Surfactant SDS

In the investigation of the effect of surfactant on the permeate flux, sodium dodecyl sulfate (SDS) was added to the feed at varying concentrations, below, at, and above the critical micelle concentration. In pure water, the CMC of SDS was reported to be 0.0082 M (Murkerjee and Mysels, 1971). This equates to about 2.36 g/L.

As shown in Figure 4-14, the steady-state permeate flux decreased as the SDS concentration was increased. When no SDS was added, a steady-state permeate flux of $0.0113\text{ m}^3/\text{m}^2\cdot\text{s}$ was achieved. When SDS was added at its CMC, this flux was reduced to $0.0054\text{ m}^3/\text{m}^2\cdot\text{s}$, a 52% reduction.

Therefore, it can be concluded that the addition of anionic surfactant to the feed reduced the effectiveness of the ultrafiltration process and was therefore not investigated further. It should be noted that the operating parameters for these experimental trials were a feed flow rate of 2.0 L/min, an operating pressure of 3.5 psi, and a paint solid concentration of 0.12%.

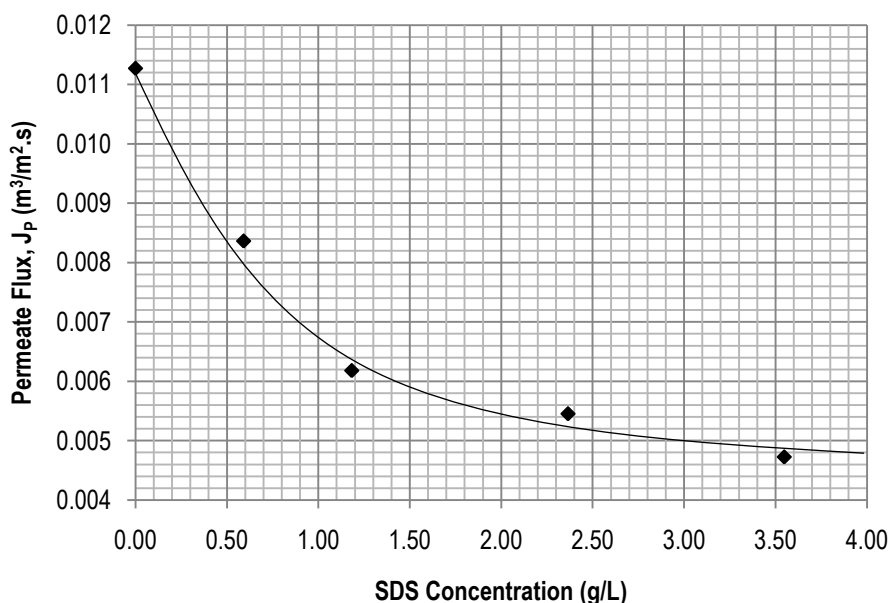


Figure 4-14: Steady-State Permeate Flux vs SDS surfactant concentrations at $t=800\text{s}$

4.5 Pretreatment of Feed with Cationic Surfactant CTAB

To investigate the addition of a cationic surfactant to the feed on the permeate flux, cetyl trimethylammonium bromide (CTAB) was added to the feed at concentrations above and below its reported CMC of 0.00092M (Murkerjee and Mysels, 1971) or about 0.33 g/L. It should be noted that the solid concentration of the feed before the addition of the surfactant was kept constant at 0.12% between experimental trials, and that the operating pressure and feed flow rate of 3.5 psi. and 2.0 L/min were used.

It is expected that the micelles formed would have the negatively-charged heads of the cationic surfactant molecules directed towards the outside, while the long-chain hydrophobic tails group together within the micelles core, as depicted in Figure 4-15. The latex paint solids are expected to dissolve within the micelles where the hydrophobic tails are clustered.

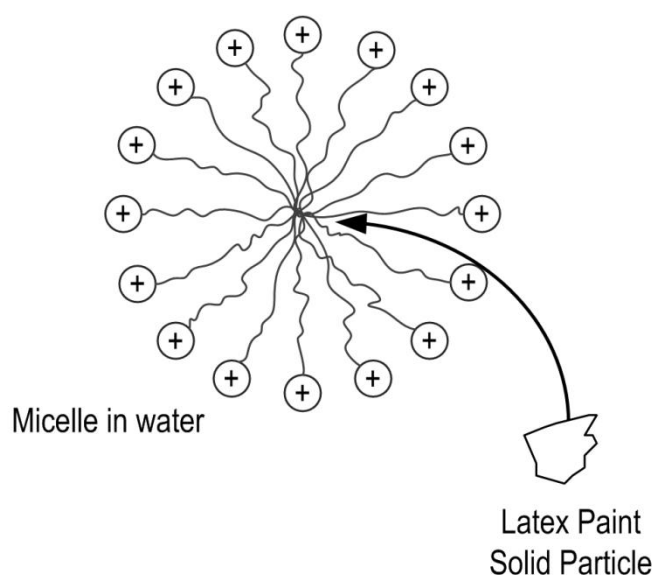


Figure 4-15: Representation of micelles formed using cationic surfactant

As shown in Figure 4-16, increasing the CTAB concentration resulted in higher permeate fluxes over time. Compared to the untreated feed, CTAB addition improved the ultrafiltration process. Even CTAB concentrations below the reported CMC displayed higher permeate flux. This CMC value was for surfactant solutions in pure water. With the addition of latex paint to the solution, the CMC may have shifted to a lower value, meaning that at lower CTAB concentrations, micelles may have been formed.

At higher CTAB concentrations, the permeate flux decline was greater than at lower concentrations. At 0.082 g/L CTAB concentration, the permeate flux drops from about $0.026 \text{ m}^3/\text{m}^2\text{s}$ to $0.013 \text{ m}^3/\text{m}^2\text{s}$, a decline of 50%. For a CTAB concentration of 0.492 g/L, there was a reduction of 64%, from $0.061 \text{ m}^3/\text{m}^2\text{s}$ to $0.022 \text{ m}^3/\text{m}^2\text{s}$.

The steady-state permeate flux achieved at various CTAB concentrations are shown in Figure 4-17. In general, as the CTAB concentration increases, this permeate flux also increases.

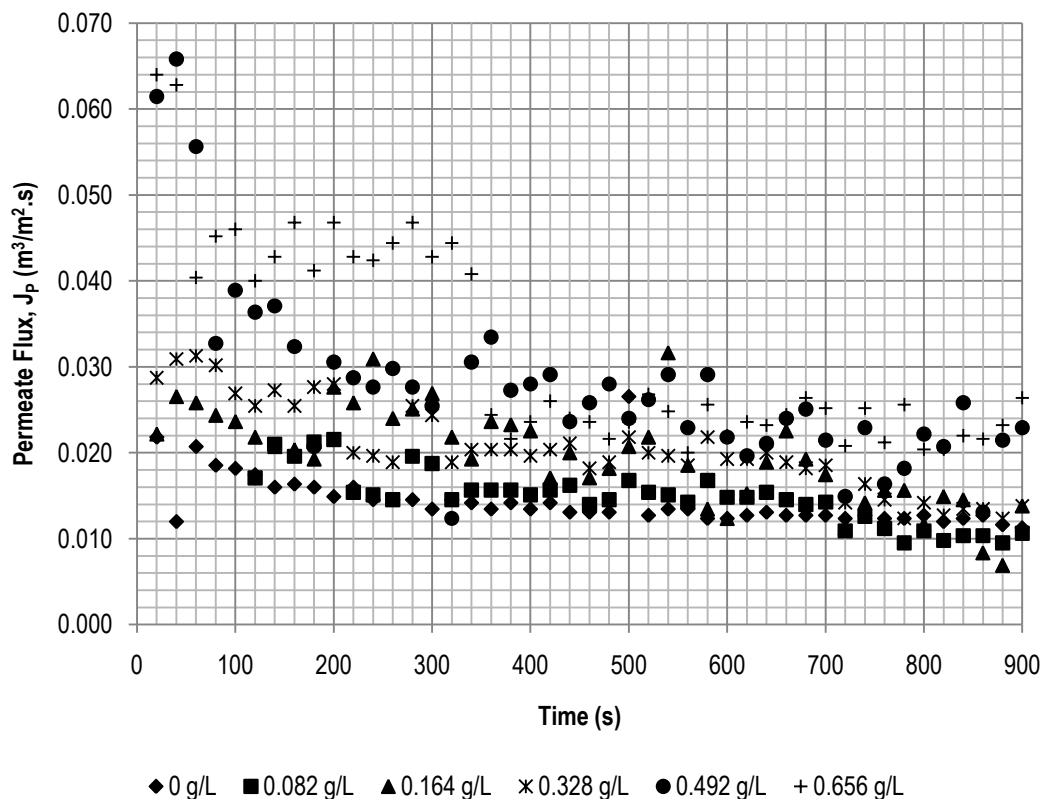


Figure 4-16: Permeate flux vs time for various CTAB concentrations, $P=3.5\text{psi.}$, $Q_f=2.0\text{L/min.}$, $C_s=0.12\%$ paint solids

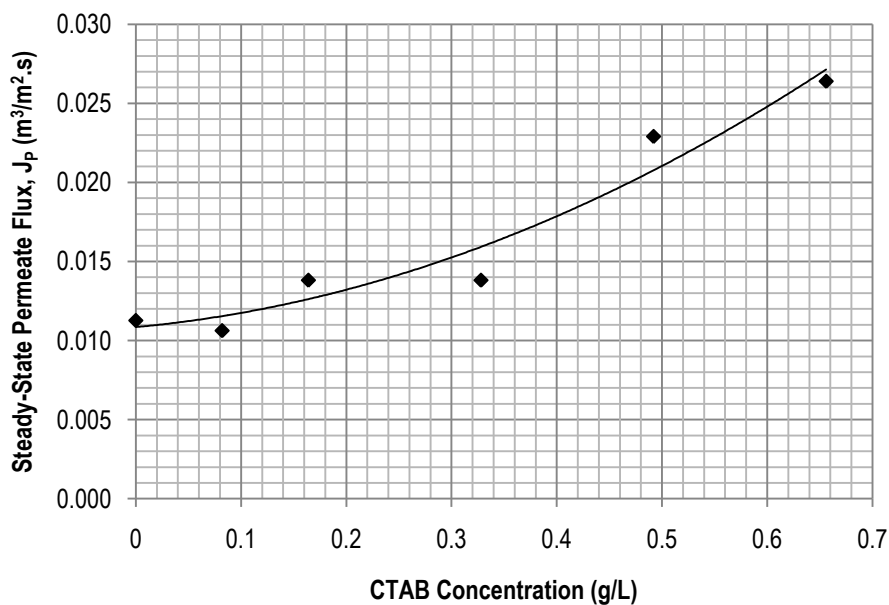


Figure 4-17: Steady-State Permeate Flux vs CTAB concentrations after $t=800\text{ s}$

The filtration constants K_p and F_M extracted from t/V vs V plots, found in Appendix B-4, are displayed in Figure 4-18 (a) and (b), respectively. The value of K_p generally decreases with increasing

CTAB concentration, indicating a decrease in the cake resistance. By increasing the CTAB concentration, the number of micelles may also increase. The larger size of the micelles compared to the original particles may result in a less dense cake layer, allowing more water molecules to pass freely into the permeate stream. Also, after the initial layer of micelles build onto the surface of the membranes, the similar surface charge of approaching micelles would cause a repulsion, essentially increasing the diffusion of particles away from the membrane surface. The constant F_M also decreases with increasing CTAB concentration, indicating a reduction in the membrane resistance.

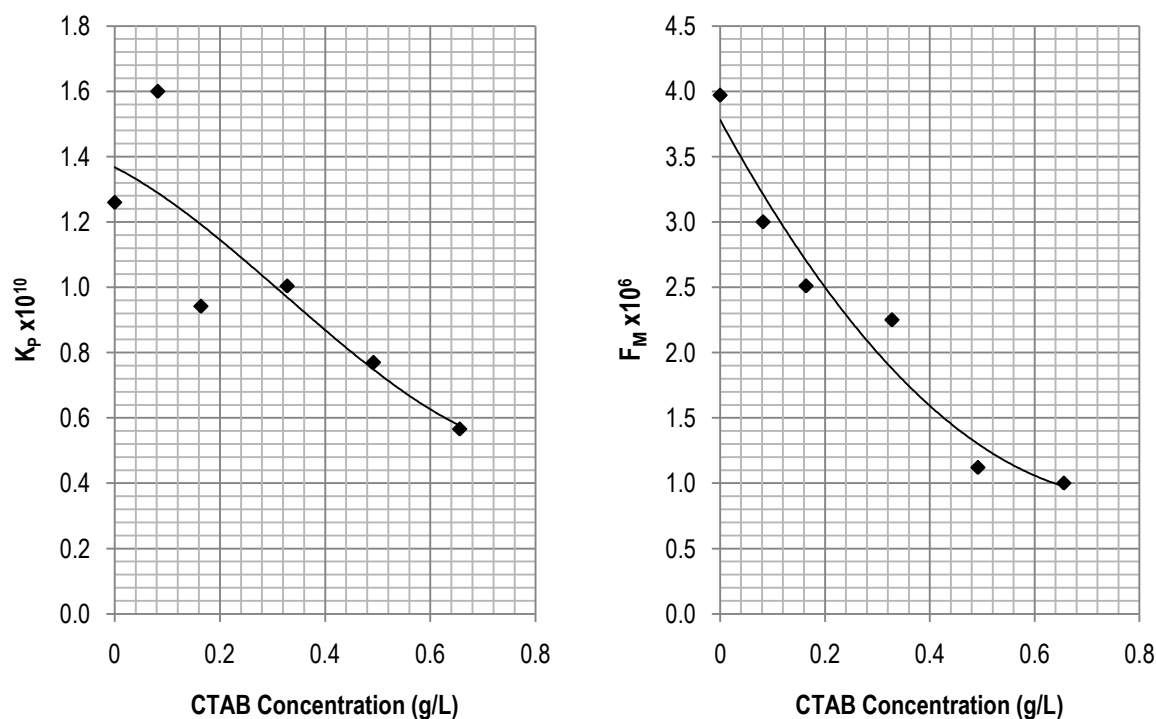


Figure 4-18: Filtration constants obtained from t/V vs. V graphs for various CTAB concentrations, $P=3.5\text{psi.}$, $Q_f=2.0\text{L/min}$, $C_s=0.12\%$ paint solids

Figure 4-19 illustrates the effect of cationic addition to the feed. While individual particles cannot be isolated in the image, it is clear that the cake layer formed has a significantly lower density when compared to the sample without the surfactant. The thickness of the layer is also thinner, at about $3.4\text{ }\mu\text{m}$. This may be due to the increased repulsion of incoming particles after the initial layer has been formed because of the like charges on the surface of the particles.

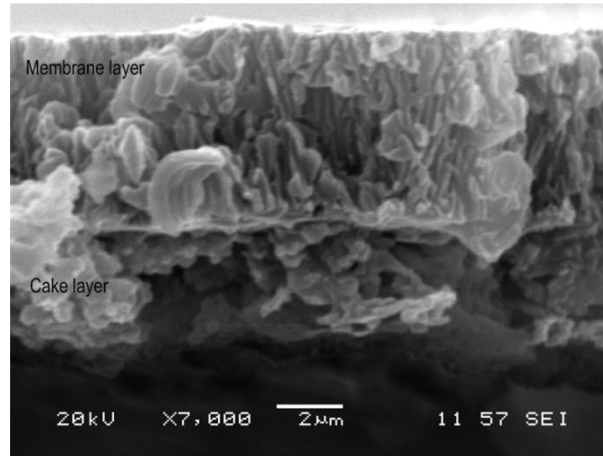


Figure 4-19: SEM images of sample of membrane after ultrafiltration with CTAB addition to the feed solution, $Q_f=2.0$ L/min, $P=3.5$ psi., $C_s=0.12\%$, $CTAB=0.492$ g/L ($t = 1200$ s)

4.6 Determining the Mass Transfer Coefficient at Membrane Surface

In order to determine the mass transfer coefficient in the membrane filtration cell, an experimental trial was conducted where the retentate stream was recycled back to the feed tank. This would allow the concentration of the feed solution to increase over time since some of the clean water was removed in the permeate stream. The decline of permeate flux over time was depicted in Figure 4-20.

Following the mathematical relationships to determine the mass transfer coefficient as previously discussed (Equation (7)), the permeate flux was plotted against the natural logarithm of the concentration factor, as shown in Figure 4-21. From this graph, the slope equates to the mass transfer coefficients and is found to be $7.99 \times 10^{-7} \text{ m.s}^{-1}$. The mass transfer coefficient, together with Equation (5) and Equation (7), can be used to predict the permeate flux in the presence of the concentration polarization (equilibrium layer of gel on the membrane) for a continuous ultrafiltration and a batch operation, respectively. The intercept was used to determine the gel layer concentration at 0.42%. This is significantly higher than the concentration of the bulk, which is equal to the concentration of the initial feed concentration of 0.12%.

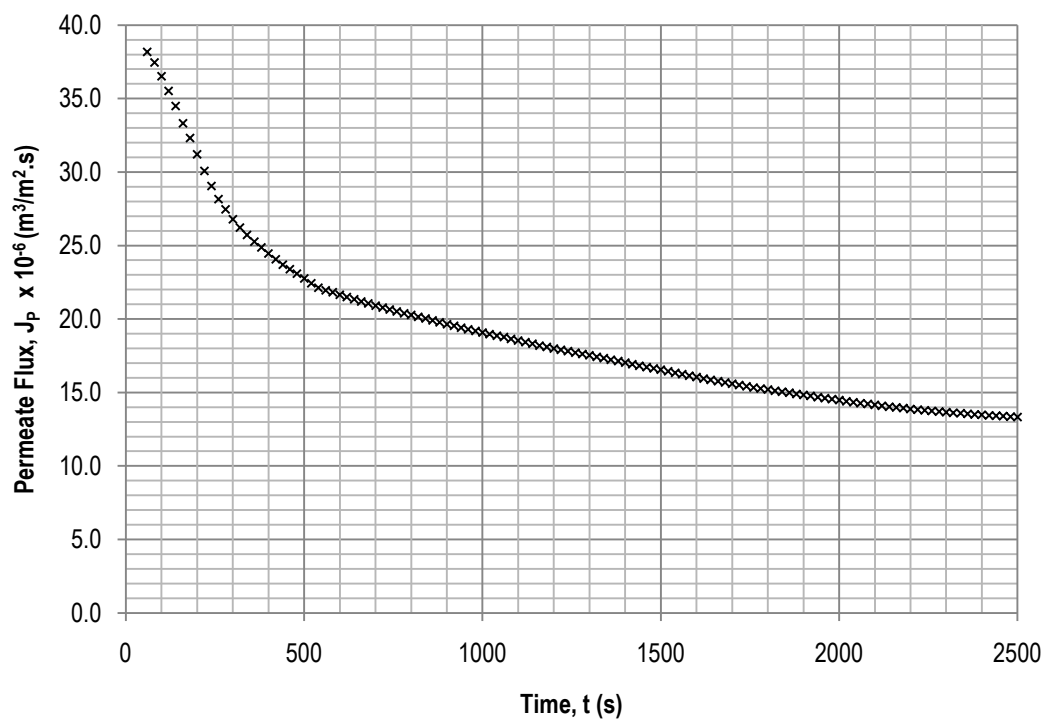


Figure 4-20: Permeate Flux vs time with recycle of retentate stream to the feed tank
 $P=3.5\text{psi}$, $Q_r=2.0\text{L/min}$, $C_s=0.12\%$

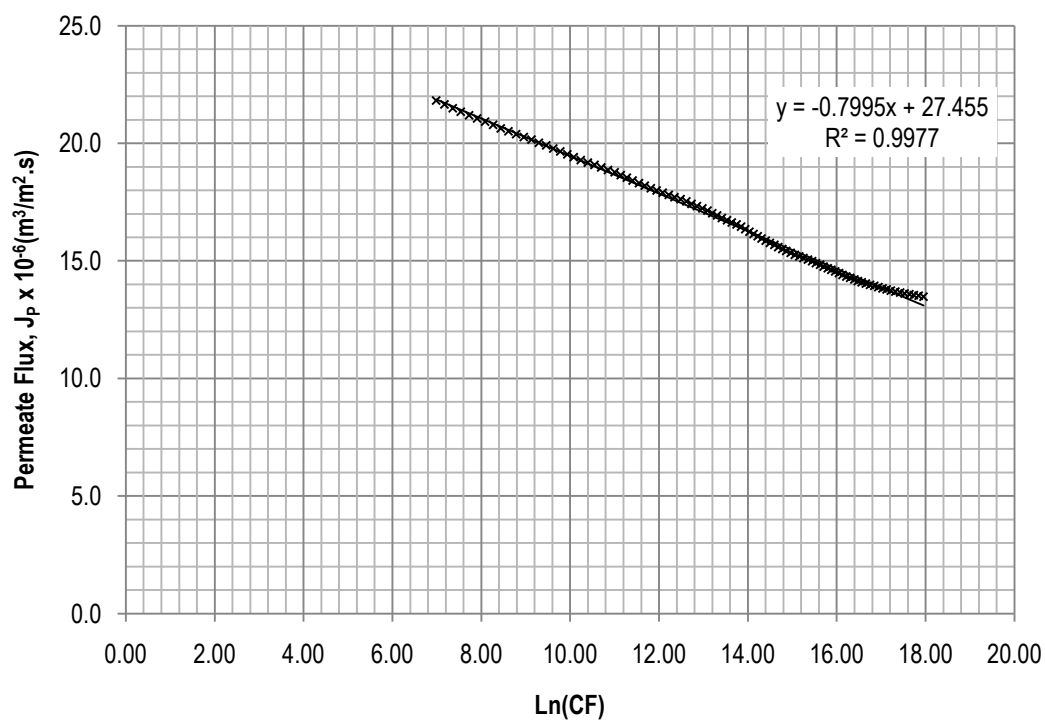


Figure 4-21: Permeate Flux vs $\text{Ln}(\text{CF})$

4.7 Empirical Models for Filtration

In this section, Hermia's models as previously described were used to interpret the fouling phenomena experienced during the separation process. This involves using Equation (9) with values for the parameters dependent on the model under consideration.

4.7.1 Complete Blocking Model

The complete blocking model assumes that all particles reaching the membrane surface from the bulk has a particle size greater than the size of the pores of the membrane (Vela et al., 2008), and that the particles are not superimposed on the other (Hermia, 1982). This results in pore sealing, as depicted in Figure 2-4(a). Here, the parameter n is equal to 2. By substituting this into Equation (9) and linearizing, the expression for the complete blocking model is derived (see Table 2-2). It can be seen that the slope of the plot of $\ln(J_p)$ versus time is equal to the complete pore blocking model constant K_b , while the intercept is equal to the initial permeate flux.

Figure 4-22 displays the prediction of the permeate flux based on the complete blocking model compared to the experimental data collected previously for various feed flow rates. The change in time between the experimental data points is approximately every 60s. The time domain considered was $t < 600$ s since above this time, the permeate flux versus time plot, Figure 4-1, generally levelled off to a constant value, indicating that cake filtration was dominant. The aim of this analysis is to determine the effect of the pore blocking on the fouling, which occurs during the initial time of the filtration run. From Figure 4-22, the complete blocking model shows a fairly good fit to the data for all feed flow rates considered.

The relative value of the complete pore blocking model constant is an indication of degree of fouling experienced; the higher the value of K_b , the more severe the fouling of the membrane (Vela et al., 2008). This is due to the physical meaning and definition of the parameter. Here, K_b is equal to the filtrate linear velocity, u_0 , multiplied by the blocked area per unit of filtrate volume, σ . At higher feed flow rates, u_0 generally increases, resulting in higher values for the constant K_b , as shown in Figure 4-22. This result is similar to that described previously where the change in the initial flux was greater for higher feed flow rates than for lower ones.

From the plot shown in Figure 4-22, the initial permeate flux, J_0 , can also be obtained from the intercept of the model. Shown in Table 4-1 are the values obtained from the model as well as the measured initial permeate flux. For 1.5 L/min feed flow rate, the calculated initial permeate flux was

0.011 m³/m².s, while the measured value was 0.014 m³/m².s, showing a discrepancy of 19%. For higher feed flow rates, the error between the calculated and measure values of the initial permeate flux decreased from 19% for 1.5 L/min., to 11% for 3.0 L/min.

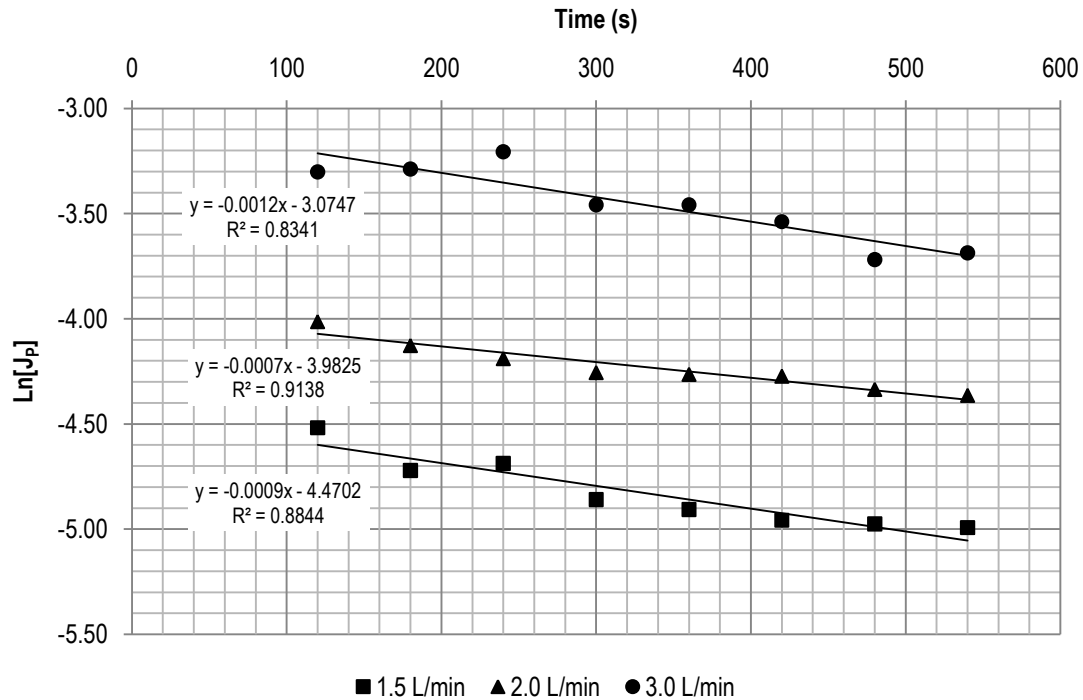


Figure 4-22: Permeate flux predicted by the complete blocking model for various feed flow rates
P=3.5psi., Cs=0.12%

Table 4-1: Comparison between experimental initial permeate flux and the initial permeate flux obtained from the complete blocking model

Variable	Value	K_b	J_0 (Model) (m ³ /m ² s)	J_0 (Measured) (m ³ /m ² s)	% Error
Flowrate (L/min) (P=3.5 psi, Cs=0.12%)	1.5	0.0009	0.011	0.014	19%
	2.0	0.0007	0.019	0.022	15%
	3.0	0.0012	0.046	0.052	11%
Pressure (psi) (Q _f =2.0L/min, Cs=0.12%)	2.5	0.0012	0.015	0.016	3%
	3.5	0.0007	0.019	0.022	15%
	4.5	0.0010	0.030	0.029	5%
Feed Solid Concentration (%) (Q _f =2.0L/min, P=3.5 psi)	0.04	0.0015	0.040	0.043	6%
	0.12	0.0007	0.019	0.022	15%
	0.16	0.0016	0.018	0.017	10%
CTAB concentration (g/L) (Q _f =2.0L/min, P=3.5 psi, Cs=0.12% paint solids)	0.000	0.0007	0.019	0.022	15%
	0.082	0.0006	0.021	0.024	14%
	0.328	0.0008	0.029	0.031	5%
	0.656	0.0006	0.035	0.040	13%

A similar approach was taken to investigate the complete blocking model of various transmembrane pressures, as displayed in Figure 4-23. The model did not agree as well for 2.5 psi compared to the 3.5 psi. and 4.5 psi. runs. When comparing the slopes of the model obtained for the 3.5 psi to the 4.5 psi trial, the slope increases. This indicates that as the transmembrane pressure is increased, the degree of fouling also increased, as shown by an increase in the value of K_b , from $0.0007s^{-1}$ for 3.5 psi, to $0.001s^{-1}$ for 4.5 psi. The value of the predicted initial permeate flux compared to that obtained experimentally were very similar, showing differences below 15%, as displayed in Table 4-1.

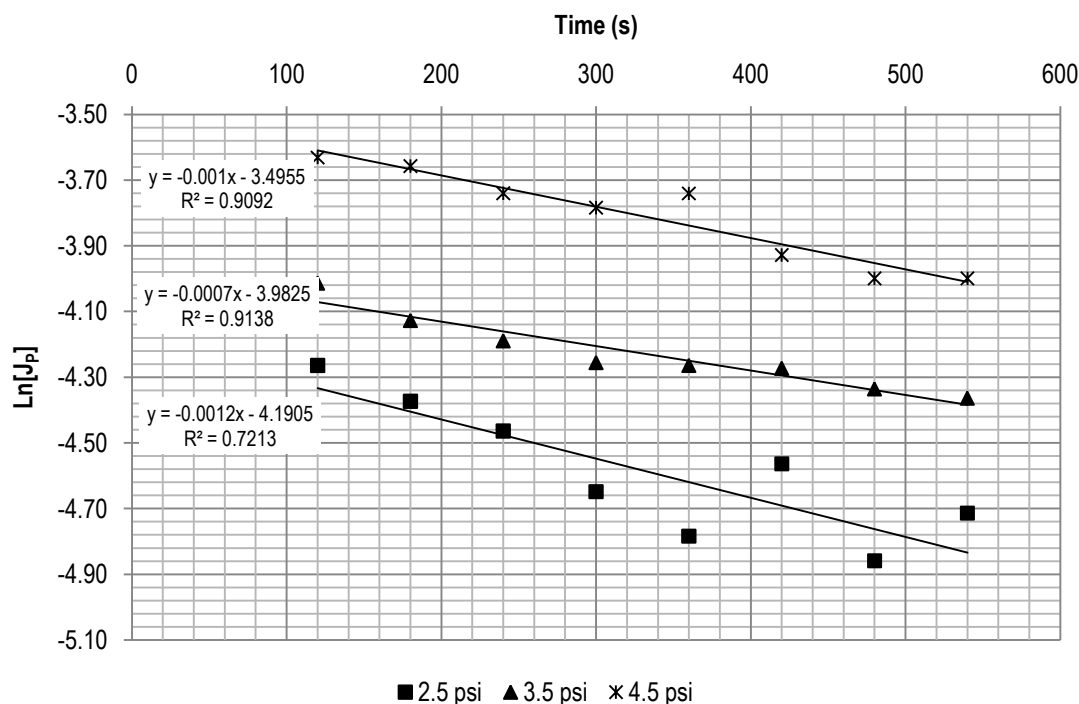


Figure 4-23: Permeate flux predicted by the complete blocking model for various operating pressures $Q_f=2.0L/min$, $C_s=0.12\%$

As displayed in Figure 4-24, the permeate flux was predicted for various feed solid concentrations. It was found that increasing the feed solid concentration from 0.12% to 0.16% resulted in K_b increasing from $0.0007s^{-1}$ to $0.0015s^{-1}$, confirming that the degree of fouling increases as the feed solid concentration is increased. At low feed solid concentration, the model did not fit the data as accurately when compared to the higher feed solid concentrations, with an R^2 value of 0.721 compared to larger than 0.9. The model accurately predicted the initial permeate flux, with a difference of less than 15%.

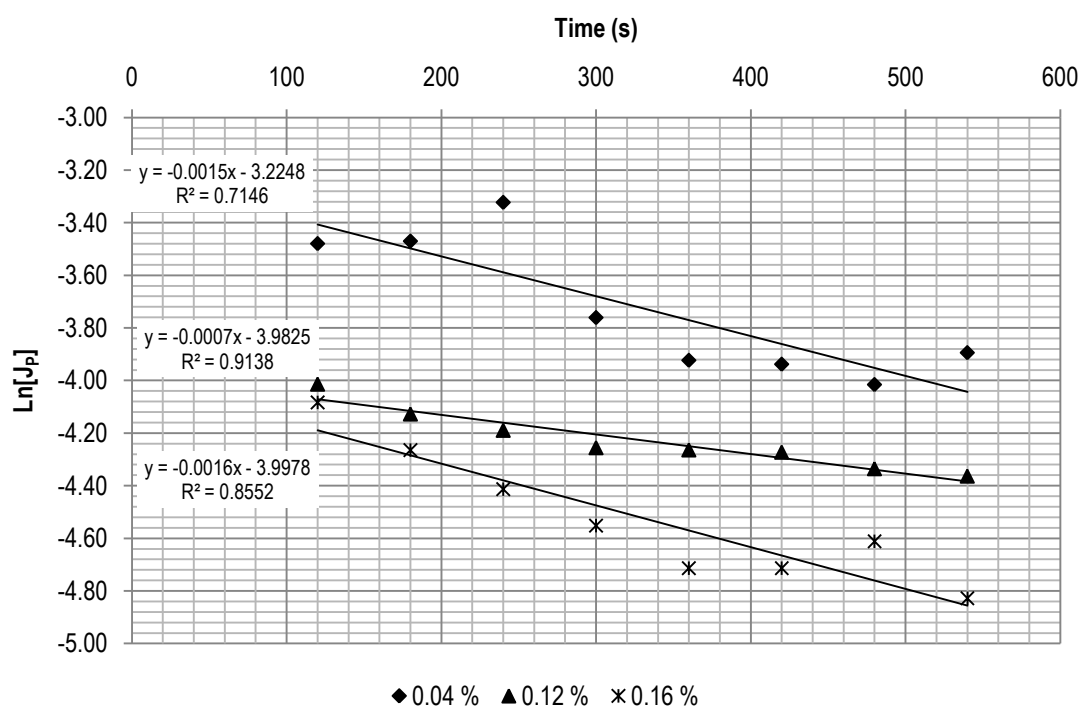


Figure 4-24: Permeate flux predicted by the complete blocking model for various feed solid concentrations, $Q_f=2.0\text{L/min}$, $P=3.5\text{ psi}$.

The complete blocking model was also applied for experimental data collected using various concentrations of the cationic surfactant CTAB as shown in Figure 4-25. The plot shows that increasing the CTAB concentration did not affect the value of K_b , and therefore, conclusions based on the degree of fouling using this model cannot be made. However, the model was able to accurately predict the initial permeate flux at various CTAB concentrations, shown in Table 4-1. Compared to the measured values, the discrepancy to the calculated values was between 5% and 15%.

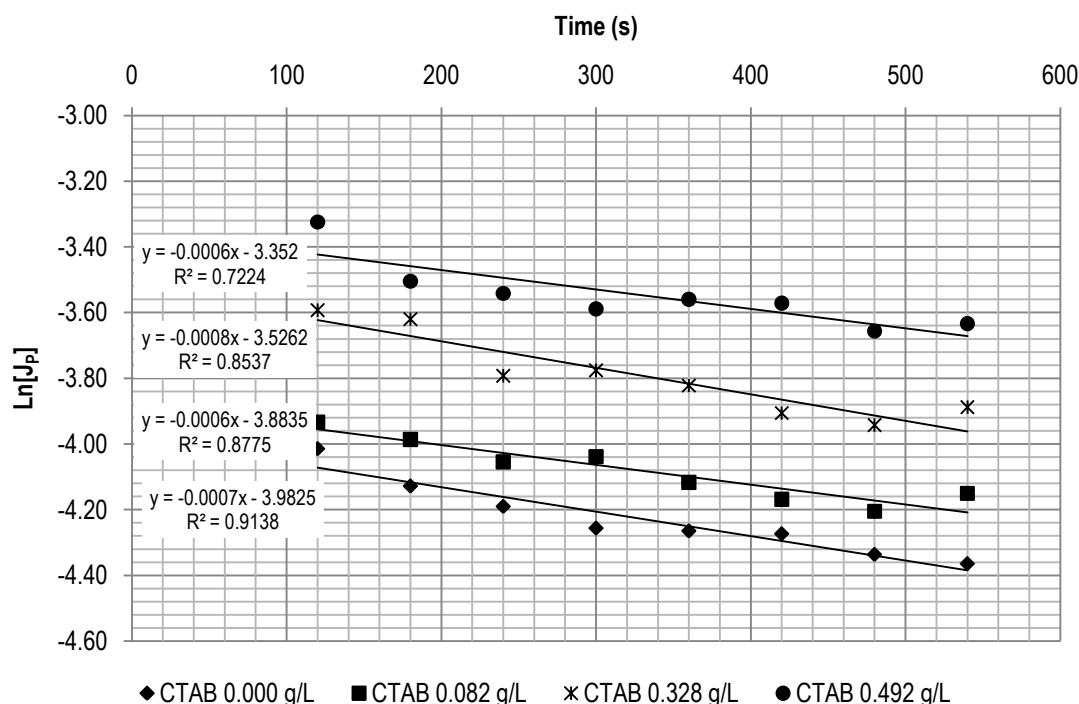


Figure 4-25: Permeate flux predicted by the complete blocking model for various concentrations of CTAB, $P=3.5\text{psi}$, $Q_f=2.0\text{L/min}$, $C_s=0.12\%$ paint solids

4.7.2 Intermediate Blocking Model

Similar to the complete blocking model previously discussed, the intermediate blocking model considers that solid particle reaching an open pore will seal the pore, as illustrated in Figure 2-4(b). However, in this model, particles approaching the sealed pore may accumulate on other particles. In this way, if the particle attaches to the side of a pore opening, accumulated particles above it may lead to the pore being fully sealed (Hermia, 1982).

With this model, the parameter n in Equation (9) is equal to 1, and after linearizing, in terms of flux, the equation displayed in Table 2-2 is achieved. This allows for plots of J_p^{-1} versus time to be used to determine the intermediate pore blocking model constant, K_i , as the slope, as well as an estimation of the initial permeate flux, J_0 , as the intercept.

The constant K_i is defined as the ratio of the blocked area per unit of filtrate volume to the total area of the membrane. Therefore, since the total area of the membrane was kept constant between the experimental trials, an increase in the value obtained for K_i would indicate an increase in the blocked area, and may be interpreted as an increase in the degree of fouling of the membrane.

Figure 4-26 displays the predicted permeate flux values for various feed flow rates. The model achieved a high level of agreement for the flow rates of 1.5, 2.0, and 3.0 L/min. Here, it is shown that increasing the feed flow rate from 1.5 L/min to 3.0 L/min led to a decrease in the value of K_i from 0.1308m^{-3} to 0.0378m^{-3} , indicating a reduction in the degree of fouling of the membrane at higher feed flow rates. This decrease may be due to the model assuming the build up of approaching particles on other particles that have already attached to the membrane surface. At higher feed flow rates, the larger amount of fluid travelling parallel to the membrane surface per unit time increases the occurrence of particle wash-out, which will reduce the number of particles that accumulate on other particles, resulting in an overall reduction in the blocked area of the membrane. This may have caused lower values for K_i .

Initial permeate flux predictions using the intermediate blocking model for various flow rates are compared in Table 4-2. The model showed good approximations, with differences ranging from 3% for 3.0 L/min to 13% for 2.0 L/min.

When the transmembrane pressure is increased, it was found that the value of K_i generally decreased, as shown in Figure 4-27. At 2.5 psi, the value of K_i was 0.1137m^{-3} , compared to 0.0438m^{-3} at 4.5 psi., indicating a reduction in the degree of fouling at higher transmembrane pressures. This may be explained due to the compacting of the accumulated particles on the membrane surface at higher operating pressures, which may reduce the effective particle size of the agglomeration. These smaller sized particles may penetrate through the membrane pores into the permeate stream. This decrease in K_i is opposite to the effect found for the complete blocking model constant, K_b .

The predicted values for the initial permeate flux, as shown in Table 4-2, are close to the measured values. The model also showed a higher level of accuracy at predicting this parameter when compared to the complete blocking model, showing discrepancies up to 13%, as opposed to below 15% for the complete blocking model.

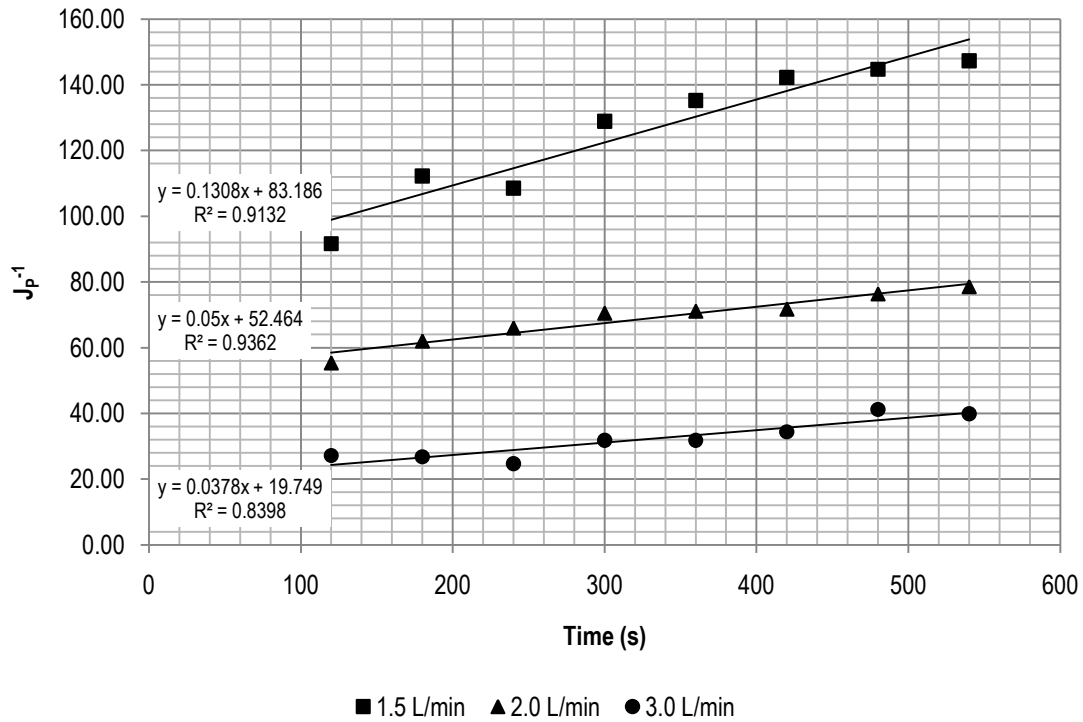


Figure 4-26: Permeate flux predicted by the intermediate blocking model for various feed flow rates
 $P=3.5$ psi., $C_s=0.12\%$

Table 4-2: Comparison between experimental initial permeate flux and the initial permeate flux obtained from the intermediate blocking model

Variable	Value	K_i	J_0 (Model) ($\text{m}^3/\text{m}^2\text{s}$)	J_0 (Measured) ($\text{m}^3/\text{m}^2\text{s}$)	% Error
Flowrate (L/min) ($P=3.5$ psi, $C_s=0.12\%$)	1.5	0.1308	0.014	0.016	11%
	2.0	0.0500	0.019	0.022	13%
	3.0	0.0378	0.051	0.052	3%
Pressure (psi) ($Q_f=2.0\text{L/min}$, $C_s=0.12\%$)	2.5	0.1137	0.016	0.016	3%
	3.5	0.0500	0.019	0.022	13%
	4.5	0.0438	0.032	0.029	11%
Feed Solid Concentration (%) ($Q_f=2.0\text{L/min}$, $P=3.5$ psi)	0.04	0.0618	0.045	0.043	6%
	0.12	0.0500	0.019	0.022	13%
	0.16	0.1410	0.021	0.017	25%
CTAB concentration (g/L) ($Q_f=2.0\text{L/min}$, $P=3.5$ psi, $C_s=0.12\%$ paint solids)	0.000	0.0500	0.019	0.022	13%
	0.082	0.0353	0.021	0.024	13%
	0.328	0.0350	0.030	0.031	2%
	0.656	0.0198	0.035	0.040	13%

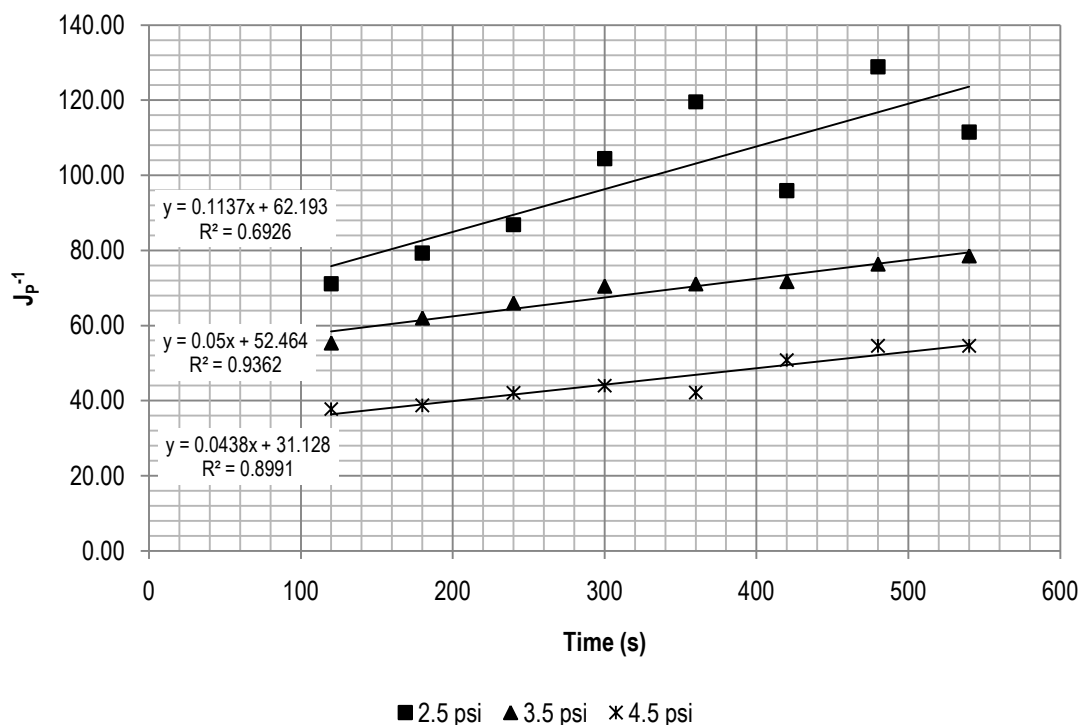


Figure 4-27: Permeate flux predicted by the intermediate blocking model for various operating pressures $Q_f=2.0\text{L/min}$, $C_s=0.12\%$

For increasing feed solid concentrations, the value of K_i increased, as shown in Figure 4-28. This matches the trend of the complete blocking model, and indicates that at higher feed solid concentration, the degree of fouling of the membrane is higher. This may be explained by, similarly to the complete blocking model, at higher feed solid concentrations, there are a larger number of particles available for deposition on the membrane surface indicated by the intermediate pore blocking model. Table 4-2 also compares the predicted and measured initial permeate fluxes for various feed solid concentrations, showing a high discrepancy between them, ranging from 6% to 25% difference.

Figure 4-29 displays the predicted permeate flux for various concentrations of CTAB. The value of K_i decreases as the CTAB concentration is increased. It decreases from 0.050m^{-3} to 0.020m^{-3} between 0.00g/L to 0.656g/L . This is expected since the previous discussion on the effect of CTAB addition on the permeate flux indicated a similar trend, where increased CTAB concentration decreased the degree of fouling of the membrane, leading to higher permeate fluxes (see Section 4.5). This was due to the formation of the particle micelles leading to less particles smaller than the membrane pore size, and therefore, less occurrences of intermediate blocking.

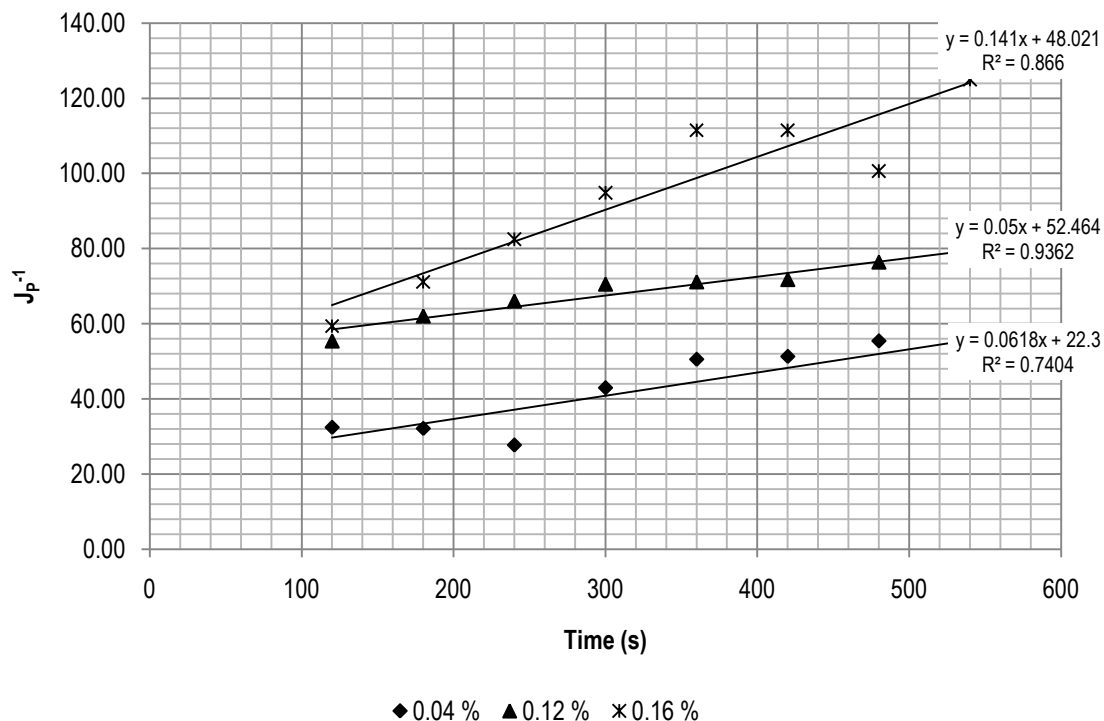


Figure 4-28: Permeate flux predicted by the intermediate blocking model for various feed solid concentrations, $Q_f=2.0\text{L/min}$, $P=3.5\text{psi}$.

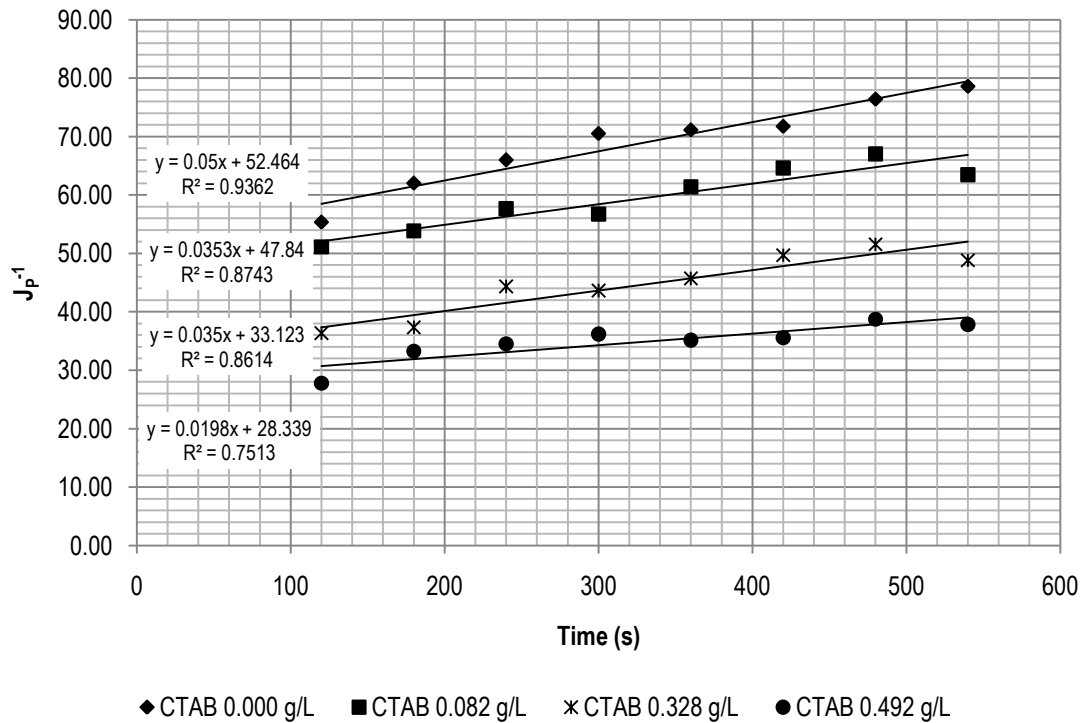


Figure 4-29: Permeate flux predicted by the intermediate blocking model for various concentrations of CTAB, $P=3.5\text{psi}$, $Q_f=2.0\text{L/min}$, $C_s=0.12\%$ paint solids

4.7.3 Standard Blocking Model

The standard blocking model assumes that particles deposit within the pores, attaching to the walls of the pores, as shown in Figure 2-4(c). This model also assumes that each pore is cylindrical, with a constant length and diameter (Hermia, 1982) and that the pore volume decreases proportionally to the filtrate volume. In Equation (9), this model adopts a value of n equal to $3/2$. After linearizing and in terms of the permeate flux, the equation listed in Table 2-2 is obtained. Plots of $J_p^{-0.5}$ versus time allows the determination of the standard pore blocking constant, K_s , an similar to the other models previously discussed, it is able to approximate a value for the initial permeate flux.

The constant K_s incorporates C , the volume of solid particles retained per unit filtrate volume, as well as the length of the pores, the membrane area, and the feed flow rate. Therefore, as with the other models, as K_s increases, it may be used as an indication that the degree of fouling of the membrane also increases. This is because while the other parameters are kept constant, the volume of solid particles retained by the membrane also increases.

Shown in Figure 4-30 are the predicted permeate flux using the standard blocking model for various feed flow rates. The model is in good agreement with the experimental data of all the flow rates investigated. The value of K_s generally decreases as the feed flow rate is increased, indicating a reduction in the degree of fouling of the membrane. This trend is similar to that of the intermediate pore blocking constant, K_i . At higher feed flow rates, the particles smaller than the pore size that cause standard blocking to occur may be washed out into the retentate more than at lower feed flow rates. Therefore, the standard blocking model would show a decline in the degree of fouling of the membrane, even though the membrane is fouled faster at higher feed flow rates.

In Table 4-3, measured values for the initial permeate flux is compared to the predicted initial permeate flux using the standard blocking model. The model predicts the initial permeate flux well for various feed flow rates, showing differences up to 14%.

Figure 4-31 displays the standard blocking model predictions for various transmembrane pressures. The model does not accurately represent the data collected for an operating pressure of 2.5 psi ($R^2=0.708$). However, at higher transmembrane pressures, the coefficient of determination (R^2) is above 0.9, indicating a high level of agreement to the model. When increasing the transmembrane pressure from 3.5 psi to 4.5 psi, the value of K_s increases from $0.003s^{-2}$ to $0.0036s^{-2}$. This shows that the degree of membrane fouling due to standard pore blocking increases at higher transmembrane

pressures. This is expected since at higher transmembrane pressures, the particles may penetrate into the membrane pores more frequently, and may adhere to the wall surfaces. There may also be higher deformation of the particles, leading to an overall reduction of any agglomerations of the solid particles to particles sizes smaller than the pore size of the membrane. The predicted values for the initial permeate flux were close to the measured values, showing a deviation of less than 14% for all transmembrane pressures investigated.

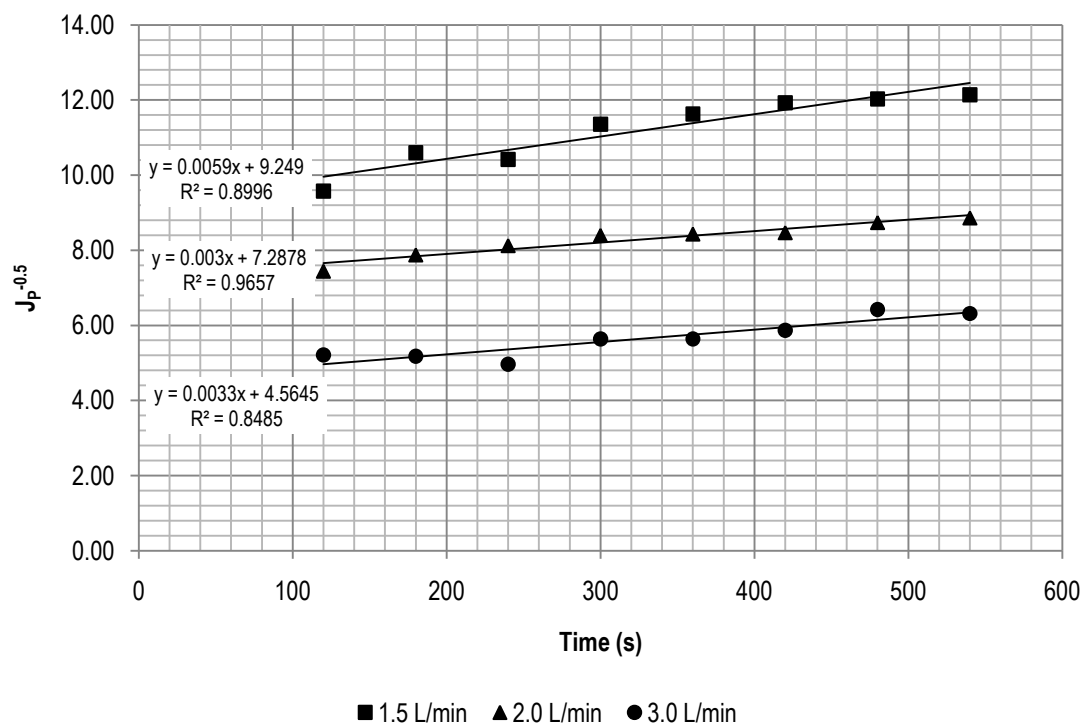


**Figure 4-30: Permeate flux predicted by the standard blocking model for various feed flow rates
P=3.5psi., Cs=0.12%**

For increasing feed solid concentration, there is an increase in the value of the constant K_s , as shown in Figure 4-32, which indicates an increase in the degree of fouling of the membrane. At higher feed solid concentrations, there are a larger number of solid particles available that participate in the fouling of the membrane, and therefore, the degree of fouling should be larger.

The predictions for the initial permeate flux were very similar to that of the measured values for lower concentrations, with a discrepancy of less than 2%. However, at the higher concentration, 0.16%, there was an error of 15%. This may be due to the fact that the model only accounts for particles smaller than the pore size of the membrane. Particles larger than the pore size, which are

present in even higher numbers at higher feed solid concentrations, are not represented by the model.

Table 4-3: Comparison between experimental initial permeate flux and the initial permeate flux obtained from the standard blocking model

Variable	Value	K_s	J_0 (Model) ($\text{m}^3/\text{m}^2\text{s}$)	J_0 (Measured) ($\text{m}^3/\text{m}^2\text{s}$)	% Error
Flowrate (L/min) ($P=3.5$ psi, $C_s=0.12\%$)	1.5	0.0059	0.014	0.016	11%
	2.0	0.0030	0.019	0.022	14%
	3.0	0.0033	0.048	0.052	8%
Pressure (psi) ($Q_f=2.0\text{L/min}$, $C_s=0.12\%$)	2.5	0.0058	0.016	0.016	0%
	3.5	0.0030	0.019	0.022	14%
	4.5	0.0036	0.031	0.029	7%
Feed Solid Concentration (%) ($Q_f=2.0\text{L/min}$, $P=3.5$ psi)	0.04	0.0048	0.042	0.043	2%
	0.12	0.0030	0.019	0.022	14%
	0.16	0.0075	0.019	0.017	15%
CTAB concentration (g/L) ($Q_f=2.0\text{L/min}$, $P=3.5$ psi, $C_s=0.12\%$ paint solids)	0.000	0.0030	0.019	0.022	14%
	0.082	0.0023	0.021	0.024	14%
	0.328	0.0027	0.030	0.031	4%
	0.656	0.0017	0.035	0.040	13%

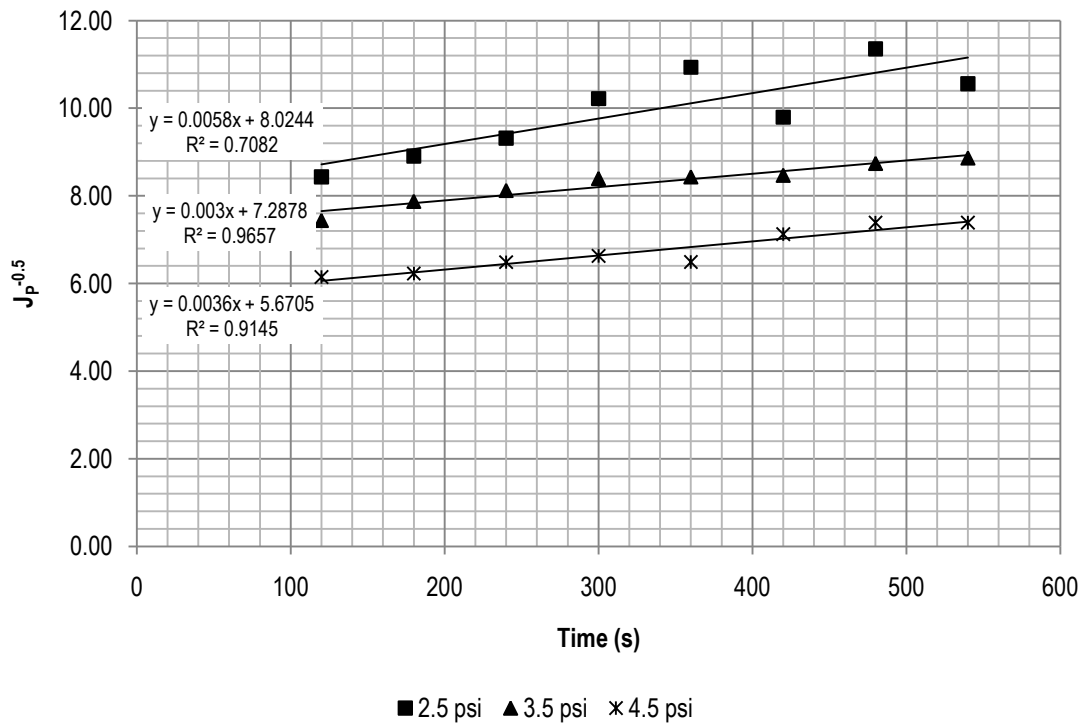


Figure 4-31: Permeate flux predicted by the standard blocking model for various transmembrane pressures $Q_f=2.0\text{L/min}$, $C_s=0.12\%$

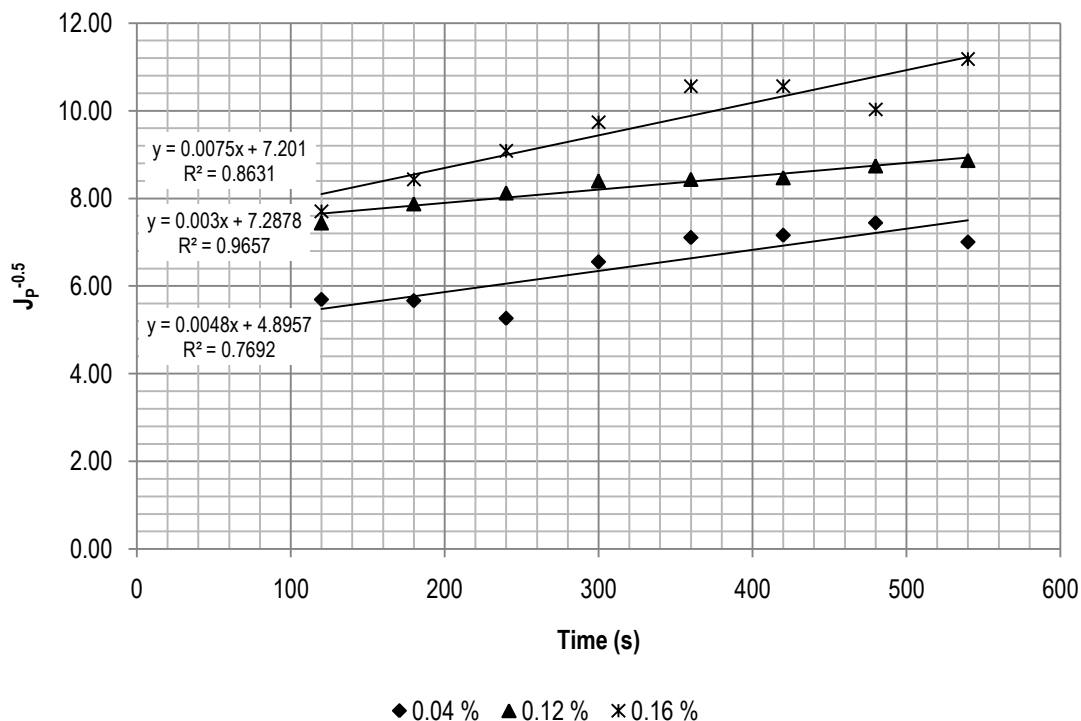


Figure 4-32: Permeate flux predicted by the standard blocking model for various feed solid concentrations, $Q_f=2.0\text{L/min}$, $P=3.5\text{psi}$.

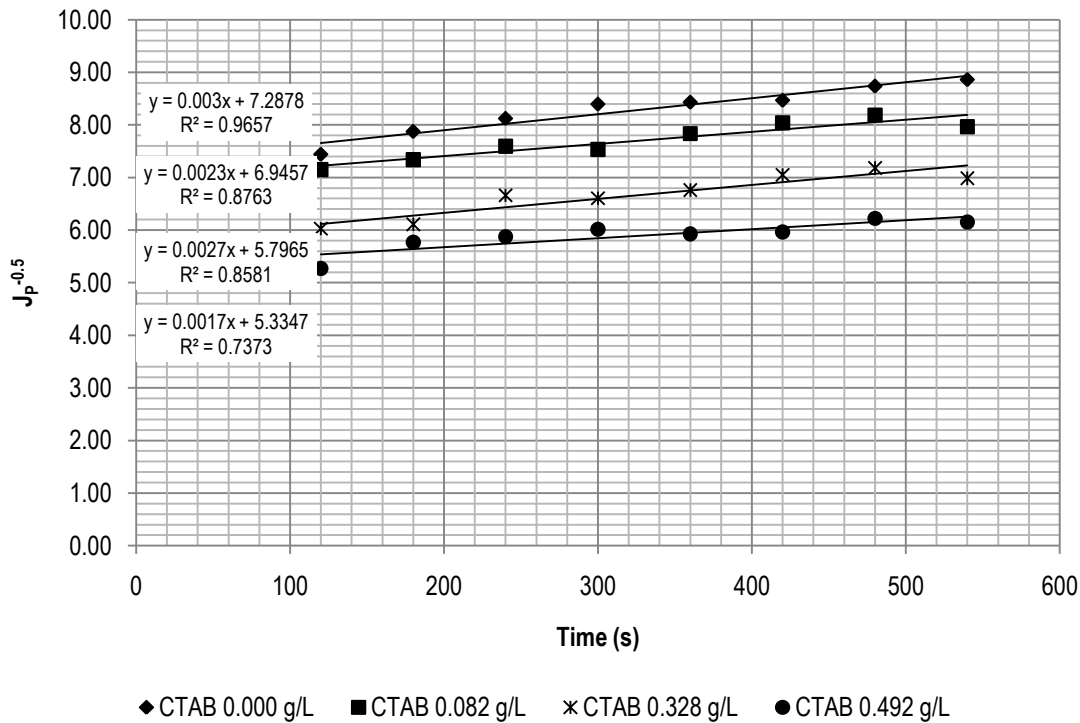


Figure 4-33: Permeate flux predicted by the standard blocking model for various concentrations of CTAB, $P=3.5\text{psi}$, $Q_f=2.0\text{L/min}$, $C_s=0.12\%$ paint solids

The standard blocking model performed well for various CTAB concentrations as displayed in Figure 4-33. From this plot, it is shown that the value of the constant K_s generally decreased with increased CTAB concentration. At higher CTAB concentrations, there will be a larger number of micelles formed, which would have a particle size greater than the pore size of the membrane. Therefore, there may be lower occurrences of standard pore blocking, leading to a decrease in the value of K_s . The initial permeate flux predicted by the standard blocking model showed an accuracy of about 14% for most trials.

4.7.4 Cake Layer Formation Model

The cake layer formation model considers solid particles above the membrane pore size that do not penetrate inside the pores but deposit on the membrane surface (Vela et al., 2008). More particles approaching the membrane surface deposit upon the previously layer, forming a cake over the surface. This is illustrated in Figure 2-4(d). In this model, the parameter n in Equation (9) is equal to 0. In terms of the permeate flux, after linearization, the equation found in Table 2-2 can be derived. The cake layer formation model constant, K_c , incorporates the specific cake resistance term, α , as well as the filter resistance, R_0 , and the flow rate, Q_0 (Hermia, 1982). This allows the constant to be used as an indication of the degree of fouling of the membrane. From the model, an estimation for the initial permeate flux can also be determined.

The predicted permeate flux for various feed flow rates is presented in Figure 4-34. From this plot, it can be established that the constant K_c decreases with increasing feed flow rate, indicating a decrease in the degree of fouling of the membrane. This is because at higher feed flow rates, there will be an increase in the amount of solids washed away from the membrane surface, reducing the thickness of the cake layer on the membrane. This was shown to be true using the SEM images comparing trials with different feed flow rates, where the cake thickness decreased from 3.6 μm for 1.0 L/min. to 0.83 μm for 3.0 L/min.

A comparison of the measured and predicted values of the initial permeate flux using the cake layer formation model is shown in Table 4-4 for various feed flow rates. At lower feed flow rates, the model accurately predicted the initial flux, with less than 10% difference. However, at the higher feed flow rate of 3.0 L/min, the error rose to 23%. This may be because at the higher flow rate, the cake layer is washed away from the membrane surface, which is not accounted for in the model.

For increasing operating pressures, the value of K_c is shown to decrease, from 22.141s/m⁶ at 2.5 psi., to 4.0655s/m⁶ at 5.5 psi., indicating a reduction in the degree of fouling. At higher operating pressures, the cake layer may be compacted, increasing the specific cake resistance. However, it was previously shown that the filtration constant K_p , which relates to the cake resistance, decreased at higher operating pressures. This may explain the reduction in the value of K_c , since the magnitude of the cake resistance is much larger than the membrane resistance. As presented in Table 4-4, the predicted values for the initial permeate flux did not agree well with the measured values, showing deviations up to 24%.

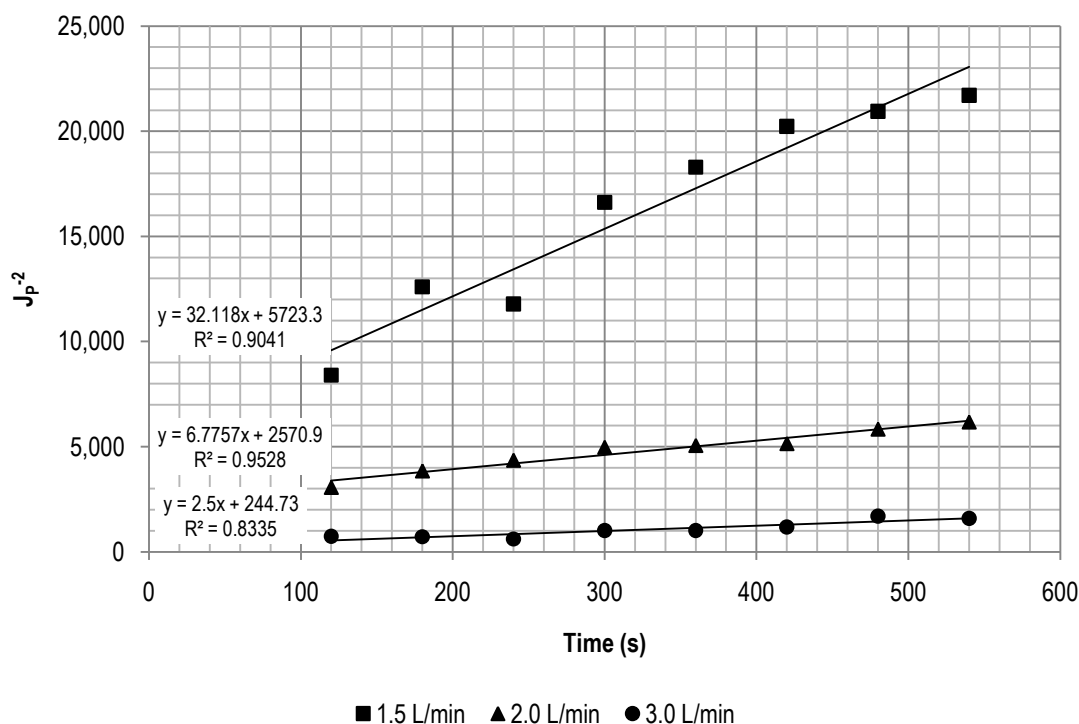


**Figure 4-34: Permeate flux predicted by the cake layer formation model for various feed flow rates
P=3.5psi., Cs=0.12%**

The constant K_c is shown to increase with increasing feed solid concentration in Figure 4-36, and can be interpreted to mean an increase in the degree of fouling of the membrane. This is expected since the thickness of the cake layer also increased as shown in Figure 4-13. The increase in thickness may be due to the larger amount of solid particles available for deposition on the membrane surface at higher feed solid concentrations. The model did not accurately predict the initial permeate flux for various feed solid concentrations, as is evident according to Table 4-4. Differences over 10% between predicted and measured values were found.

Table 4-4: Comparison between experimental initial permeate flux and the initial permeate flux obtained from the cake layer formation model

Variable	Value	K_c	J_0 (Model) (m^3/m^2s)	J_0 (Measured) (m^3/m^2s)	% Error
Flowrate (L/min) ($P=3.5$ psi, $C_s=0.12\%$)	1.5	32.118	0.013	0.014	7%
	2.0	6.7757	0.020	0.022	10%
	3.0	2.500	0.064	0.052	23%
Pressure (psi) ($Q_f=2.0$ L/min, $C_s=0.12\%$)	2.5	22.141	0.018	0.016	17%
	3.5	6.7757	0.020	0.022	10%
	4.5	4.0655	0.036	0.029	24%
Feed Solid Concentration (%) ($Q_f=2.0$ L/min, $P=3.5$ psi)	0.04	5.1645	0.068	0.043	60%
	0.12	6.7757	0.020	0.022	10%
	0.16	25.862	0.035	0.017	107%
CTAB concentration (g/L) ($Q_f=2.0$ L/min, $P=3.5$ psi, $C_s=0.12\%$ paint solids)	0.000	6.7757	0.020	0.022	10%
	0.082	4.1596	0.021	0.024	11%
	0.328	3.066	0.031	0.031	2%
	0.656	1.3366	0.036	0.040	12%

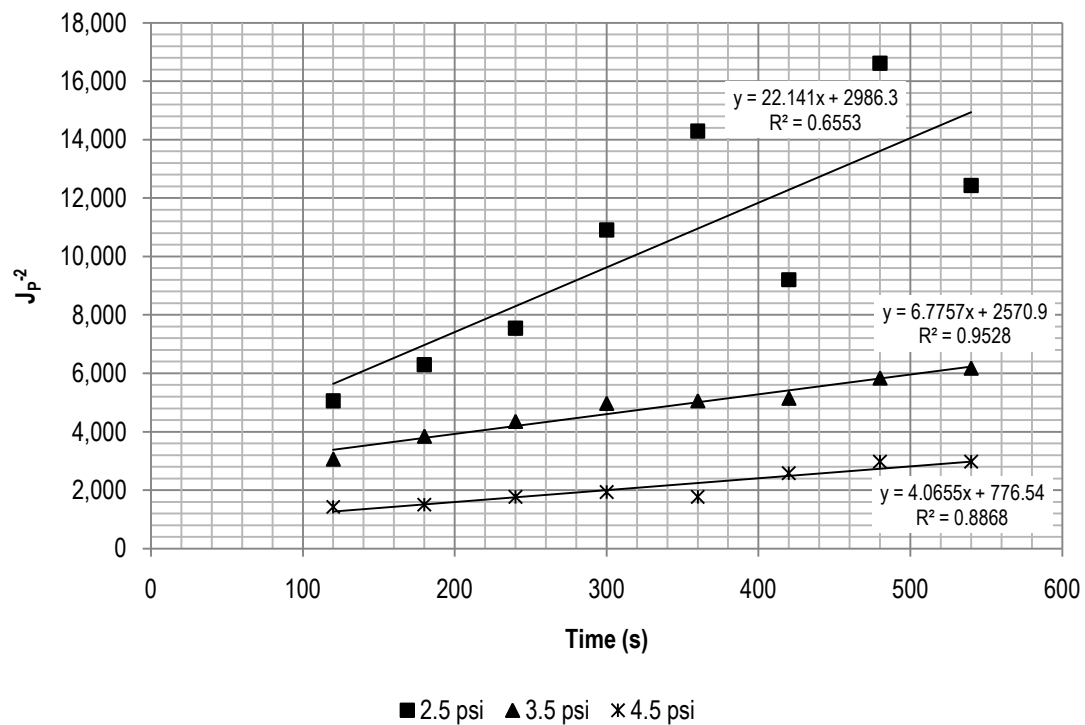


Figure 4-35: Permeate flux predicted by the cake layer formation model for various operating pressures $Q_f=2.0$ L/min, $C_s=0.12\%$

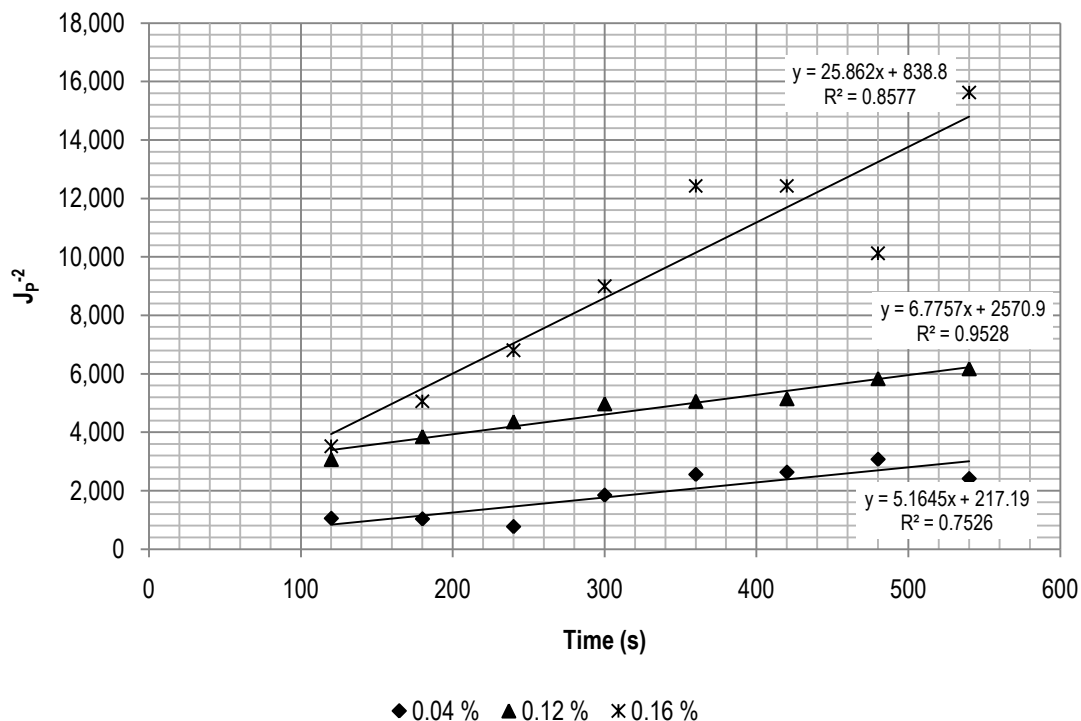


Figure 4-36: Permeate flux predicted by the cake layer formation model for various feed solid concentrations, $Q_f=2.0\text{L/min}$, $P=3.5\text{psi}$.

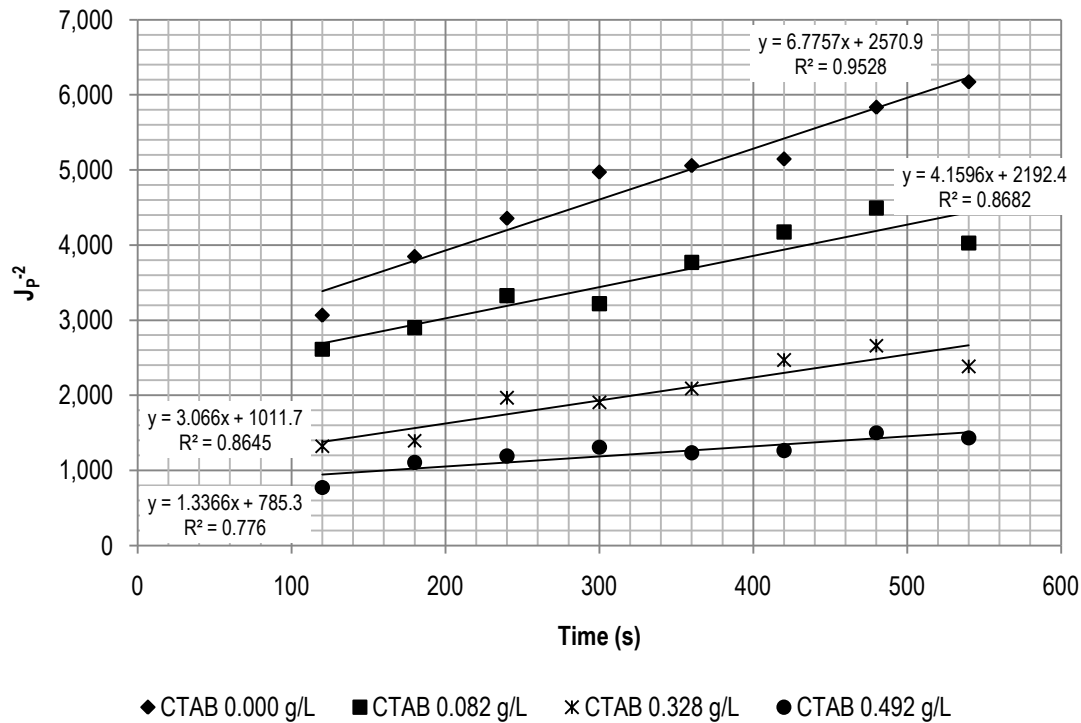


Figure 4-37: Permeate flux predicted by the cake layer formation model for various concentrations of CTAB, $P=3.5\text{ psi}$, $Q_f=2.0\text{L/min}$, $C_s=0.12\%$ paint solids

For increasing CTAB concentration, K_c generally decreases, which confirms the previous result where the increase of CTAB concentration reduces the degree of fouling of the membrane. The model also estimated the initial permeate flux well, with errors lower than 12%, as shown in Table 4-4.

4.7.5 Summary of Regression Coefficients

Shown in Table 4-5 is a summary of the measures of fit to the experimental data for Hermia's model. A number of other researchers have used this parameter to determine the most dominant mode of fouling for experimental data of various operating parameters (Sahali et al., 2010; Vela et al., 2008). The largest coefficient of determination, R^2 , between each of the models can be used as an indication of the dominant mode of fouling, which are highlighted in the table. It should be noted that all modes of fouling occurs simultaneously throughout the runs, but this method is used to determine the mode of fouling that has the greatest effect on the permeate flux.

Table 4-5: Measures of fit to the experimental data for Hermia's model

Variable	Value	R^2			
		Complete Blocking	Intermediate Blocking	Standard Blocking	Cake Layer Formation
Flowrate (L/min) (P=3.5 psi, Cs=0.12%)	1.5	0.884	0.913	0.900	0.904
	2.0	0.914	0.936	0.966	0.953
	3.0	0.834	0.840	0.849	0.834
Pressure (psi) (Q_f =2.0L/min, Cs=0.12%)	2.5	0.721	0.693	0.708	0.655
	3.5	0.914	0.936	0.966	0.953
	4.5	0.909	0.899	0.915	0.887
Feed Solid Concentration (%) (Q_f =2.0L/min, P=3.5 psi)	0.04	0.715	0.740	0.769	0.753
	0.12	0.914	0.936	0.966	0.953
	0.16	0.855	0.866	0.863	0.858
CTAB concentration (g/L) (Q_f =2.0L/min, P=3.5 psi, Cs=0.12% paint solids)	0.000	0.914	0.936	0.966	0.953
	0.082	0.878	0.874	0.876	0.868
	0.328	0.854	0.861	0.859	0.865
	0.656	0.722	0.751	0.737	0.776

At low flow rates, it was found that the intermediate blocking model best represented the experimental data. Here, the larger particles may accumulate on the membrane surface, thereby increasing the occurrence of intermediate pore blocking. However, as the feed flow rate is increased, these larger particles may be washed away from the surface, leaving the pores open for particles smaller than the pore size of the membrane to penetrate into the pores and adhere to the wall

surface, increasing the effect of standard pore blocking. This is seen, as at higher flow rates, the data is best represented by the standard blocking model.

For increasing operating pressure, the dominant mode of fouling changed from complete pore blocking to standard pore blocking. At higher pressures, particles approaching the membrane may be deformed and can be forced through the pore openings but may attach on the pore walls, increasing the occurrence of standard pore blocking.

For low feed solid concentrations, the standard blocking model showed the best agreement to the data collected. However, at the higher feed solid concentration of 0.16%, the intermediate blocking mode was dominant. This change may be due to a larger number of particles present in the feed at higher feed solid concentrations, which may result in a greater occurrence of the larger particles adhering to the pore openings before the smaller particles can penetrate through the membrane surface.

With no addition of CTAB surfactant, the dominant mode of fouling was found to be standard pore blocking. Adding CTAB to the feed resulted in complete pore blocking to be dominant, indicating that the increase in particle size of the feed due to the formation of micelles when the surfactant was added resulted in more occurrences of pore sealing due to complete pore blocking. Further increase of the CTAB concentration changed the dominant mode of fouling to be intermediate pore blocking. This may be because the greater number of micelles at CTAB higher concentrations may begin to build up on other particles already adhered on the surface of the membrane, as in the intermediate blocking model. Another increase in the CTAB concentration resulted in cake layer formation model best representing the data. This may be due to more of the micelles building up on the surface of the membrane.

4.7.6 Changing Modes of Fouling over Filtration Time

To investigate the steps involved in the membrane fouling process, as presented in Section 2.2.2, the experimental data collected for one run was evaluated at various time intervals to determine the changes in the dominant mode of fouling over filtration time. This procedure was also carried out on an experimental data set for the CTAB surfactant to investigate whether the addition of surfactant shifts the transition between the modes of fouling.

Figures 4-38 to 4-41 displays the plots for the complete blocking, intermediate blocking, standard blocking, and cake layer formation models, respectively. In Table 4-6, the coefficients of

determination for each of the models are displayed. The overall time was segregated into three main time domains. These time domains were determined through trial-and-error so that the highest regression coefficients were obtained.

For the run with no surfactant, the first time domain, from 120s to 360s, the model that best fit the data was the standard blocking model. The next time domain, from 360s to 600s, intermediate blocking was dominant. In the final time range, from 600s to 900s, the cake layer formation model showed this best fit. This was in keeping with the stages of membrane fouling, where, for the beginning of the filtration, pore blocking occurs, and cake layer formation occurs at a later stage.

When surfactant was added, the stages of membrane fouling were found to be similar. For the first time domain, from 120s to 300s, standard pore blocking was dominant. Following this was complete pore blocking between 240s and 480s. Cake layer formation was dominant from 500s to 900s.

It should be noted that the periods of time where fouling by pore blocking was dominant was longer when no surfactant was used, compared to when CTAB was added. This indicated that the micelles formed by the addition of CTAB may have been larger than the pore size of the membrane, allowing for the deposition of the micelles on the surface to form the cake layer sooner than when no surfactant was added. This is illustrated in Figure 4-42.

Table 4-6: Measures of fit to the experimental data for Hermia's models dependant on the time domain considered

Conditions	Time domain (s)	R ²			
		Complete Blocking	Intermediate Blocking	Standard Blocking	Cake Layer Formation
Q_f=2.0 L/min, P=3.5 psi., Cs=0.12% paint solids, No surfactant added	120-360	0.925	0.931	0.933	0.927
	360-600	0.902	0.905	0.904	0.902
	600-900	0.818	0.813	0.816	0.828
Q_f=2.0 L/min, P=3.5 psi., Cs=0.12% paint solids, CTAB = 0.492 g/L	120-300	0.860	0.881	0.891	0.881
	240-480	0.634	0.632	0.633	0.629
	500-900	0.880	0.889	0.885	0.896

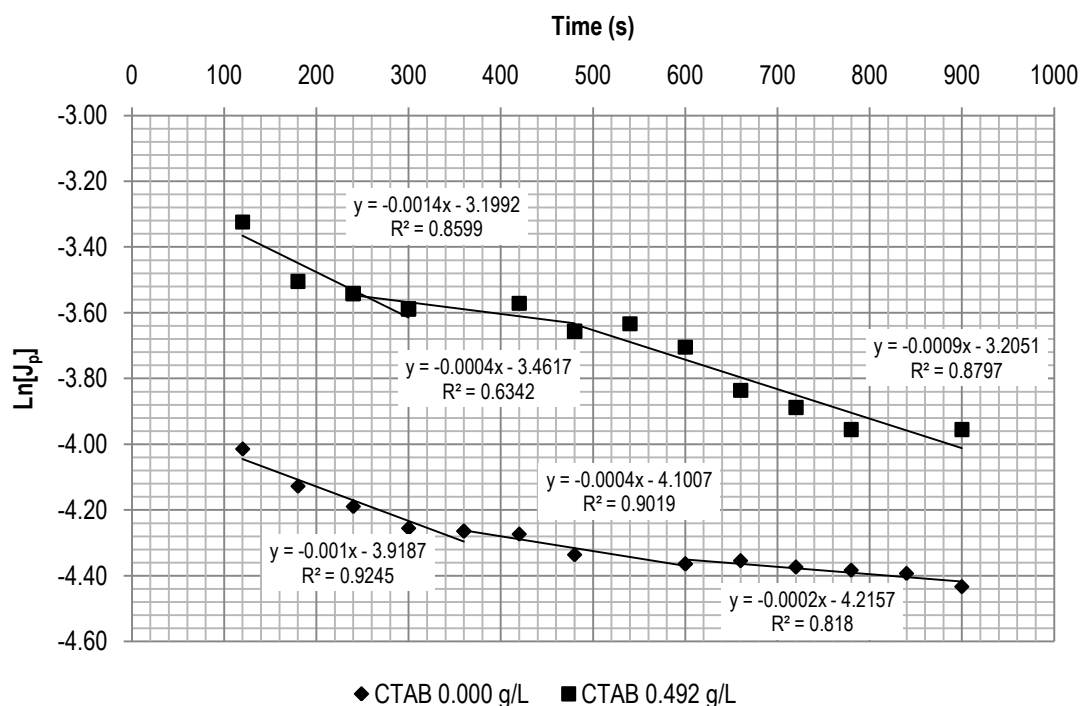


Figure 4-38: Permeate flux predicted by the complete blocking model at various time intervals over the experimental run, $Q_f=2.0\text{L/min}$, $P=3.5\text{ psi.}$, $C_s=0.12\%$

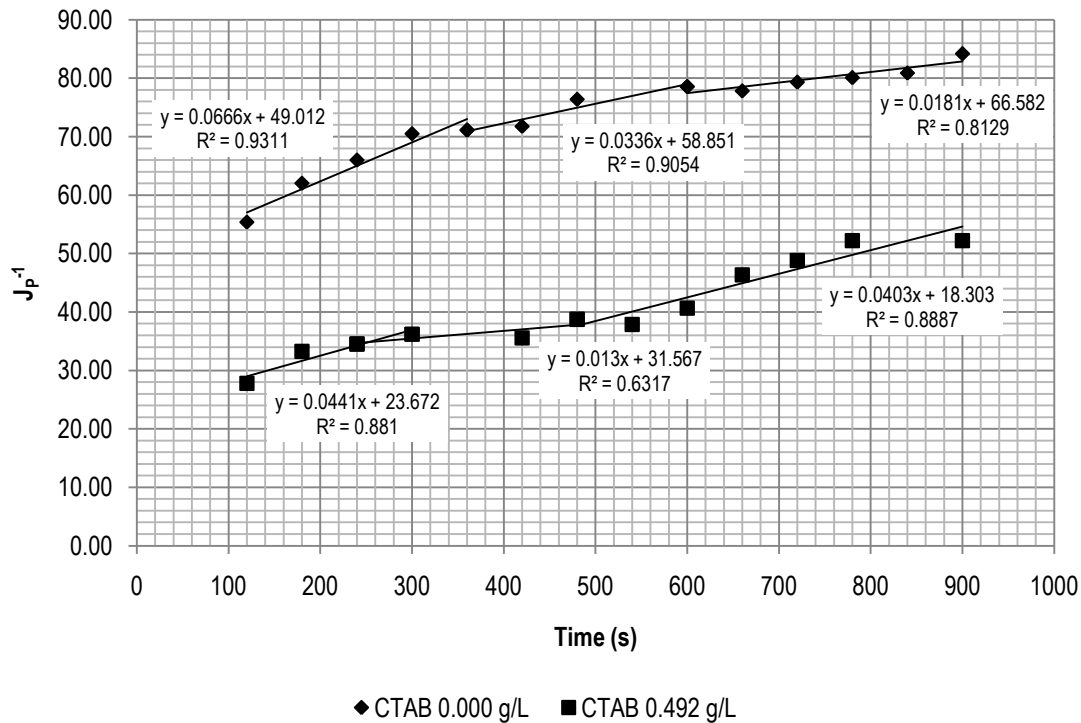


Figure 4-39: Permeate flux predicted by the intermediate blocking model at various time intervals over the experimental run, $Q_f=2.0\text{L/min}$, $P=3.5\text{ psi.}$, $C_s=0.12\%$

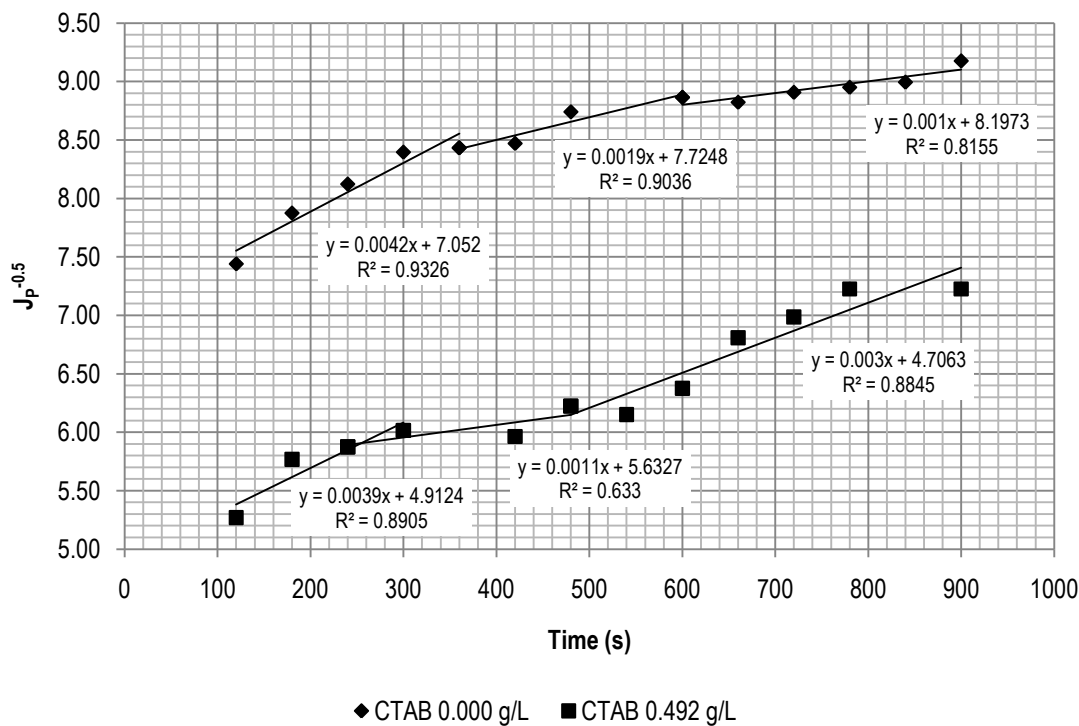


Figure 4-40: Permeate flux predicted by the standard blocking model at various time intervals over the experimental run, $Q_f=2.0\text{L/min}$, $P=3.5\text{ psi.}$, $C_s=0.12\%$

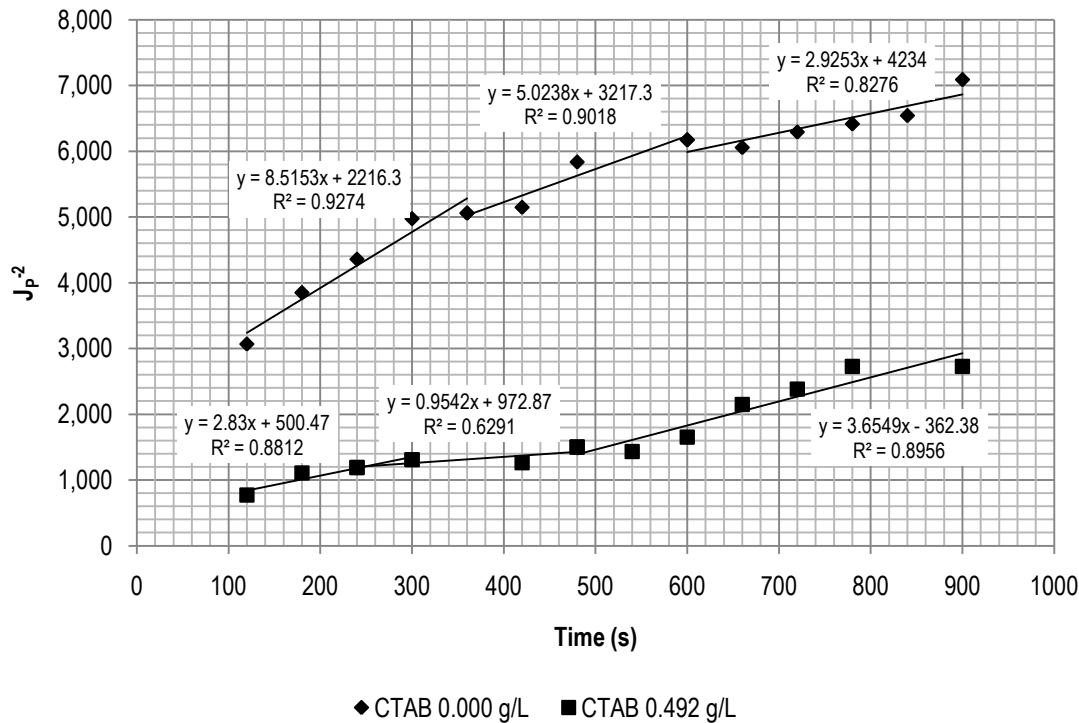


Figure 4-41: Permeate flux predicted by the cake layer formation model at various time intervals over the experimental run, $Q_f=2.0\text{L/min}$, $P=3.5\text{ psi.}$, $C_s=0.12\%$

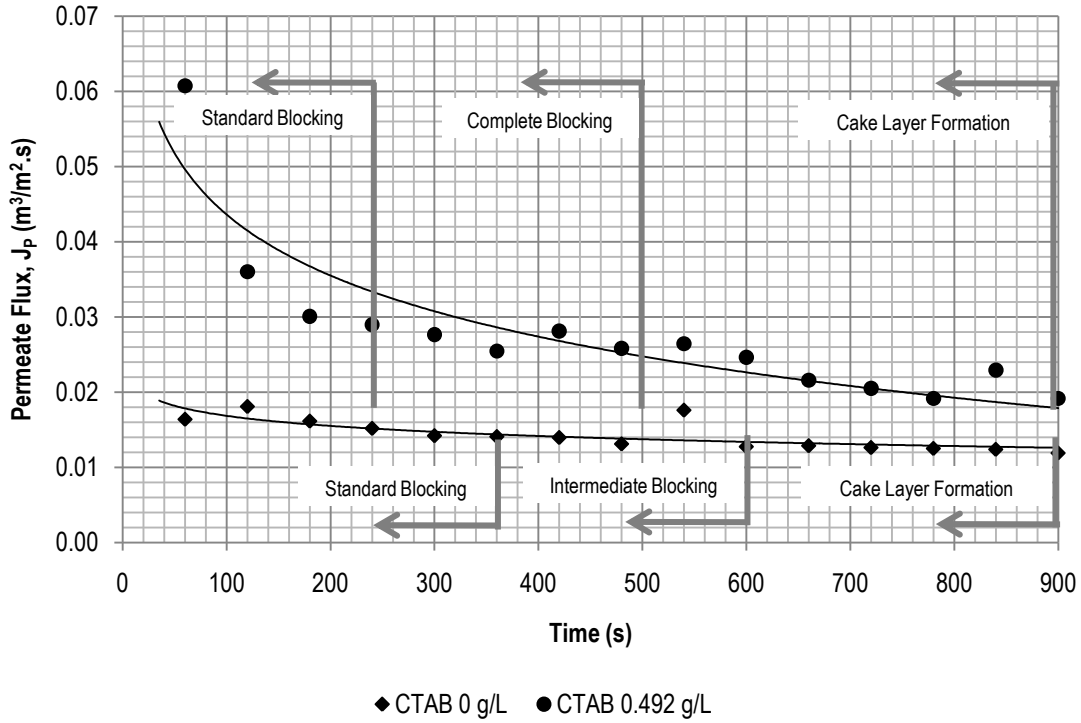


Figure 4-42: Permeate flux to demonstrate dominant mode of fouling over time, $Q_f=2.0\text{L/min}$, $P=3.5\text{ psi.}$, $C_s=0.12\%$ paint solids

4.8 Resistance-in-series Model

Applying the resistance-in-series model as shown in Equation (8) allows quantifying of the resistances to the permeate flow. It is assumed that the concentration polarization layer resistances has a limited contribution to the total resistance and is therefore ignored. In order to determine the intrinsic membrane resistance, R_M , at various operating conditions, distilled water was used as the feed solution. The steady-state permeate flux achieved for various feed flow rates and for various operating pressures are shown in Figure 4-43 (a) and (b), respectively. The cumulative mass of permeate collected as well as the permeate flux over time are included in Appendix A.

Rearranging Equation (8) yields the following expression using to determine the total membrane resistance. The resistance due to fouling was then calculated as shown in Equation (11).

$$R_{TOT} = \frac{\Delta P}{\mu J} \quad (10)$$

$$R_F = R_{TOT} - R_M \quad (11)$$

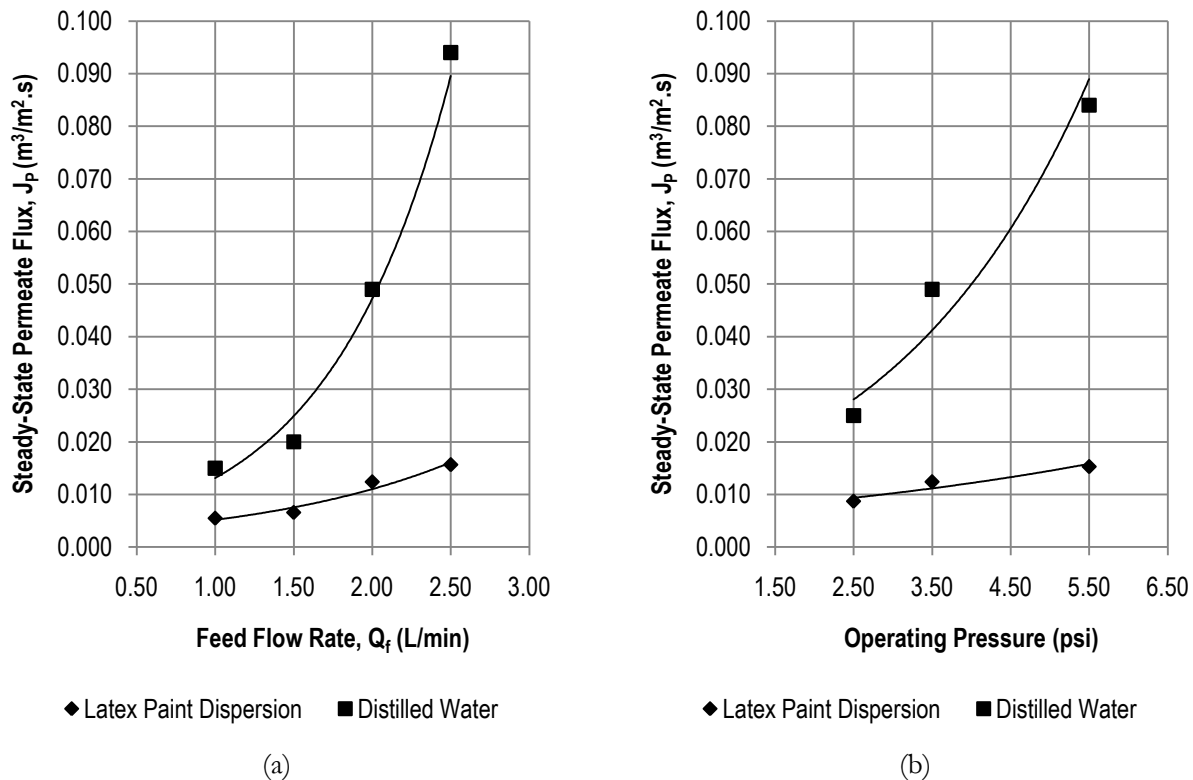


Figure 4-43: Steady-State permeate flux vs (a) Feed Flow Rate ($P=3.5\text{psi.}$, $C_s=0.12\%$ or 0% for distilled water) (b) Operating Pressure ($Q_f=2.0\text{L}/\text{min}$, $C_s=0.12\%$ or 0% for distilled water)

Figure 4-44 displays the total resistance to permeate flow for various feed flow rates. At increasing feed flow rates, this resistance is shown to decrease. This allows for the greater steady-state permeate flux levels achieved. The membrane resistance also decreases with increasing feed flow rates. This may be due to more of the particles smaller than the membrane pore size found in the feed being swept away into the retentate stream, reducing the occurrence of standard blocking as previously described. The reduction in the fouling resistance higher feed flow rates may be due to the decreased thickness of the cake layer.

The total resistance to the permeate flow is shown to generally increase with increasing operating pressure in Figure 4-45. While at 3.5 psi. and 5.5 psi. operating pressures the membrane resistance is similar with an average of $4.71 \times 10^5 \text{ m}^{-1}$, at the lower operating pressure of 2.5 psi., a slightly higher membrane resistance is found. This discrepancy may be due to residual solids remaining in the experimental apparatus when the trial using distilled water under this operating pressure was performed. Also shown in Figure 4-44, the fouling resistance increased with increasing operating pressure. This may be because at higher operating pressures, more particles are brought to the membrane surface due to the increase in the forces exerted on the particles, increasing the fouling of

the membrane and therefore the fouling resistance. The permeate flux achieved is still higher at higher operating pressure due to the proportionality of the permeate flux with the transmembrane pressure, as shown in Equation (8).

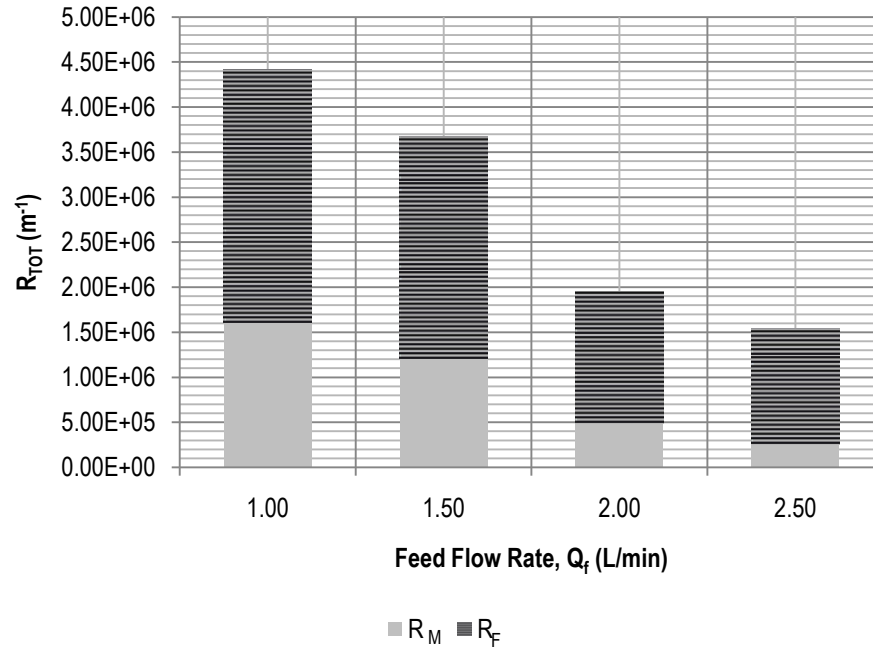


Figure 4-44: Total resistance to permeate flow, R_{TOT} vs Feed Flow Rate, Q_f

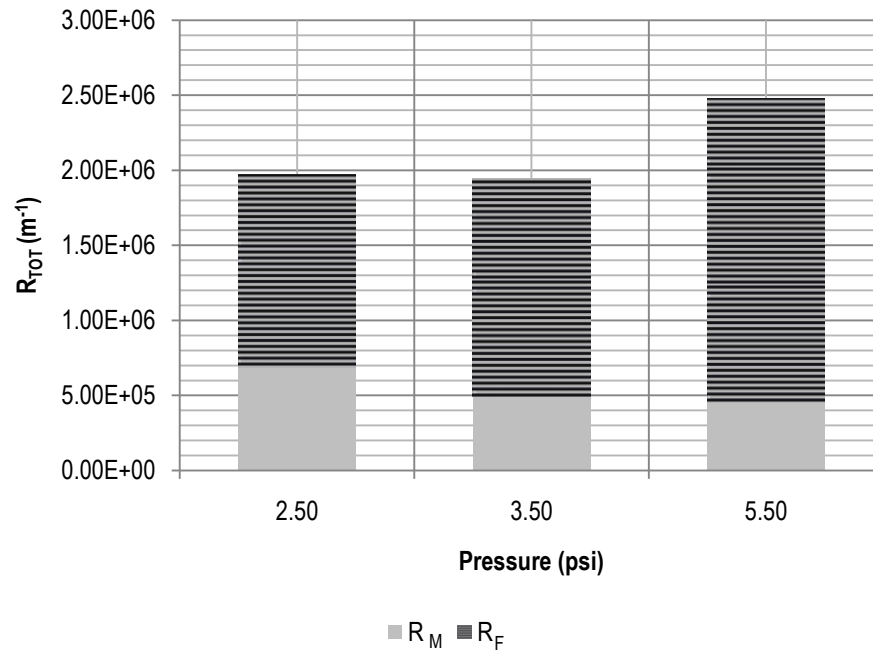


Figure 4-45: Total resistance to permeate flow, R_{TOT} vs Operating Pressure

Chapter 5

Conclusions and Recommendations

In his chapter, a summary of the conclusions obtained through this study is presented, followed by some recommendations for future work to be performed in context to the presented work.

5.1 Conclusion

From the analysis performed on the experimental results obtained, the study showed that increasing the feed flow rate increases the permeate flux achieved, from $5.43 \times 10^{-3} \text{ m}^3/\text{m}^2.\text{s}$ at 1.0 L/min to $2.15 \times 10^{-2} \text{ m}^3/\text{m}^2.\text{s}$ at 3.0 L/min, a 294% increase. Through SEM imaging, it was shown that the cake layer formed was thinner and less dense at higher feed flow rates.

A similar effect was found for increasing operating pressures. Here, changing the operating pressure from 1.5 psi. to 5.5 psi. resulted in an increase of 320% in the permeate flux achieved.

For increasing feed solid concentrations, there was an apparent reduction in the permeate flux achieved. When compared to the clean water flux of $5.50 \times 10^{-2} \text{ m}^3/\text{m}^2.\text{s}$, increasing the feed solid concentration to 0.21% resulted in a 292% reduction in the steady-state permeate flux level achieved to $4.04 \times 10^{-2} \text{ m}^3/\text{m}^2.\text{s}$. The cake thickness was shown to increase with increasing feed solid concentrations through SEM images of the cross-sections of the used membranes.

Another major effect investigated was the addition of surfactants to the feed in order to positively affect the permeate flux. It was found that the addition of anionic surfactant, SDS, actually reduced the effectiveness of the separation process. When added at twice the SDS critical micelle

concentration (CMC), a reduction of 58% of the permeate flux was found. In contrast, using the cationic surfactant CTAB greatly increased the permeate flux, up to 134% higher when twice its CMC was used. The cake layer formed when cationic surfactant was used was thicker and less dense than without surfactant.

Using the gel layer model for concentration polarization, the mass transfer coefficient of the solute was found to be $7.99 \times 10^{-7} \text{ m}^3/\text{m}^2\cdot\text{s}$. The gel layer concentration was also determined to be 0.42%.

Hermia's models were used to describe the degree of fouling of the membranes for each variable considered. It was found that the majority of the experimental data agreed well with the model fits, and the trends discussed were generally confirmed. The coefficient of determination, R^2 , was used to identify the dominant mode of fouling. When considering the change of the dominant mode of fouling over time for latex paint wastewater, it was found that initially, there was a period where standard blocking was dominant, followed by a period of intermediate blocking, and finally, cake layer formation was dominant. Similarly, the CTAB treated feed showed that standard blocking was dominant at the beginning of the filtration. However, this time period was shorter, from 120-300s compared to 120-360s when the untreated feed was used. Complete blocking then followed this time period for the CTAB treated feed, before cake layer formation was dominant. The occurrence of complete blocking in the CTAB treated feed may be an indication that the particle size of the constituents of the feed was increased to be larger than the pore size of the membrane.

Using the resistance-in-series model, the membrane and fouling resistances were determined. At 3.5 psi. and 2.0 L/min, these were found to be $4.91 \times 10^5 \text{ m}^{-1}$ and $1.45 \times 10^6 \text{ m}^{-1}$, respectively. The total resistance to permeate flow decreased with increasing feed flow rate, but showed an increase with increasing operating pressure.

5.2 Recommendations

From this study, a few areas that may require further investigation are identified as follows:

- Investigate pressure on the permeate flux decline for CTAB treated latex paint dispersions. Since the micelles formed were expected to be larger than the particles found originally in the dispersion, there may be some deformation of these micelles at larger operating pressures. An increased effect of fouling at higher operating pressures is expected.

- Determine the effect of non-ionic and zwitterionic surfactants on the permeate flux decline. Because this study compared only anionic and cationic surfactants, no conclusions can be extrapolated to include the effect of non-ionic and zwitterionic surfactants.
- Combining various ratios of different types of surfactants is another area that can be studied. This has been done for a number of different feed solutions but not on latex paint dispersions.

References

- Ahmad, A., Chong, M., & Bhatia, S. (2006). Ultrafiltration modeling of multiple solutes system for continuous cross-flow process. *Chemical Engineering Science* , 61 (15), 5057-5069.
- Anderson, J., Springer, W., & Strosberg, G. (1981). Application of reverse osmosis to automotive electrocoat paint wastewater recycling. *Desalination* , 36 (2), 179-188.
- Apel, P. (2001). Track etching technique in membrane technology. *Radiation Measurements* , 34 (1-6), 559-566.
- Armengol, J., Calbo, J., Pujol, T., & Roura, P. (2008). Bernoulli correction to viscous losses: Radial flow between two parallel discs. *American Journal of Physics* , 76 (8), 730-737.
- Beca, J. (2007). Pharmaceutical discharge: Zero discharge for pharma plant. *Filtration & Separation* , 44 (6), 40-41.
- Benitez, F., Acero, J., Leal, A., & Gonzalez, M. (2009). The use of ultrafiltration and nanofiltration membranes for the purification of cork processing wastewater. *Journal of Hazardous Materials* , 162, 1438-1445.
- Berg, P., Hagmeyer, G., & Gimbel, R. (1997). Removal of pesticides and other micropollutants by nanofiltration. *Desalination* , 113 (2-3), 205-208.
- Bhattacharjee, C., & Datta, S. (2003). Analysis of polarized layer resistance during ultrafiltration of PEG-6000: an approach based on filtration theory. *Separation and Purification Technology* , 33 (2), 115-126.
- Bowen, W., Calvo, J., & Hernández, A. (1995). Steps of membrane blocking in flux decline during protein microfiltration. *Journal of Membrane Science* , 101 (1-2), 153-165.
- Burba, P., Geltenpoth, H., & Nolte, J. (2005). Ultrafiltration behavior of selected pharmaceuticals on natural and synthetic membranes in the presence of humic-rich hydrocolloids. *Analytical and Bioanalytical Chemistry* , 382 (8), 1934-1941.

- Csefalvay, E., Imre, P., & Mizsey, P. (2008). Applicability of nanofiltration and reverse osmosis for the treatment of wastewater of different origin. *Central European Journal of Chemistry* , 6 (2), 277-283.
- Dey, B. K., Hashim, M. A., Hasan, S., & Gupta, B. (2004). Microfiltration of water-based paint effluents. *Advances in Environmental Research* , 8 (3-4), 455-466.
- Doering, C., & Constantin, P. (1994). Variational bounds on energy dissipation in incompressible flows: Shear flow. *Physical Review E* , 49 (5), 4087-4099.
- Ferella, F., Prisciandaro, M., De Michelis, I., & Veglio, F. (2007). Removal of heavy metals by surfactant-enhanced ultrafiltration from wastewaters. *Desalination* , 207, 125-133.
- Foley, G. (1994). Membrane fouling in crossflow filtration: implications for measurement of the steady state specific cake resistance. *Biotechnology Technique* , 8 (10), 743-746.
- Ganguly, S., & Bhattacharya, P. (1994). Development of concentration profile and prediction of flux for ultrafiltration in a radial cross-flow cell. *Journal of Membrane Science* , 97, 185-198.
- Geankopolis, C. (1993). *Transport Processes and Unit Operations* (3rd Edition ed.). NJ: Prentice-Hall Inc.
- Gelinas, S. (1995). *Micellar-enhanced ultrafiltration using a twin-bead cationic surfactant*. McGill University, Department of Chemical Engineering, Montreal, QC.
- General Electric Company. (2009). *GE PCTE (Polycarbonate) Membrane Filters*. Retrieved October 21, 2009, from GE Osmonics Labstore: <http://www.osmolabstore.com/OsmoLabPage.dll?BuildPage&1&1&323>
- Ghose, S., Bhattacharjee, C., & Datta, S. (2000). Simulation of unstirred batch ultrafiltration process based on a reversible pore-plugging model. *Journal of Membrane Science* , 169 (1), 29-38.
- Goosena, M., Sablania, S., Al-Maskaria, S., Al-Belushia, S., & Wilfb, M. (2002). Effect of feed temperature on permeate flux and mass transfer coefficient in spiral-wound reverse osmosis systems. *Desalination* , 144 (1-3), 367-372.
- Hermia, J. (1982). Constant pressure blocking filtration laws - application to power-law non-newtonian fluids. *Chemical Engineering Research and Design* , 60a, 183-187.
- Hwang, K., & Lin, T. (2002). Effect of morphology of polymeric membrane on the performance of cross-flow microfiltration. *Journal of Membrane Science* , 199 (1-2), 41-52.

- Hwang, K., Liao, C., & Tung, K. (2007). Analysis of particle fouling during microfiltration by use of blocking models. *Journal of Membrane Science* , 287, 287-293.
- Kennedy, M., Kamanyi, J., Rodriguez, S., Lee, N., Schippers, J., & Amy, G. (2008). Water Treatment by Microfiltration and Ultrafiltration. In N. Li, A. Fane, W. Ho, & T. Matsuura (Eds.), *Advanced Membrane Technology and Applications* (pp. 131-170). John Wiley & Sons Inc. .
- Kohuniewicz, A. (1992). Predicting permeate flux in ultrafiltration on the basis of surface renewal concept. *Journal of Membrane Science* , 107-118.
- Konieczny, K., Rajca, M., Bodzek, M., & Kwiecinska, A. (2009). Water treatment using hybrid method of coagulation and low-pressure membrane filtration. *Environment Protection Engineering* , 35 (1), 5-22.
- Körbahti, B., Aktaş, N., & Tanyolaç, A. (2007). Optimization of electrochemical treatment of industrial paint wastewater with response surface methodology. *Journal of Hazardous Materials* , 148 (1-2), 83-90.
- Kurt, U., Avsar, Y., & Talha Gonullu, M. (2006). Treatability of water-based paint wastewater with Fenton process in different reactor types. *Chemosphere* , 64 (9), 1536-1540.
- Microtrac. (2008). *Microtrac Laser Diffraction Particle Size Analyzer for Sizing Distributions of Submicron Micron Millimeter Particulates*. Retrieved January 26, 2010, from Microtrac: <http://www.microtrac.com/ProductsTechnology/MicrotracS3500ParticleSizeAnalyzer.aspx>
- Mikulasek, P., & Cakl, J. (1994). Removal of industrial latex dispersions from waste waters using microporous alumina membranes. *Desalination* , 95, 211-220.
- Mohammadi, T., Kazemimoghadam, M., & Saadabadi, M. (2003). Modeling of membrane fouling and flux decline in reverse osmosis during separation of oil in water emulsions. *Desalination* , 157, 369-375.
- Montgomery, D., & Runger, G. (2003). *Applied Statistics and Probability for Engineers* (3rd Edition ed.). New York, NY: John Wiley & Sons.
- Mukerjee, P., & Mysels, K. (1971). *Critical Micelle Concentration of Aqueous Surfactant Systems*. Washington, D.C.: US. Government Printing Office.

- Nakao, S. (1994). Determination of pore size and pore size distribution 3. Filtration membranes. *Journal of Membrane Science* , 96, 131-165.
- Noble, J. (2006). GE ZeeWeed technology for pharmaceutical wastewater treatment. *Membrane Technology* , 9, 7-9.
- Oatley, D., Cassey, B., Jones, P., & Bowen, W. (2005). Modelling the performance of membrane nanofiltration – recovery of a high-value product from a process waste stream. *Chemical Engineering Science* , 60, 1953-1964.
- Riesmeier, B., Kroner, K., & Kula, M.-R. (1989). Tangential filtration of microbial suspensions: filtration resistances and model development. *Journal of Biotechnology* , 12, 153-172.
- Russell, D. (2006). *Practical Wastewater Treatment*. John Wiley & Sons Inc.
- Salahi, A., Abbasi, M., & Mohammadi, T. (2010). Permeate flux decline during UF of oily wastewater: Experimental and modeling. *Desalination* , 251, 153-160.
- Salahi, A., Mohammadi, T., Pour, A., & Rekabdar, F. (2009). Oily wastewater treatment using ultrafiltration. *Desalination and Water Treatment* , 6 (1-3), 289-298.
- Shirazi, S., Len, C., & Chen, D. (2010). Inorganic fouling of pressure-driven membrane processes — A critical review. *Desalination* , 250 (1), 236-248.
- Song, L., & Elimelech, M. (1995). Theory of Concentration Polarization in Crossflow Filtration. *Journal of the Chemical Society, Faraday Transactions* , 91 (19), 3389-3398.
- Tchobanoglous, G., Burton, F., & Stensel, H. (2003). *Wastewater engineering: treatment and reuse*. McGraw-Hill.
- Um, M., Yoon, S., Lee, C., Chung, K., & Kim, J. (2001). Flux enhancement with gas injection in crossflow ultrafiltration of oily wastewater. *Water Research* , 35 (17), 4095-4101.
- Vela, M., Blanco, S., Garcia, J., & Rodríguez, E. (2008). Analysis of membrane pore blocking models applied to the ultrafiltration of PEG. *Separation and Purification Technology* , 62 (3), 489-498.
- Viadero, R., Vaughan, R., & Reed, B. (1999). Study of series resistances in high-shear rotary ultrafiltration. *Journal of Membrane Science* , 162, 199-211.
- Wijmans, J., Nakao, S., & Smolders, C. (1984). Flux limitation in ultrafiltration: osmotic pressure model and gel layer model. *Journal of Membrane Science* , 20 (2), 115-124.

- Yoon, Y., Westerhoff, P., Yoon, J., & Snyder, S. (2004). Removal of 17 β -Estradiol and Fluoranthene by nanofiltration and ultrafiltration. *Journal of Environmental Engineering* , 130 (12), 1460-1467.
- Yu, C., Wu, C., Lin, C., Hsiao, C., & Lin, C. (2008). Hydrophobicity and molecular weight of humic substances on ultrafiltration fouling and resistance. *Separation and Purification Technology* , 64, 206-212.

Appendix A

Experimental Data Collected

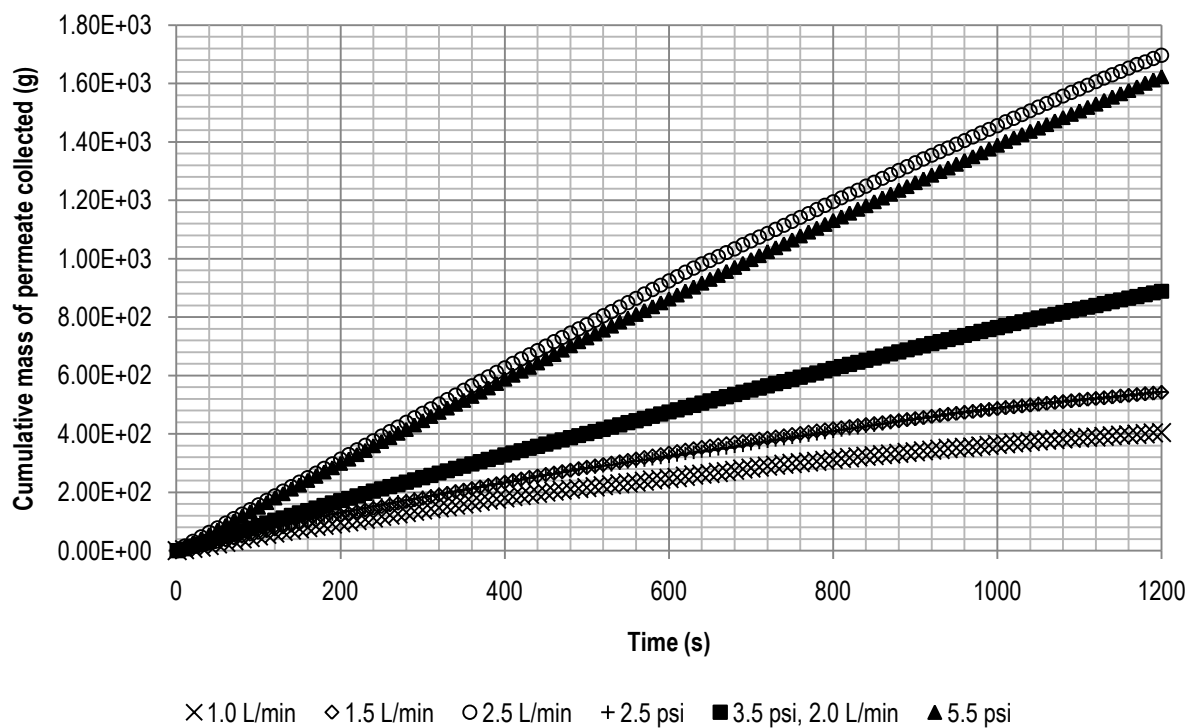


Figure A-1: Cumulative mass of permeate collected vs time for various operating conditions using Distilled Water

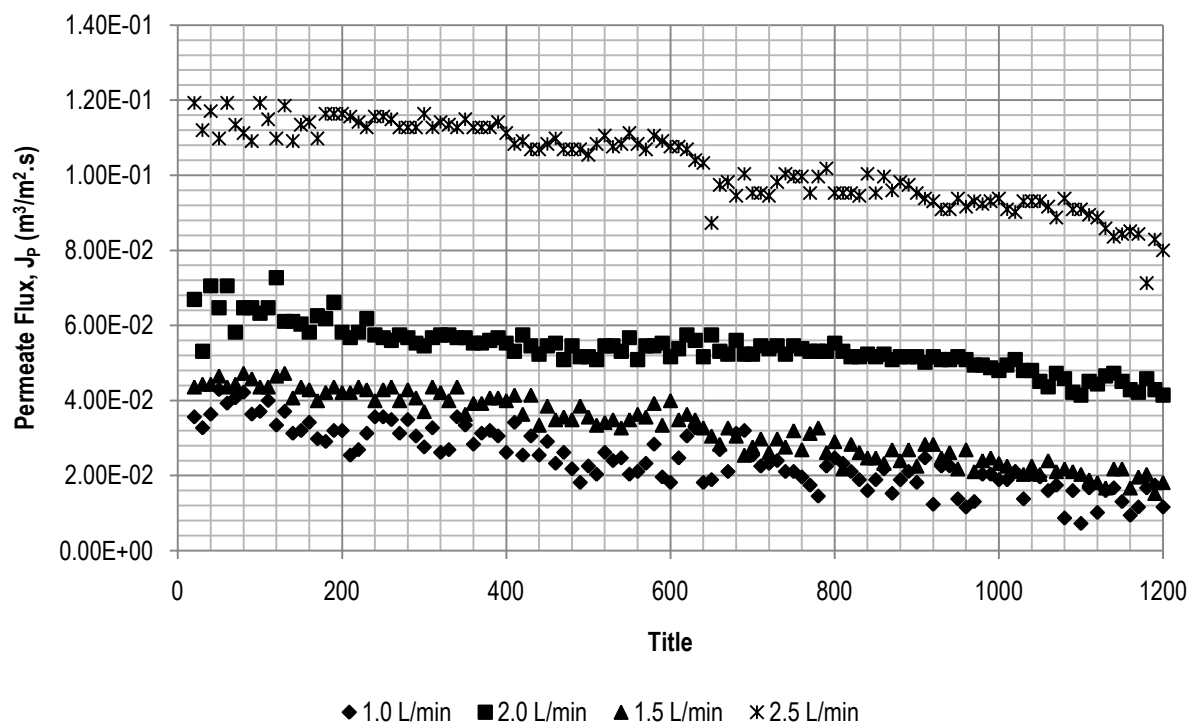


Figure A-2: Permeate Flux vs time for various feed flow rates using Distilled Water

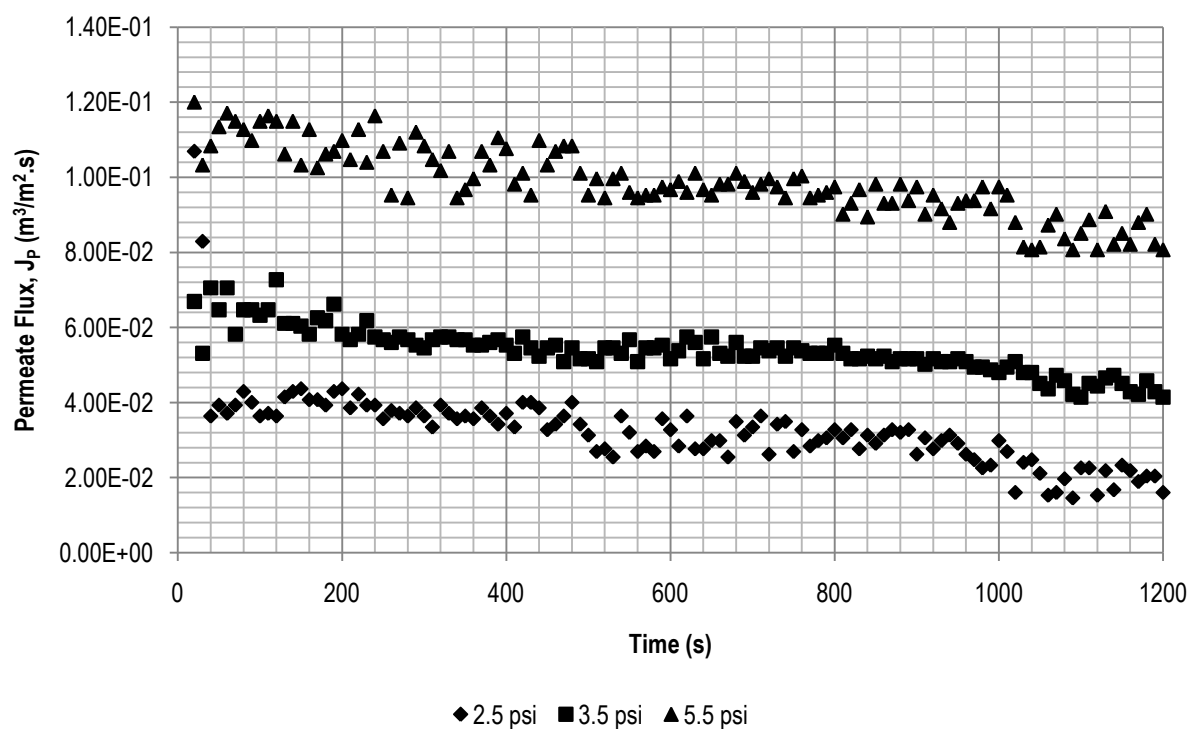


Figure A-3: Permeate flux vs time for various operating pressures using Distilled Water

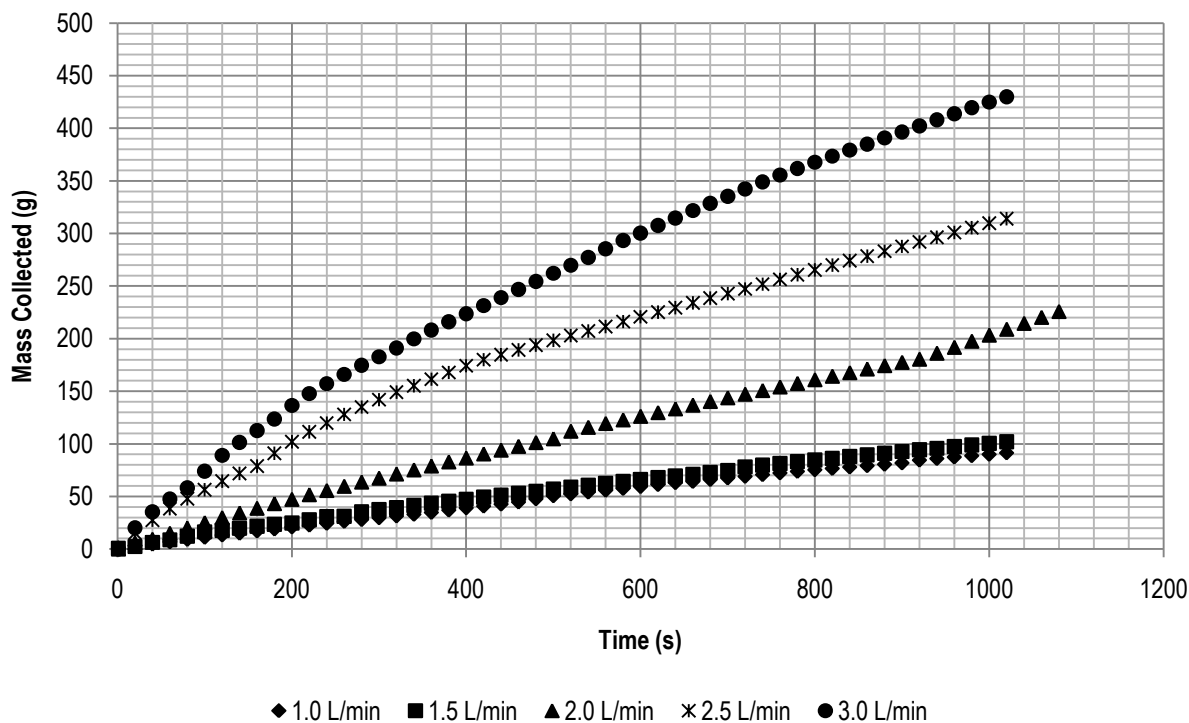


Figure A-4: Cumulative mass of permeate collected vs time for various feed flow rates, $P=3.5\text{psi}$, $C_s=0.12\%$

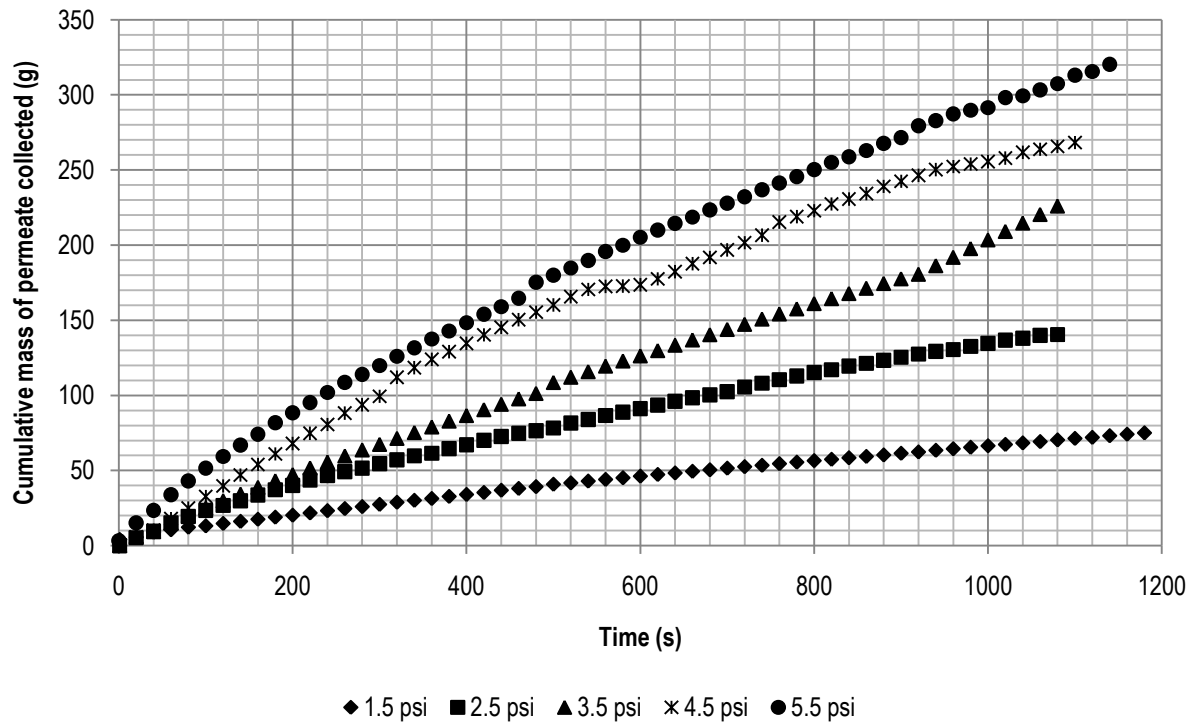


Figure A-5: Cumulative mass of permeate collected vs time for various operating pressures, $Q_f=2.0\text{L/min}$, $C_s=0.12\%$

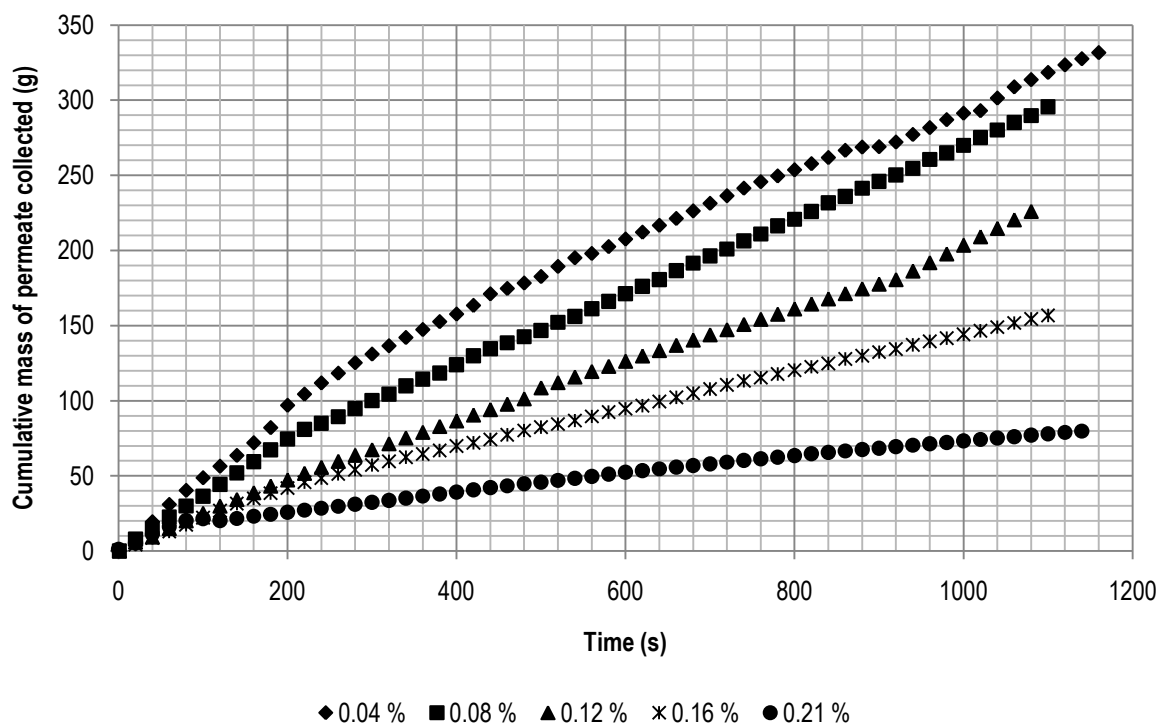


Figure A-6: Cumulative mass of permeate collected vs time for various feed solid concentrations
 $Q_f=2.0\text{L/min}$, $P=3.5\text{ psi}$.

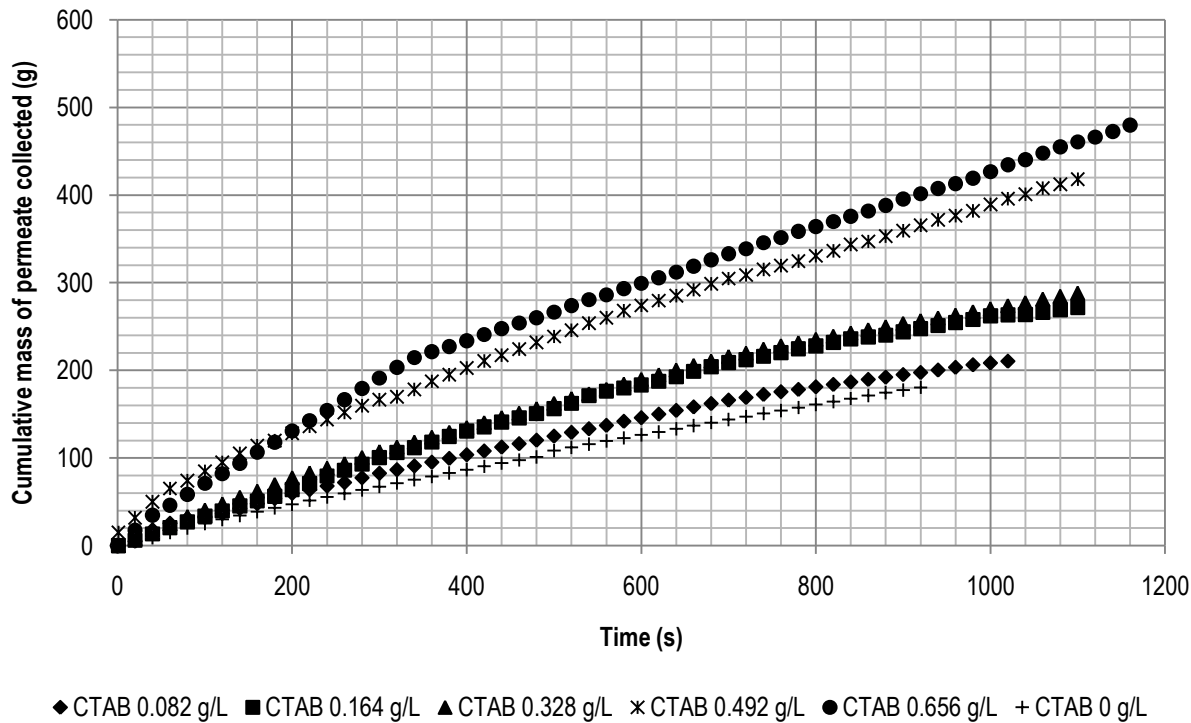


Figure A-7: Cumulative mass of permeate collected vs time for various CTAB surfactant concentrations, $Q_f=2.0\text{L/min}$, $P=3.5\text{ psi}$, $C_s=0.12\%$

Appendix B

t/v Data Graphs

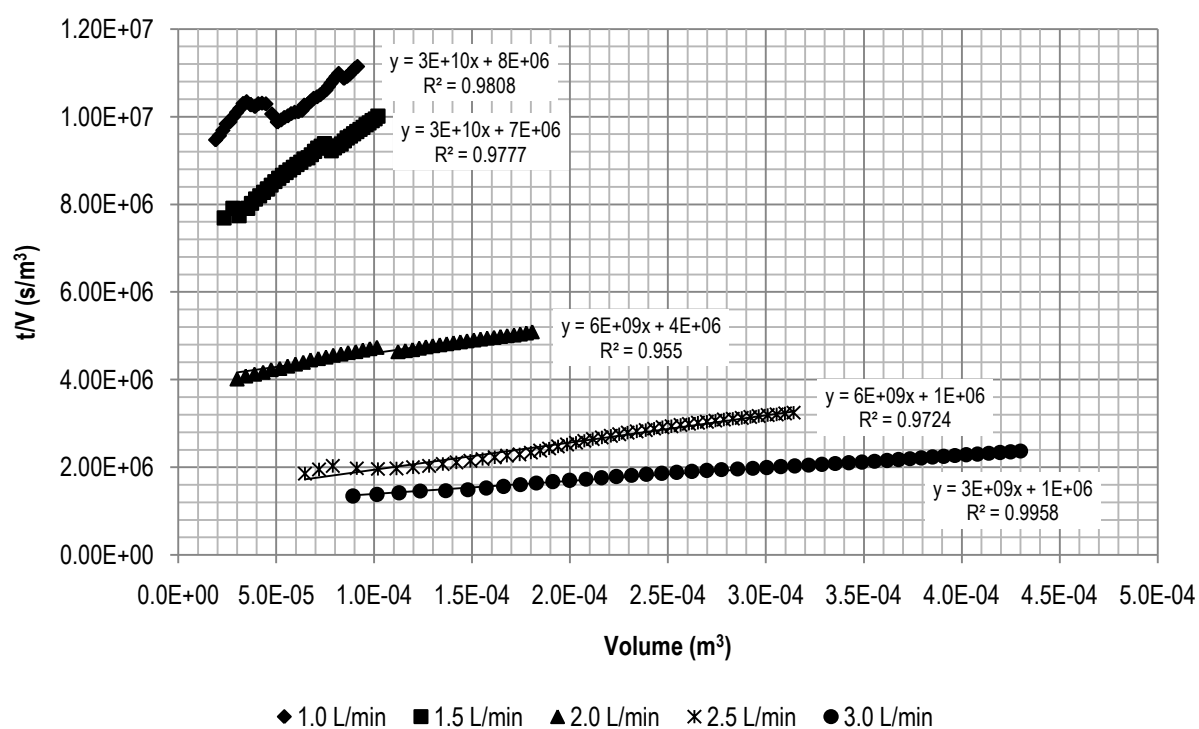


Figure B-1: t/V vs V plots for various feed flow rates, $P=3.5\text{psi}$, $C_s=0.12\%$

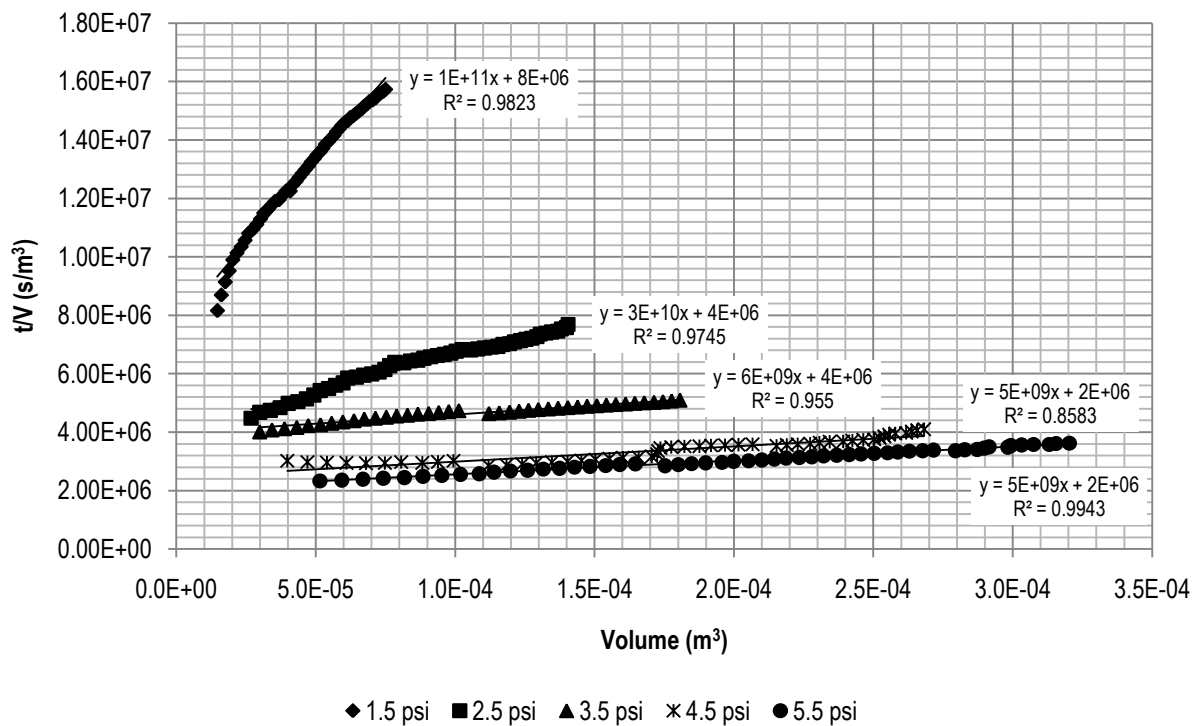


Figure B-2: t/V plots for various operating pressures, $Q_f=2.0\text{L/min}$, $C_s=0.12\%$

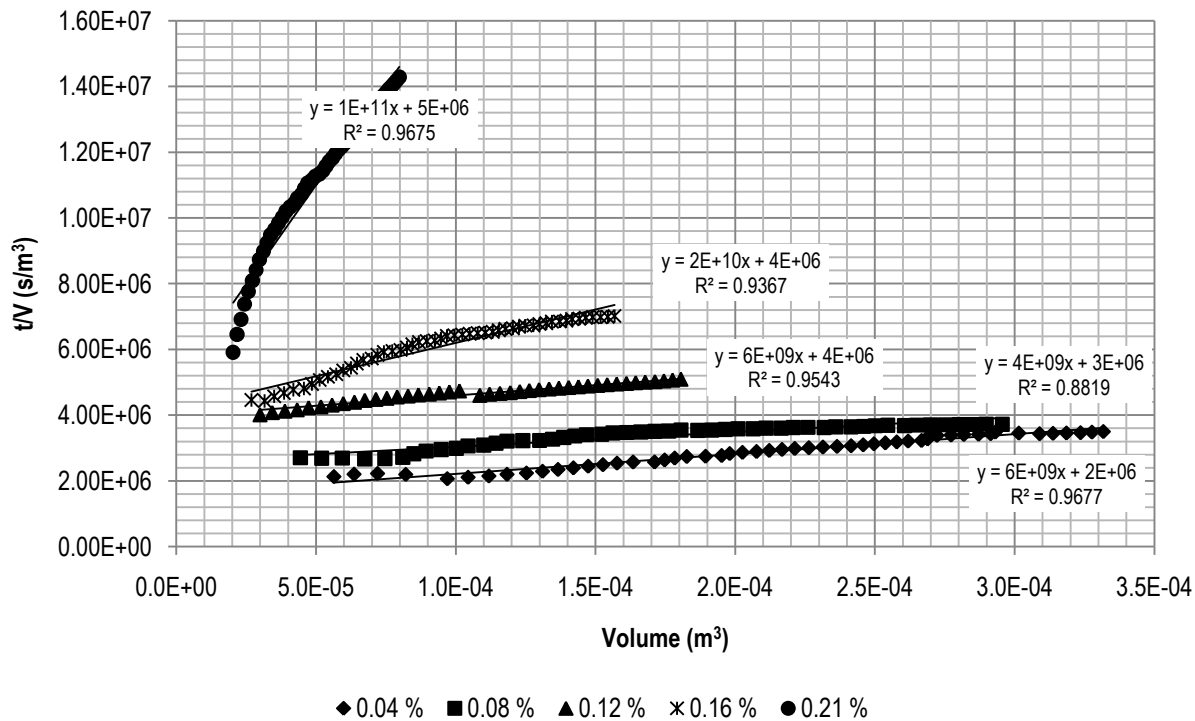
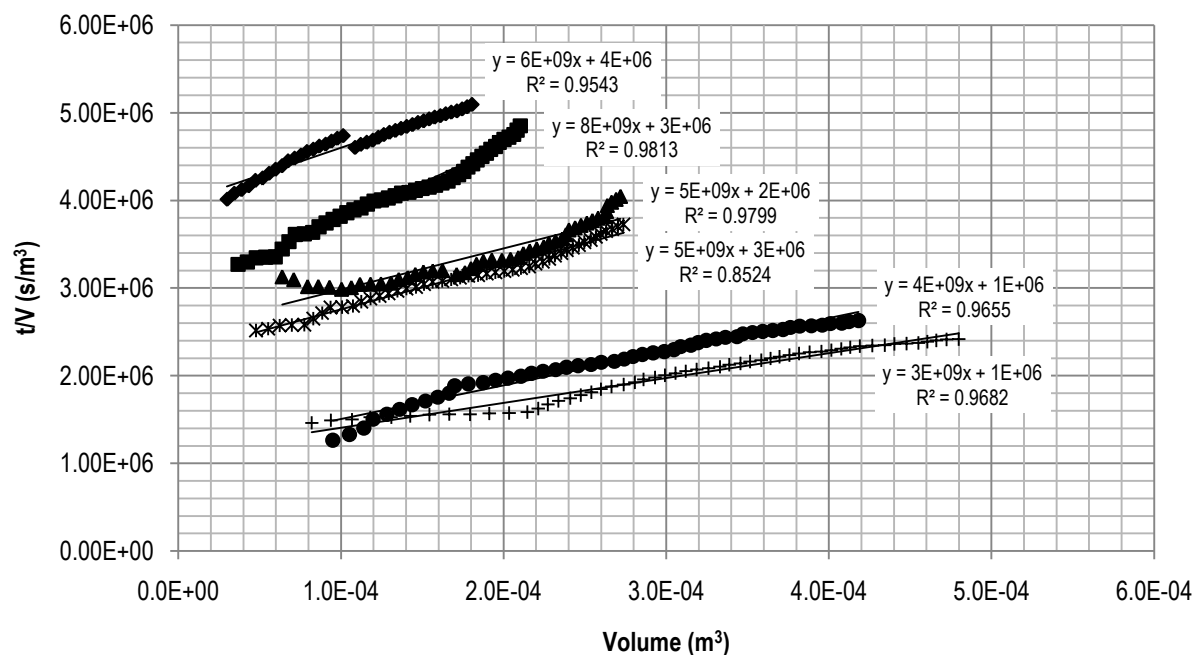


Figure B-3: t/V vs V plots for various feed concentrations, $Q_f=2.0\text{L/min}$, $P=3.5$ psi.



◆ CTAB 0 g/L ■ CTAB 0.082 g/L ▲ CTAB 0.164 g/L × CTAB 0.328 g/L ● CTAB 0.492 g/L + CTAB 0.656 g/L

Figure B-4: t/V vs V plots for various CTAB surfactant concentrations,
 $Q_f=2.0\text{L/min}$, $P=3.5\text{psi}$, $C_s=0.12\%$

Appendix C

Ultrafiltration Cell

The ultrafiltration cell used for these experiments was constructed of two acrylic parts. The base part of the cell had the opening at its centre for the feed flow stream. When sealed together using four sets of stainless steel nuts and bolts, a narrow cavity existed between these two pieces. It is within this cavity that the feed stream travelled. The upper part of the cell was recessed to allow the positioning of the membrane sheet as well as a stainless steel support, above which another cavity was located, used to collect the permeate stream. A small circular, PVC block measuring 49 mm in diameter was used at the centre of the unit to provide additional support to the upper cavity. A diagram illustrating the geometry and dimensions of this cell can be found in Figure C-1.

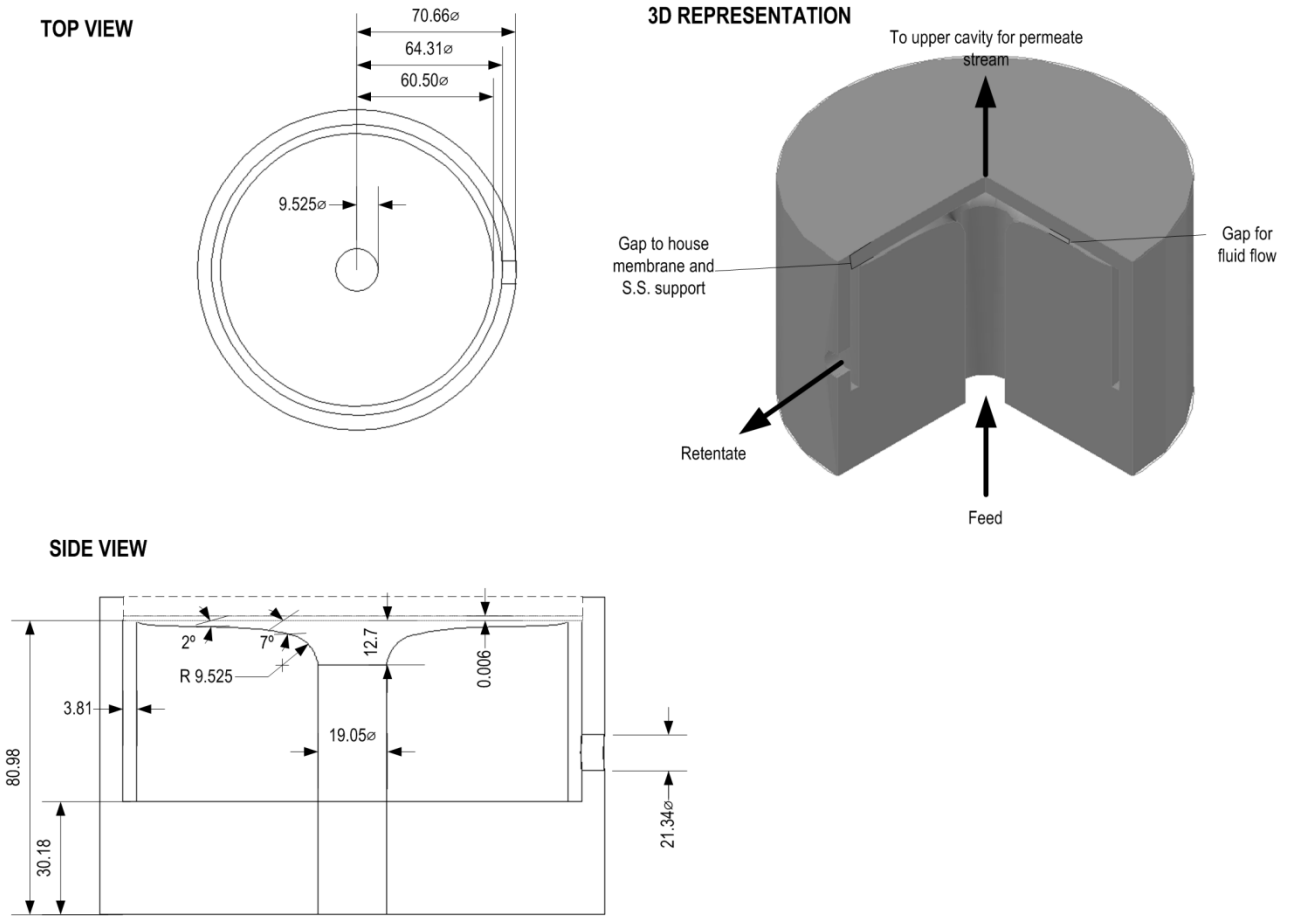


Figure C-1: Ultrafiltration cell with dimensions (all sizes in mm)

Due to the geometry of the ultrafiltration cell, for the purpose of determining the type of flow through the unit, it can most easily be described as flow between two plane-parallel discs. Here, the characteristic linear dimension is defined as the distance between the two plates, H (Doering & Constantin, 1994); in this case, this is the distance between the surface of the lower acrylic part and the surface of the membrane.

The average velocity in this geometry is as follows:

$$\bar{v} = \frac{Q}{2\pi r H} \quad (\text{C-1})$$

The following expression shows the equation for the Reynolds number, Re , of the flow on the feed side of the ultrafiltration cell (Armengol et al., 2008).

$$Re = \frac{\rho D \bar{v}}{\eta} = \frac{\rho H}{\eta} * \frac{Q}{2\pi r H} = \frac{\rho Q}{2\pi r \eta} \quad (C-2)$$

It is assumed that the critical Reynolds number, Re_c , is similar to that of the flow through circular pipes, i.e. $Re_c=2000$. Properties of the fluid were assumed to be similar to water at 20°C (Armengol et al., 2008), density, $\rho=1000 \text{ kg/m}^3$ and viscosity, $\eta = 1.024 \times 10^{-3} \text{ Pa.s}$.

From this, it was determined that the flow at the centre point of cell for each of the experimental trials were all well below the critical Reynolds number, indicating laminar flow, as shown in Table C-1.

Table C-1: Maximum Reynolds number of flow on the feed side of the ultrafiltration cell for various feed flow rates

Feed Flow Rate, Q_f (L/min)	Re
1.0	271
1.5	407
2.0	543
2.5	679
3.0	814

Appendix D

Reproducibility

In order to verify the reproducibility of the data collected, multiple runs were conducted at identical operating conditions. These were $Q_f = 2.0$ L/min, $P = 3.5$ psi., and $C_s = 0.12\%$. Plots of t/V vs. V for these repeated trials are shown in Figure D-1.

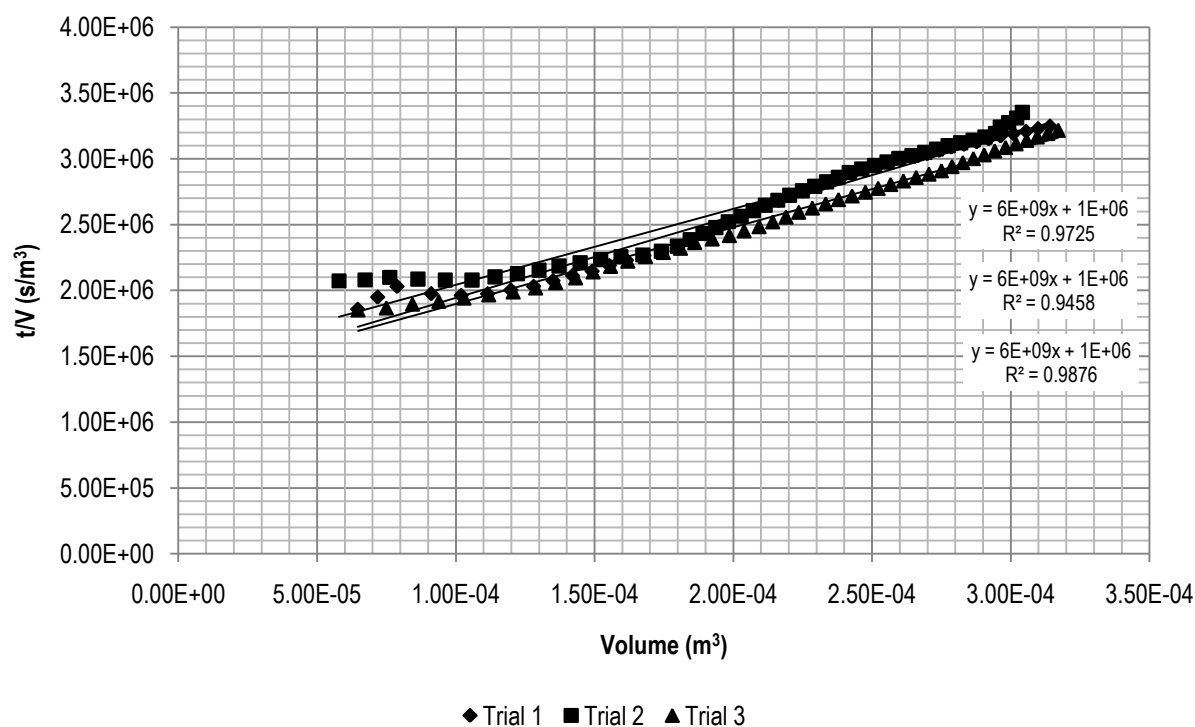


Figure D-1: t/V vs V plots for various CTAB surfactant concentrations,
 $Q_f=2.0$ L/min, $P=3.5$ psi, $C_s=0.12\%$

From this plot, values of the constants K_p and F_M were extracted, and the standard deviation was calculated (Montgomery and Runger, 2003), as shown in Table D-1.

Table D-1: Filtration constants for repeated trials at $Q_f=2.0\text{L}/\text{min}$, $P=3.5\text{ psi.}$, and $C_s=0.12\%$

	K_p	F_M
Trial 1	1.24×10^{10}	1.32×10^6
Trial 2	1.15×10^{10}	1.47×10^6
Trial 3	1.16×10^{10}	1.32×10^6
Average	1.19×10^{10}	1.37×10^{10}
Standard Deviation	4.98×10^8	8.51×10^4